UNIVERSITY OF SOUTHAMPTON
FACULTY OF ENGINEERING AND PHYSICAL SCIENCES
Optoelectronics Research Centre

Cathodoluminescence of nitrogen vacancies in nanodiamonds and plasmonic nanostructures

By

Hao Li

Thesis for the degree of Doctor of Philosophy

April 2021

UNIVERSITY OF SOUTHAMPTON

ABSTRACT

FACULTY OF ENGINEERING AND PHYSICAL SCIENCE

Optoelectronics Research Centre

Doctor of Philosophy

CATHODOLUMINESCENCE OF NITROGEN VACANCIES IN NANODIAMONDS AND PLASMONIC NANOSTRUCTURES

by Hao Li

Emission and scattering of light by nanostructures depends strongly on the ambient dielectric properties resulting in phenomena, such as Purcell enhancement of radiation or emission suppression. Free-electron beams have emerged as the ideal probe for the investigation of such effects and have been used extensively for the characterization of plasmonic and dielectric nanostructures, shedding light to the underlying physical mechanisms and leading to new applications, such as nanoscale electron beam driven light sources.

In this thesis, I have investigated the emission properties of nitrogen-vacancy (NV) centres in nanodiamond and plasmonic nanostructures by cathodoluminescence. In particular, I have demonstrated by time-resolved cathodoluminescence (TR-CL) and control of the emission of NV centres through tailoring the dielectric properties of the host medium (including dielectric, plasmonic). I have also analyzed the underlying mechanisms linking dielectric properties, geometry and emission statistics. Conversely, I have demonstrated that machine learning can be employed to retrieve information about arrangements of plasmonic nanostructures for the their emission properties and vice versa. In particular, in this thesis I have, for the first time:

- Employing TR-CL to experimentally demonstrate a two-fold enhancement of the decay rate of NV centers on a diamond-covered Si substrate as opposed to a bare Si substrate. I link the emission statistics to the interplay between the excitation of substrate modes and the presence of non-radiative decay channels and show that the radiative decay rate can vary by up to 90% depending on the thickness of the diamond film.

- Employing TR-CL to experimentally demonstrate that the distribution of the decay rates of NV centers in nanodiamonds can be made narrower by as much as five times once the nanodiamonds have been embedded into chalcogenide films. This result paves the way towards the dynamic control of the emitter decay rate through the phase change properties of chalcogenides.

- Numerically demonstrated that the cathodoluminescence spectra emitted by sets of subwavelength plasmonic apertures can be predicted from their configurations and, inversely, information about the configurations of subwavelength plasmonic apertures can be inferred from the cathodoluminescence spectra they emit.

Contents

List of figures

DECLARATION OF AUTHORSHIP

I, Hao Li, declare that the thesis entitled "Cathodoluminescence of nitrogen vacancies in nanodiamonds and plasmonic nanostructures" and the work presented in the thesis are both my own, and have been generated by me as the result of my original research. I confirm that:

- this work was done wholly or mainly while in candidature for a research degree at this University;
- where any part of this thesis has previously been submitted for a degree or any other qualification at this University or any other institution, this has been clearly stated;
- where I have consulted the published work of others, this is always clearly attributed;
- where I have quoted from the work of others, the source is always given. With the exception of such quotations, this thesis is entirely my own work;
- I have acknowledged all main sources of help;
- where the thesis is based on work done by myself jointly with others, I have made clear exactly what was done by others and what I have contributed myself;
- parts of this work have been published as the journal papers and conference contributions listed in Appendix A Publications.

Signed: _____

Date: _____

Acknowledgements

The work presented here in this report would be impossible without the constant help and support of my supervisors, collaborators, friends and fellow group members at the Optoelectronics Research Centre. I would like to acknowledge their contribution, namely:

- My supervisors, Dr. Nikitas Papasimakis, Prof. Nikolay Zheludev, Dr. Vassili Fedotov and Dr. Jun-Yu Ou, for their invaluable guidance, insight, and patience throughout my research. Dr. Papasimakis is a fantastic supervisor, who is very helpful in every aspect of my research from theory, simulation, sample fabrication, setting up experiments to writing journal papers. There are so many things that I will never forget, such as training me build and optimize COMSOL models hand by hand, helping me clean my first sample substrate in cleanroom, training me use use the laser in the lab, helping me very patiently prepare my oral presentation in NANOP 2019, which is my first international conference. Prof. Zheludev is both a great scientist and mentor, providing inspiration and guidance for my research during the group meeting. Dr. Fedotov is a very nice and humorous co-supervisor who is always give me encouragence infront of the delimma, how patiently he trained me design the metasurface, encourage me to bravely raise the questions during the scientific presentation. Dr. Ou is a fantastic co-supervisor who is an experiment expert, patiently training me use the SEM and prepare the presentation for group meeting, helping me maintenance the SEM, how patiently he help me solve the experiment problems. Dr. Ou is also a very good friend to talk during the beer time and coffee time every week.

- My collaborators, without whom some of my work would not have been possible. Especially Prof. Kevin MacDonald for providing me the conveneince of using SEM. Dr. Behrad Gholipour for helping me characterize the SbTe film. Dr. Davide Piccinotti for helping me fitting the ellipsometry measured data. Dr. Oleksandr Buchnev for fabricating the metasurface samples. Dr. JinKyu So for his suggestions about Hanbury Brown-Twiss (HBT)-CL experiment. Dr. Brendan Clarke for training me use the CL system. Dr. Giorgio Adamo for his suggestion about electron beam size measurement. Dr. Vassili Savinov for helping me understand the dipole radiation theory. Dr. Parikshit Moitra for his suggestion about ENMZ simulation.

- The staff and members of the ORC. In particular Glenn Topley for solving lots of my lab problems, like filling liquid nitrogen, making sample plates with 3D printing, etc. Neil Sessions, Dr Libe Arzubiaga Totorika, Christopher Craig for providing training in the use of the ORC cleanroom facilities. Mike Bartlett for safety of laser. Niel Fagan for filling up liquid nitrogen for me every week. Mark lessey for the safety notification during emergency. John Ure for protecting lab users from infection during COVID-19 pandemic. Paula Smith for her kindly and patiently help to any office errands. Toni Couvoussis for booking flights and hotels for

international conference. The excellent work of the staffs in ORC guarantees my research be finished finally.

- My contemporaneous colleagues, whose helps and accompanies are very important to my Ph.D experience. In particular Dr. Apostolos Zdagkas and Dr. Angeliki Zafeiropoulou for training my English during every day lunch time in common room in the past four years. Many thanks to all my friends in the nanophotonics & metamaterials group, Jinxiang Li, Tongjun Liu, Jie Xu, Dr. Qiang Zhang, Dimitrios Papas, Resmi Ravi Kumar, Sergei Kurdiumov, Yu Wang, Dr. Yaonan Hou, Dr. Angelos Xomalis, Dr. Pablo Cencillo Abad, Tiberius Georgescu, Dr. Artemios Karvounis, Dr. Maria Papaioannou, Dr. Yijie Shen, Dr. Shankar Pidishety, Dr. Tanchao Pu, Xingguang Liu, Dr. Guoqiang Lan, Dr. Yusuke Nagasaki, Dr. Bo Qiang, Dr. Wei-Yi Tsai, Dr. Ren Wang, Prof. Liwei Zhang, Dr. Huifang Zhang, Prof. jinfeng Zhu, Dr. Minhua Li, Dr. Tiago Martins.

- My friends in ORC, who give me pleasure in my spare time. In particular, I would like to thank my housemates Dr. Sheng Zhu, Dr. Qiang Fu, Dr. Zhengqi Ren. Many thanks to Dr. Fernando Guzman, Dr. Norberto Javier Ramirez Martinez, Dr. Soonki Hong, Dr. Naresh Kuman, Dr. Kasia Grabska, Dr. Wanvisa Talataisong, Dr. Teerapat Rutirawut, Dr. Jake Prentice, Dr. Francesco De Lucia, etc.

- My family, whose encouragement and support have been a continuing source of inspiration in completing my studies. In particular, I would like to thank my parents, who not only cultivated my strong interest in acquiring knowledge, but also gave me a pious refuge in the long journey of life, and also provided me with great support and help to successfully complete my PhD's study. I would like to thank my old sister and young brother, who always support me during my whole education career. Finally and most importantly, I would like to thank my wife and my daughter, who are the most valuable asset in my life. In the future, I will study and work harder to live up to their expectations.

Chapter 1

Introduction

1.1 Motivation

This work aims to identify routes towards controlling the emission and scattering by nanostructures in dielectric, plasmonic, and epsilon-near-zero (ENZ) media. In particular, as nanostructures become smaller and smaller the laws of quantum mechanics will become apparent in their interaction with light. In this limit, continuous scattering and absorption of light will be supplemented or replaced by resonant interactions when the photon energy matches the energy difference between discrete internal (electronic) energy levels. In atoms, molecules and other 'quantum confined' systems, these resonances are found at optical frequencies [1]. Because of their small size, quantum systems are ideal probes for local field distributions. Furthermore, when they interact with light the quantum nature of the internal states gets encoded into the statistics of the emitted light. An example of such systems is nitrogen vacancy centres, which are promising candidates for single photon sources.

The nitrogen vacancy (NV) centres are point defects in diamond consisting of substitutional nitrogen–lattice vacancy pairs [2]. NV centres in diamond supply long spin coherence lifetime and serve as stable solid single photon sources at room temperature [3, 4], which play a potentially important role in quantum technologies, such as quantum computing and quantum information processing. NV centres in nanodiamonds (NDs) can be readily integrated with various photonic systems, such as photonic crystals [5], optical fibres [6]. There is a problem, however – the lifetimes of NV centres in NDs exhibit large variation being strongly affected by radiative rates, nonradiative rates and quantum efficiencies. Therefore, understanding the emission of NV centres in ND-dielectric environments requires a large set of measurements with good statistics. Here, I use a home-built time-resolved cathodoluminescence (TR-CL) system as a test platform, which enables the experimental study of the NV centres lifetime statistics when their emission properties are modulated by changes in the dielectric environment. CL- spectral and temporal measurements are involving and not easily accessible. Artificial intelligence (AI) provides unique opportunities for the prediction of emission spectra of plasmonic structures without the need for full CL spectroscopic setup. Indeed, AI has attracted significant attention in the nanophotonics community [7-10]. Supervised machine learning algorithms have been implemented to classify single versus multiple NV centres in NDs using the sparse autocorrelation data [11]. Here, I use AI to predict the CL spectrum emitted by subwavelength plasmonic apertures. This chapter constitutes an overview of the main concepts explored in the thesis, including a short overview of the cathodoluminescence, research progress on NV centres in NDs for nanophotonics, a description of the electron microscopy for NV centres in NDs and a short overview of machine learning for nanophotonics.

1.2 Cathodoluminescence

Cathodoluminescence (CL) refers to the light or electromagnetic radiation arising from electronic recombination following excitation by a fast electron beam, commonly used to characterize materials with the nanometer resolution based on their dispersed fluorescence spectra. CL has been one of the most successful techniques for interrogating NV centres in diamond [12, 13]. There are two different kinds of excitations underpinning CL of metallic materials and of semiconductors. When an electron beam excites a semiconductor, various signals are generated as shown in Fig. 1.1. The incident electrons dissipate their energy into different channels, including emission of X-rays, generation of e-h pairs, generation of Auger electrons (when a fraction of primary electrons is absorbed in bulk material), and emission of photons (when the generated e-h pairs recombine radiative). However, the CL of metallic materials results from the coupling of plasmon modes to the far-field.

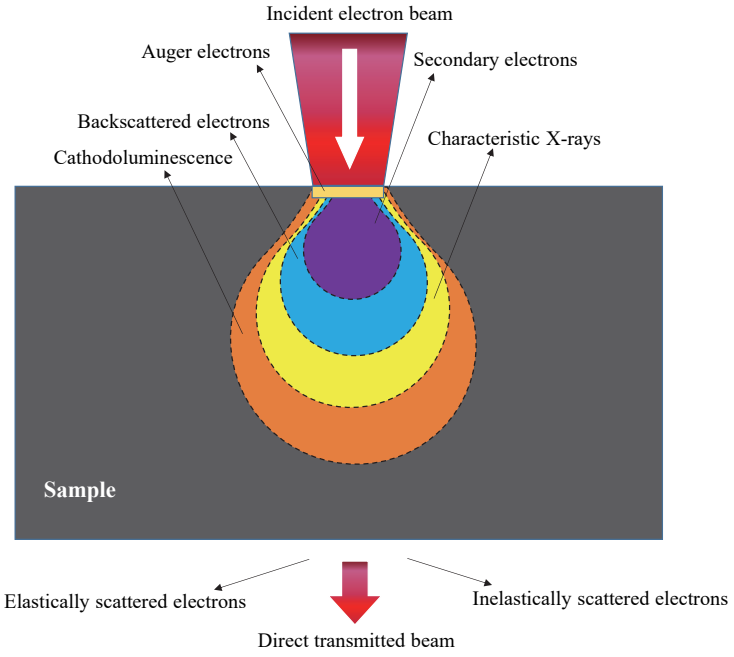

Figure 1. 1. Electron beam – matter interactions. Schematic illustration of signals generated by the interaction of an electron beam and a sample.

When a fast electron impinges on a metal surface, the sudden annihilation of its image acts like an induced dipole that produces radiation, which is known as transition radiation (TR). The TR angular pattern is similar to the far field radiation pattern of a vertical point dipole on a surface [14], as shown in Fig. 1.2.

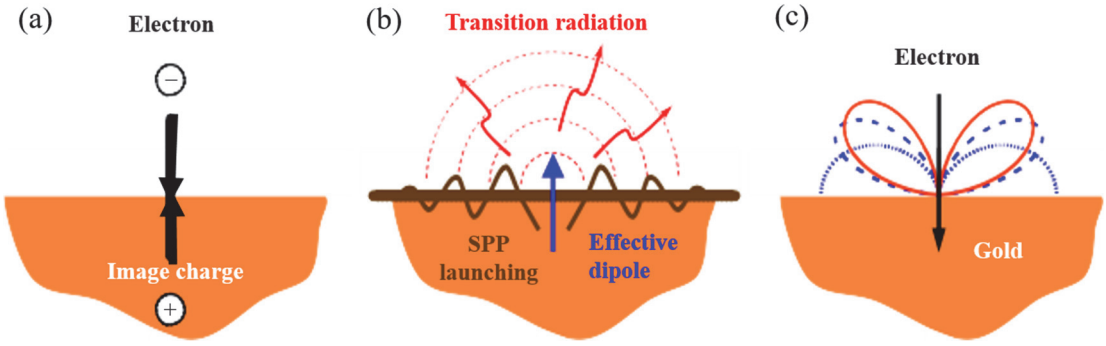

Figure. 1.2. Transition radiation. (a) An electron cancels its image charge when it crosses a metal surface. (b) This cancellation happened in (a) creates an effective dipole that can emit light and generate surface plasmon polaritons (SPP). (c) The dipolar angular pattern (solid curve) resulted from transition radiation is similar to the angular pattern when a dipole normal to the surface (dashed curve). The dotted curve shows the pattern of the dipole in the absence of the surface. The angular pattern is calculated for 200 keV electrons impinging on a planar Au surface and at the light wavelength of 600 nm. Figure adapted from ref. [14]

1.3 Cathodoluminescence of plasmonic systems

The high spatial resolution of the CL technique enables the analysis of resonant modes in the plasmonic nanostructure, for instance, by studying the propagation properties of surface plasmon polariton (SPP) on metallic nano-gratings [15, 16]. A single gold nanowire supporting plasmonic eigen modes can be analysed by CL technique [16]. High energy electron beams can excite all resonant modes in metallic nanostructures. For instance, both the even and odd modes of an ultrathin strip nano-antenna can be observed by CL while only the odd mode can be observed in the traditional light scattering experiment [17]. The coupling properties of plasmonic structures can be revealed by CL, such as studying the mechanisms of Fano resonance in coupled plasmonic systems [18]. There is a difference between scattering spectrum and CL spectrum in clusters of plasmonic nanodisks because Fano resonance can be excited by light but cannot be excited by an electron beam. The CL images of a cluster change with the probe wavelength: there is higher intensity in the nanodisks at the edge of the cluster at the wavelength of 660 nm while there is much higher intensity at the centre of the cluster at wavelength of 770 nm, as shown in Fig 1.3 (a)-(c) [19]. The peak wavelength of the CL spectrum in the centre of the cluster is redshifted compared the CL spectrum at the edge of the cluster (see Fig 1.3 (d)), which is due to the different coupling between bright and dark plasmonic modes. The absence of polarization control in the case of electron beam excitation does not allow Fano resonance (which appears in the case of light excitation), but there are two discrete non-Eigen modes. Light excitation yields a bright mode, while electron excitation generates a superposition of a dark and bright modes.

Even the coupling among the needles of a gold nanoflower can be studied by CL [20]. Unlike light excitation, which usually excites the whole nanoflower, the focused electron beam acts as a local probe engaging different locations inside the nanoflower and exciting resonant plasmonic modes. As figure 1.3 (e) shows, five different positions A-E were selected to excite

the coupled plasmonic modes. There are differences in the CL intensity and the peak wavelength in these five CL spectra and CL intensity becomes higher when the resonance wavelength nears the absorption peak. The small angle difference results in the strong coupling of needles in the gold nanoflower. This type of CL study is very important for understanding the mechanisms of the excitation of plasmonic modes in 3D nanostructures by an electron beam.

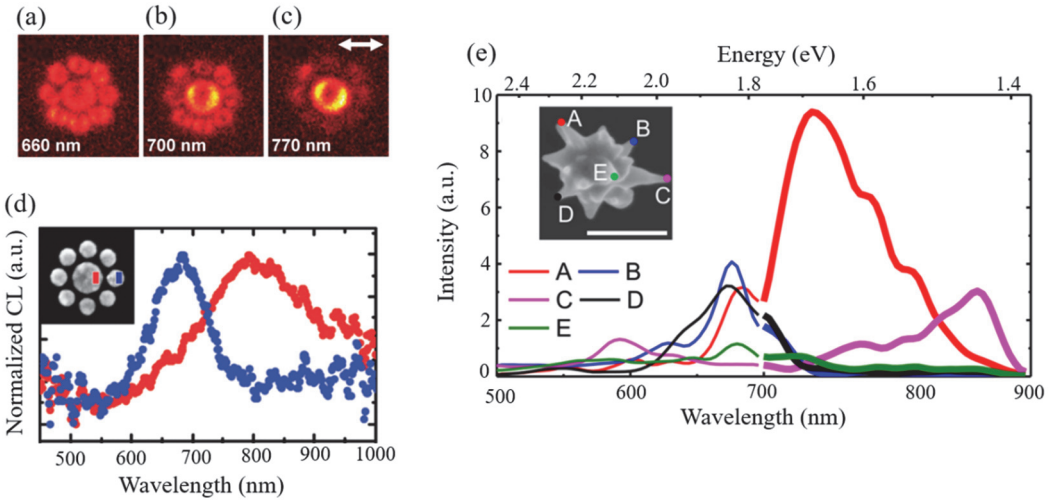

Figure 1. 3. CL of plasmonic nano-systems. Polarized, wavelength-selected CL images of a nonamer at (a) 660, (b) 700, and (c) 770 nm. Arrow indicates analyzer angle. (d) CL spectra where the electron beam is exciting the center particle (red) and a particle in the outer ring (blue). The inset shows an SEM image of a nonamer with blue and red squares to indicate the location of the beam for the blue and red spectra, respectively, figure adapted from ref. [19]. (e) Experimentally acquired CL spectra from different tip apex regions marked as A−E of the gold nanoflower. The inset SEM image shows the e-beam impact points with different colored dots, figure adapted from ref. [20]

1.4 Nitrogen vacancy centres in diamond nanocrystal

Diamond presents various important physical properties, such as wide energy bandgap at room temperature, optical transparency from deep-ultraviolet to the infrared, high mechanical strength, high thermal conductivity, bio-compatibility and robustness in a chemical environment. Such properties make diamond a good candidate for various applications ranging from semiconductor devices, bioscience, to material engineering, etc. More than 500 optically active color centers in diamond have been discovered [21], which has led to great advances in the past decades in the field of diamond photonics, holding promise for quantum information applications. Among them, nitrogen-vacancy (NV) centers have attracted the most research interest, because they offer a long spin coherence lifetime and serve as stable solid single photon sources at room temperature [3, 4]. NV centre's electron-spin has a long coherence time (1.8 ms [22]) and can be optically initialized and reliably manipulated using microwave fields [2], its spin can serve as a long lived spin qubit, whereas the emitted photons can serve as flying qubits. This make it be able to interface spins and photons, which paves the way to optical quantum information processing. Morever, the sensitivity of an NV center magnetometer can be directly linked to the photon emission rates and collection efficiencies [23], which makes it is very important to control the emission rates of NV centres. An NV centre is a point defect in

diamond consisting of a substitutional nitrogen–lattice vacancy pair, as shown in Fig. 1.4 (a) [2]. Two charge states are known for NV centers, namely NV^0 and NV^-. They exhibit zero phonon lines (ZPLs) centered at 575 nm and 637 nm with characteristic broad phonon sidebands (PSBs), which at room temperature extend from 580 to 650nm and 650 to 800 nm respectively, as shown in Fig. 1.4 (b). Bidirectional switching occurs between the NV^0 and NV^- centres [24]. A prerequisite condition for next-generation quantum sensing, communication, and computing is the precise modulation of the charge states of NV centers in diamond. Several methods can help to achieve the conversion of NV^0 into NV^-. They include selective oxidation with surface exposure to oxygen atmosphere [25], ultrafast synthesis technique [26], in-plane Schottky junctions [27], engineering photonic environment [28], optical controlled [24, 29, 30] and electron-induced [31].

Precise tuning of these centers in highly concentrated NV-diamonds using photons, phonons, and electrons has been achieved [26]. After single NV center in diamond was for the first time at room temperature with scanning confocal optical microscopy in 1997 [32], the detection of single centres soon enabled demonstrations of photostable single photon generation in simple experimental configurations [3, 4]. One year later, a nanodiamond (ND) containing a single NV centre was also observed the photon antibunching with very low background light, as shown in Fig. 1.4 (c) [33]. Recently, a method for rapid classification of single NV centres in ND enabled by machine learning has been developed [11]. This method has 95% classification accuracy and is about 100 times faster than the conventional approach. The lifetime time of the NV^- centre in bulk diamond has been determined as 13±0.5 ns for natural type Ib diamonds [34], while the intrinsic lifetime of NV^0 centre in bulk diamond is measured as 19 ± 2 ns [35].

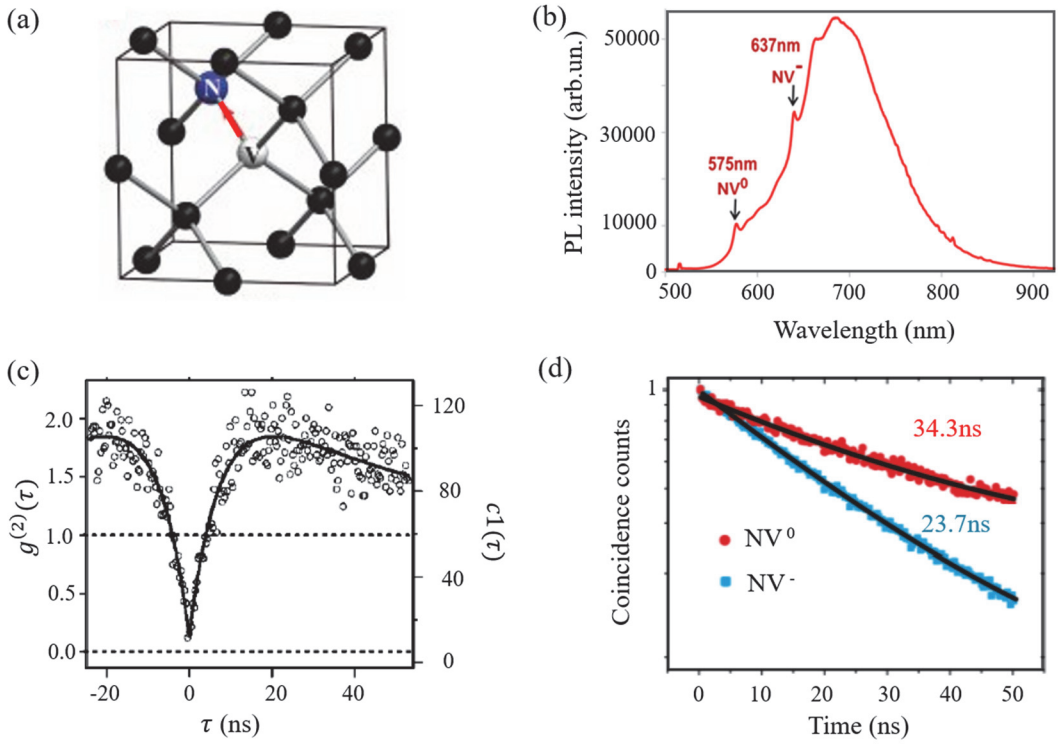

Figure 1. 4. Photonic properties of NV centres in diamond. (a) Crystal structure of a NV centre. (b) The mission spectrum from NV centre. (c) Experimental antibunching curve showing single photon emission of NV centre in ND, figure adapted from ref. [33]. (d) Exemplary fluorescence lifetime measurement for NV^- and NV^0 in NDs, figure adapted from ref. [36].

The lifetime of NV center in ND is longer than in the bulk diamond [33] due to the size-dependent quenching of the NV radiative emission [37]. The lifetime of NV centre in ND is also sample dependent [36, 38, 39]. There are even significant differences between different ND types, as shown by comparative studies in [38, 39]. There are also two distinct decay times of negative and neural charge states, as illustrated in Fig. 1.4(d). The Mie resonances of NDs themselves can also affect the lifetime of NV centres they host. There are fundamental eigenmodes of subwavelength NDs (see Fig. 1. 5 (a)) [40] The eigenmodes reveal themselves as scattering resonances (see Fig. 1. 5 (b)), which depend on particle size. Correspondingly, the Purcell enhancement of the NV centre emission also depends on particle size. The dependence of Purcell factor on the position of NV centre in an ND and the size of an ND is illustrated in Fig. 1. 5 (c). In [41] it has been experimentally demonstrated that there are decay rate enhancements for NV centres in NDs when the NDs act as active nanoantennas coupled to their Mie resonances (see Fig. 1. 5 (d)). Hence, it should be easy to improve the efficiency of ND-based sensors and single-photon sources by choosing NDs of optimal size and shape.

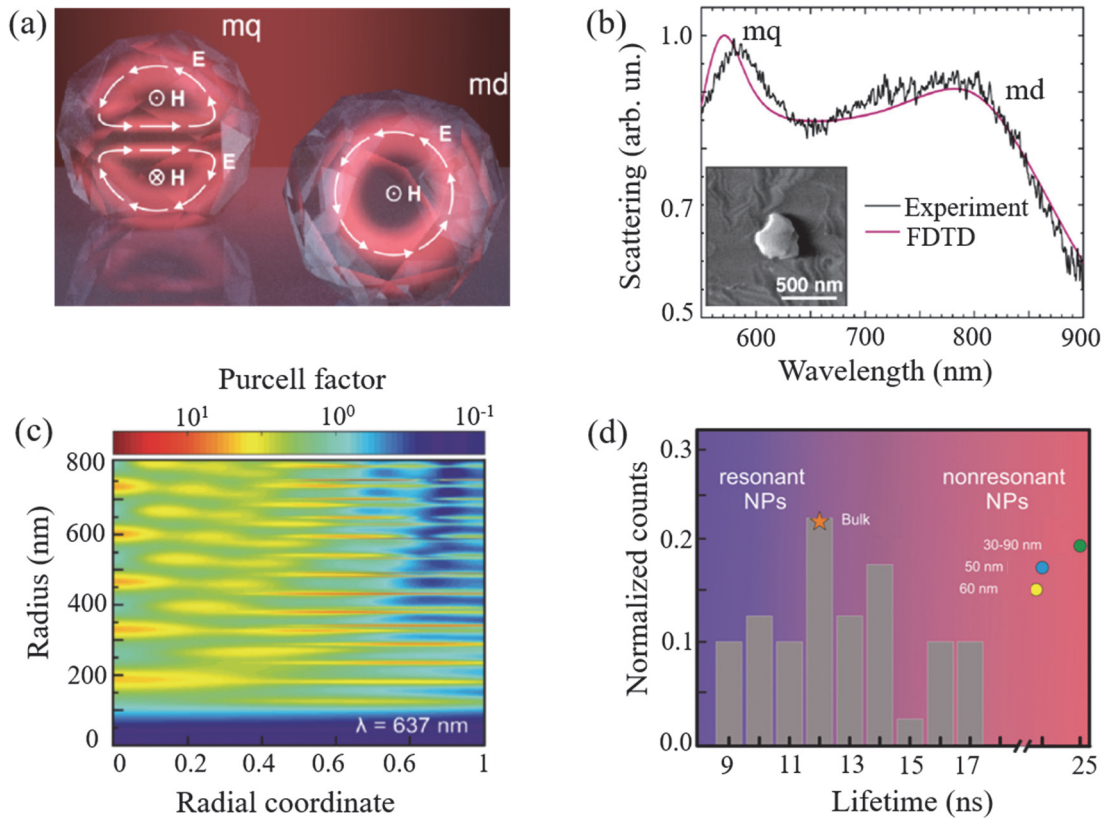

Figure 1. 5 Mie resonances in NDs enhance decay rates of NV centres. (a) Schematic representation of the fields in NDs upon excitation of the magnetic dipole (md) and magnetic quadrupole (mq) modes. (b) Unpolarized scattering spectrum from a typical ND (a scanning electron micrograph is shown in the inset) and FDTD simulated spectrum of scattering by a sphere with a diameter of 320 nm under the experimental conditions of the collection. (c) Purcell factor describing the enhancement of radiative emission for the ND with an NV^- center. The NV^- center is located at different positions along the ND radius. (d) Lifetime histogram for 40 NDs with different spectral positions of resonances relative to the NV center luminescence spectrum. The star shows the lifetime of the NV^- center in a bulk diamond. Figures (a-b) adapted from ref. [40], figures (c-d) adapted from ref. [41].

Despite the small size of NDs forming an aggregate, NV centers in the aggregate exhibit spin properties comparable to similar sized NDs grown by other methods, but with brightness enhanced by a factor of 2 [42]. NV centres have been usually observed in aggregated and milled NDs, and they also have been observed in very small isolated NDs. The first direct observation of NV centres in discrete 5-nm NDs at room temperature has been reported in [43], including evidence for blinking which can be controlled by modifying the surface of the NDs. Several different types of NDs have also been characterized in order to find the best sample to be used in further experiments with metamaterials [38]. Stable bright NV centers in NDs could enable quantum optics with metamaterials.

1.5 Controlling the decay rates of nitrogen vacancy centres in nanodiamonds

Controlling the emission rates of NV centres in NDs is crucial for their perspective application in quantum technologies. In the simplest case, the emission rates can be influenced by the

substrates that NDs are sitting on. Guiding emitted photons by waveguides and optical fibers, which is required by applications in quantum information, is also related to the control of emission rates. An increase in the emission rate can be achieved by increasing the local density of states (LDOS) in the vicinity of NDs, which leads to faster photon emission and shorter lifetimes. According to the geometries of the systems that NDs are embedded in, the dielectric environment can be classified as a uniform dielectric, semi-infinite structure and cavity. In particular, resonators and cavities are typically used for enhancing LDOS given their relatively high Q-factors. I discuss the research progress in each case in the following section.

1.5.1 Nanodiamonds coupled with planar systems

The photoluminescence (PL) of a single NV center in an ND can be significantly enhanced when the ND sits on a continuous gold nanofilm rather than a glass substrate [44] (see Fig. 1.6(a)). At the same time the lifetime of NV centers decreases indicating total decay rate enhancement. The decay rate enhancement is caused by the enhancement of the electric field via the excitation of a surface plasmon and the energy exchange between the excited state of NV centers and the surface plasmon. There is a large variation of lifetimes of NV centres in NDs even when they are placed on the same substrate. For instance, the lifetime on the coverslip varies from ~10 ns to 30 ns, as shown in Fig. 1.6(b). Multilayer metamaterials not only not only enable broadband enhancement of the decay rate for a single NV center in NDs but also make the lifetime distribution narrower [45]. A multilayer metamaterial fabricated as an epitaxial metal/dielectric superlattice consisting of CMOS-compatible ceramics, such as titanium nitride (TiN) and aluminium scandium nitride (AlxSc1-xN), also shows similar properties, which makes it a key component of perspective CMOS-compatible integrated quantum sources [46].

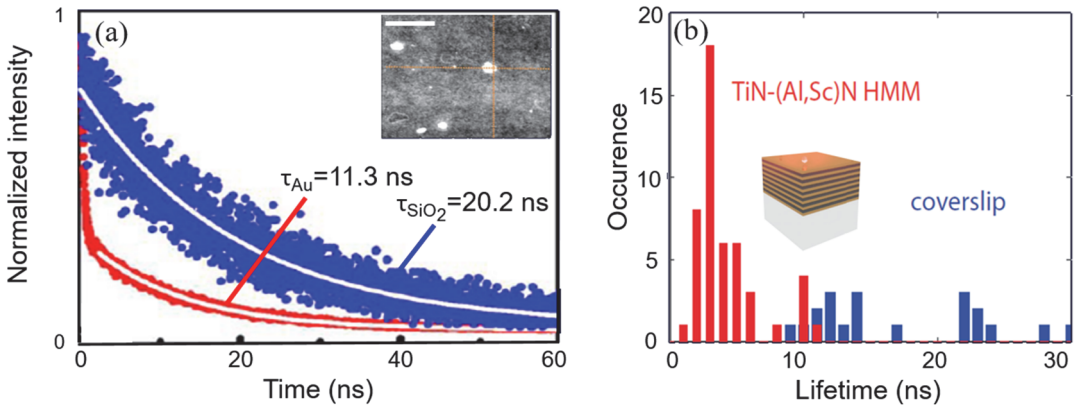

Figure 1. 6. Lifetimes of NV centres in NDs on gold film and multilayer metamaterial. (a) Decay traces of NV centres in NDs on gold film and SiO_2 respectively. Inset is the atomic force microscope (AFM) image of ND on a gold film, scale bare is 100 nm, figure adapted from [44]. (b) Lifetime distributions of NV centres on hyperbolic metamaterial and coverslip respectively, figure adapted from [45].

1.5.2 Nanodiamonds coupled with waveguides and optical fibres

Coupling photons emitted by NV centres to waveguides and optical fibers is necessary to make NV centers operate as single photon sources and render them suitable for applications in

quantum telecommunications. Recently, a hybrid GaP-diamond material system consisting of high-index GaP (n_{GaP} = 3.3) thin films on top of the diamond was used to demonstrate optical coupling between NVs close to the diamond surface and ridge waveguides patterned in the GaP film (see Fig. 1.7(a)) [47]. Because of the enhanced LDOS in the near field of the GaP waveguide modes, the relatively efficient evanescent coupling between NVs and the GaP waveguide can be observed. GaP-diamond photonic crystal nanowire waveguides provide three-dimensional confinement and it has been numerically shown that only can they be efficiently coupled to individual NVs but also have an efficient broadband collection of NV emission [48]. These types of waveguide structures can be fabricated using existing materials and processing techniques. High transparency of dielectric waveguides facilitates information transport over long distances but the corresponding waveguide modes are diffraction-limited in their cross-sections [49]. When light interacts with metal surfaces, it couples with free electrons and can form propagating excitations knowns as surface plasmon polaritons (SPPs). SPPs can produce strong electric fields localized to subwavelength distance scales [50]. An NV centre coupled to a silver nanowire (NW) excites a single SPP, which not only enhances the emission rate of the NV centre but also exhibits both wave and particle properties [51]. However, such a nanowire-ND system was not deterministically assembled and therefore it is difficult to estimate with certainty the enhancement of emission rate the system provides. By using the atomic force microscope (AFM) operating in contact mode one can move a chosen diamond nanocrystal across a NW in a controllable way. This technique is used to position a single ND near a silver NW with high accuracy and thus enables the complete control of coupling between the NV center and propagating SPPs. The excitation of a single SPP is witnessed as well with a total rate enhanced by a factor of 4.6 [52]. By using AFM-assisted nano-assembly technique, placing an ND in the gap between two end-to-end aligned silver NWs becomes possible [53]. This technique also helps to realize an efficient coupling of an NV center to an easily accessible gap plasmon mode, which enhances the spontaneous emission rate of NV centre by a factor of 8.3 [54]. Moreover, this technique enables the generation and controls the routing of a single SPP excited by NV centre from one NW to another (see Fig. 1.7(b)) [55]. The most important challenge in exploiting plasmonic circuitry for quantum-optical networks is the inevitable SPP propagation loss due to absorption (ohmic loss). Dielectric-loaded surface plasmon polariton (DLSPP) waveguides confine SPPs laterally by using dielectric ridge waveguides patterned on a flat metal film can serve as a bridge between nanoplasmonic components and dielectric waveguides. Furthermore, DLSPP waveguides can be fabricated using a standard lithography process. A top-down fabrication technique for deterministic positioning of DLSPP waveguides to incorporate NDs with a single NV center has been experimentally demonstrated (see Fig. 1.7(c-e)) [56]. Here the decay rate enhancement by a factor of ~5 on average has been observed. Also, β factor, defined as the fraction of total emission into the plasmonic mode, is estimated to be 0.58 ± 0.03.

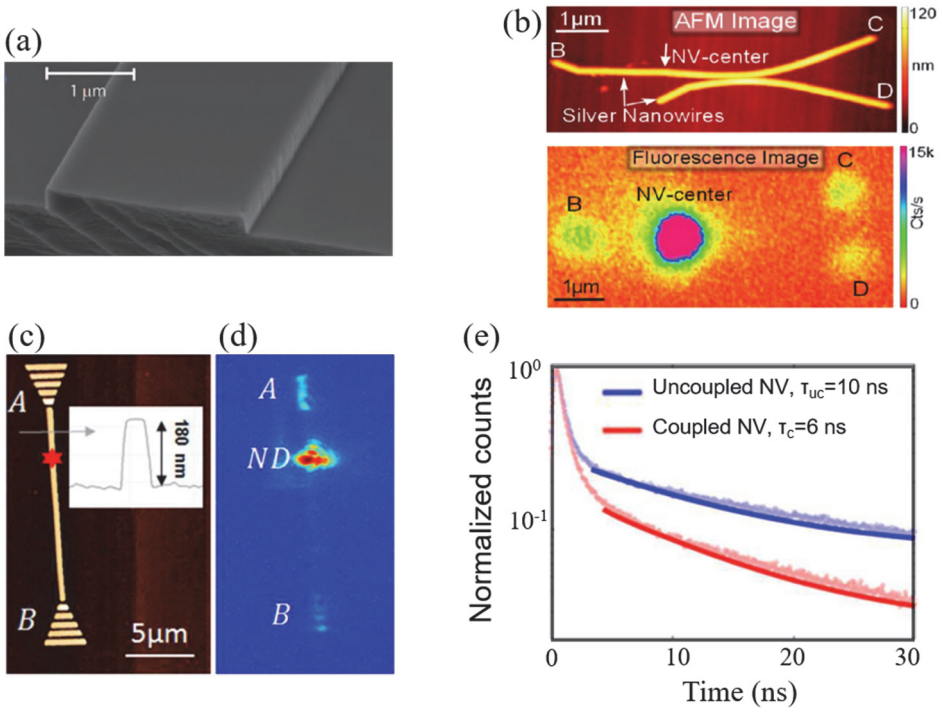

Figure 1. 7. Nanodiamond with NV centres. (a) GaP waveguide deposited on single-crystal diamond, figure adapted from ref. [47]. (b) Silver nanowires as plasmonic waveguides and beam splitter for single photons: an NV center is placed close to a silver nanowire (sample topography see upper panel). Light is guided by the nanowire as evident from the fluorescence image in the lower panel: emission is not only recorded from the position of the NV center, but also from the ends of the wire (points B and C). Furthermore, the beam is split as evident by light emission from the second wire's end (point D), figure adapted from ref. [55]. (c) AFM image of the fabricated dielectric-loaded surface plasmon polariton (DLSPP) waveguide. The inset shows thickness profile across the gray arrow and indicates a 180 nm height for the waveguide [56]. (d) CCD camera image of the whole structure where the ND is excited and a emission image of the focal plane is taken is presented. Emission from the gratings at the ends of the waveguide, when ND is excited, confirms the coupling of NV center to the waveguide mode. (e) The lifetime of the NV center before (blue) and after (red) coupling, figures (c-e) adapted from ref. [56].

The efficient and small scale coupling of a single NV centre to a fiber network is an essential requirement to build complex quantum systems. Depositing NDs on the end faces of optical fibers, capturing the emission generated by NV centres into the fiber and controlling the concentration of NV centres during the chemical vapor deposition of NDs are all critical steps in developing a fiber coupled single-photon source [6]. Other efforts have been made by depositing preselected NDs on specially prepared fibers [57], by indirectly coupling NV centers via a toroidal resonator to a fiber [58], or by placing a preselected ND directly on the fiber facet to achieve near-field coupling of a single NV center in a bottom-up approach [59]. Tapered optical fibers (TOFs) with a subwavelength waist are promising one-dimensional nanophotonic waveguides that can provide efficient coupling between their fundamental mode and NV centres placed inside them. In particular, a lower and upper bound for the coupling efficiency of (9.5±0.6)% and (10.4±0.7)% can be obtained by the on-demand positioning of a single ND onto the nanofiber-waist with the help of an AFM, as illustrated in Fig. 1.8(a) [60]. Single NDs deposited on a TOF with the diameter of 273nm provided a record-high number of 689±12kcps

single photons from a NV center via a single-mode fiber [61]. Numerical results have also shown that a maximum coupling efficiency of 53.4% can be realized for the two fiber ends when a dipole representing an NV is located at the center of the TOF [62]. A new approach is based on the coupling of a single NV centre to a fiber-based Fabry-Perot cavity, where the cavity can be easily tuned and thus enables the NV centre-cavity coupling to be continuously varied (see Fig.1.8(b)) [63]. By employing the fiber-coupled GaP microcavities the spontaneous emission decay of NV centres can measured [64]. Theoretically, the average Purcell factor due to fibre coupling is 2–3 times greater than that of free-space collection. In fact, optical collection from an NV center coupled to an optical fibre is more efficient than the approach that uses adiabatic power transfer between a TOF and a single-mode diamond micro-waveguide fabricated from high-quality CVD-grown diamond [65]. Tellurite is a promising base material for photonic structures since it has a wide transparency window (from 0.5 to 4 μm) and low transmission loss at the emission wavelengths of NV centres. Incorporating diamond with NV centers in tellurite glass opens the possibility of leveraging all of the designs of microstructured optical fibers. In [66] the researchers have taken tellurite glass through an optical fiber drawing process and demonstrated single photon emission from the drawn tellurite fibre. This demonstration renders diamond in tellurite glass as a new medium for quantum information.

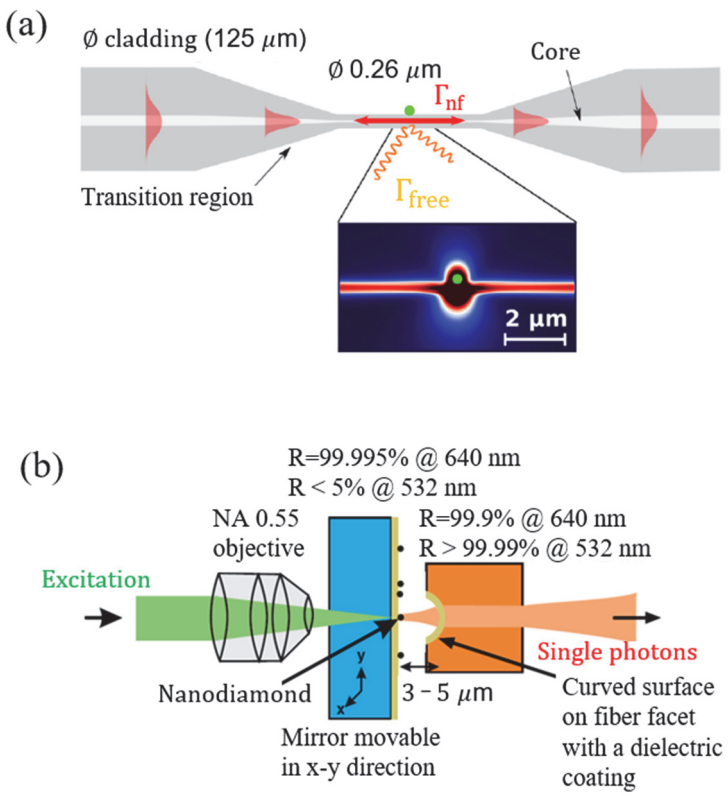

Figure 1. 8. Nanodiamond with NV centres coupled with fiber: (a) Tapered fiber coupling of NDs. A ND is placed onto the tapered region. A high coupling efficiency is feasible due to the strong evanescent field of the partially air-guided mode of the nanofiber. Via the taper, the evanescent mode and thus the single photons are converted into the mode of a standard single mode fiber, figure adapted from ref. [60]. (b) Fiber based microcavity for the coupling of single photons: NDs are placed on a highly reflecting, planar mirror. The second mirror is formed in the end facet of a glass fiber, into which the photons are collected. The fiber end facet is micromachined to form a concave surface and subsequently coated with a dielectric coating, figure adapted from ref. [63].

1.5.3 Nanodiamonds coupled with dielectric resonators and cavities

The coupling of NDs with NV centres to a cavity will enhance the emission into the ZPL, therefore enabling faster and brighter emission. Currently, the coupling between NV centers and dielectric cavities has been demonstrated in several different systems that can be divided into two main categories: (i) hybrid and (ii) monolithic all-diamond. Hybrid systems typically consist of cavities fabricated in non-diamond materials and are evanescently coupled to NV centers in NDs. On the other hand, monolithic, all-diamond systems are based on optical cavities fabricated directly in single crystal diamond substrates. Examples include microring resonators [67, 68], two-dimensional (2D) photonic crystal cavities (PCCs) [69] [70] and one-dimensional (1D) PCC [71]. Coupling the ZPL of a singe NV centre to the modes of microring resonators fabricated in single-crystal diamond enables ZPL enhancement by more than a factor of 10, as estimated from lifetime measurements [67]. Microring resonators are fabricated using standard semiconductor techniques and off-the-shelf materials, which makes them attractive for

integrated diamond photonics. Similarly, in [68] a large overall photon extraction efficiency (10%) was observed for a single NV centre embedded in a ring resonator with the quality factor of as high as 12600. The ZPL of a NV center is enhanced by a factor of ~70 when coupled to a 2D PCC fabricated in monocrystalline diamond using standard semiconductor fabrication techniques [69]. A 2D PCC with high-quality factor and cubic wavelength mode volume was directly fabricated in bulk diamond [70]. Quality factors of a 1D PCC can be as high as 6000 with the NV center's ZPL emission enhanced by a factor of ~7 in low-temperature measurements [71].

Hybrid integration of NDs and dielectric cavities typically involves NV centers in NDs evanescently coupled to cavities fabricated in non-diamond materials. Dielectric microspheres with ultrahigh quality factors are usually employed for coupling to NV centres in NDs [72]. The observation of the normal mode splitting indicates that there is a strong coupling between an NV center and whispering gallery mode (WGM) of a silica microsphere, which has an ultrahigh quality factor $Q>10^8$ [72]. Polystyrene microspheres provide WGMs with both large Q-factor and small mode volume, which is essential for observing the effects of quantum electrodynamics. With the help of a scanning near-field probe, NDs can be attached to a polystyrene microsphere and assembled on a coverslip one by one. A clearly modulated fluorescence spectrum and pronounced antibunching dip evidenced the coupling of a single NV centre to high-Q WGMs [73]. By characterizing a polystyrene microsphere using white light Mie-scattering it is possible to identify ideal partners in ensembles of polystyrene microsphere and NV-centres with finite size and finite defect density distributions, respectively, and couple them on-demand [74]. The first optical measurement of a single NV center in a three-dimensional (3D) PCCs fabricated by self-assembly of polystyrene microspheres reveals a photonic stopband that overlaps the NV PL spectrum. The NV centre lifetime increases by 30% due to coupling [75]. Similarly, opal photonic crystal surfaces composed of polystyrene microspheres on average can enhance the total emission rate by a factor of 1.5 [76]. Moreover, simulation results show that ~5-fold enhancement of the emission rate can be achieved by high-index silicon nanoparticles [77].

Dielectric microdisks also support high-Q WFGs, which are able to interact evanescently with the diamond substrate that contains NVs as well as with NDs containing NVs [78-80] An example of such a microdisk can be seen in Fig. 1.9(a). Using a fiber taper NDs can be placed in the near-field of a high-Q SiO_2 microdisk, which modifies the PL of NVs [79]. Unlike potonic crystals (PCs) in bulk diamond, dielectric PCs based on NDs are easier to fabricate. PCs in GaP scanned over PMMA film containing NDs with NVs is a novel technique for deterministic positioning of NVs on PCs, which allows addressing isolated NV centres [81]. For NDs with NVs placed directly on the surface of GaP PCs using AFM pick-and-place technique, a Purcell enhancement of the PL emission at the ZPL by a factor of 12.1 is observed (see Fig. 1.9(b-c)) [82]. The coupling between NV centers and PCs can also result in a strong enhancement of NV center emission at the cavity wavelength [79]. A three-dimensional dielectric resonator consisting of a microdisk and a waveguide has been fabricated via direct laser writing. The technique is based on exposing locally a photoresist containing NDs to focused ultrashort laser

pulses, which induce two-photon polymerization (see Fig. 1.9(d)) [80]. Usually, the coupling mechanism in hybrid systems engages evanescent fields and typically results in reduced coupling strength compared to the all-diamond approach, where the emitter is located in the field maximum [83]. Recently, NDs positioned inside a 1D PC based on a Si_3N_4 membrane exhibited efficient coupling to the PC with the β_λ-factor reaching values as large as 0.71 (see Fig. 1.9(g-h)) [83]. A fishbone-shaped 1D PCs cavity based on a Si_3N_4 membrane with a nanopocket located at the electric field maximum of its fundamental mode not only allows more efficient coupling between an ND and the cavity mode (with Purcell enhancement reaching ~50) but also enables better integration of the ND with the cavity compared to the AFM pick-and-place technique (see Fig. 1.9(e-f)) [84]. The nanopocket in this kind of 1D PCs can be replaced with a nanotrench, which will help to achieve higher Purcell enhancement [5].

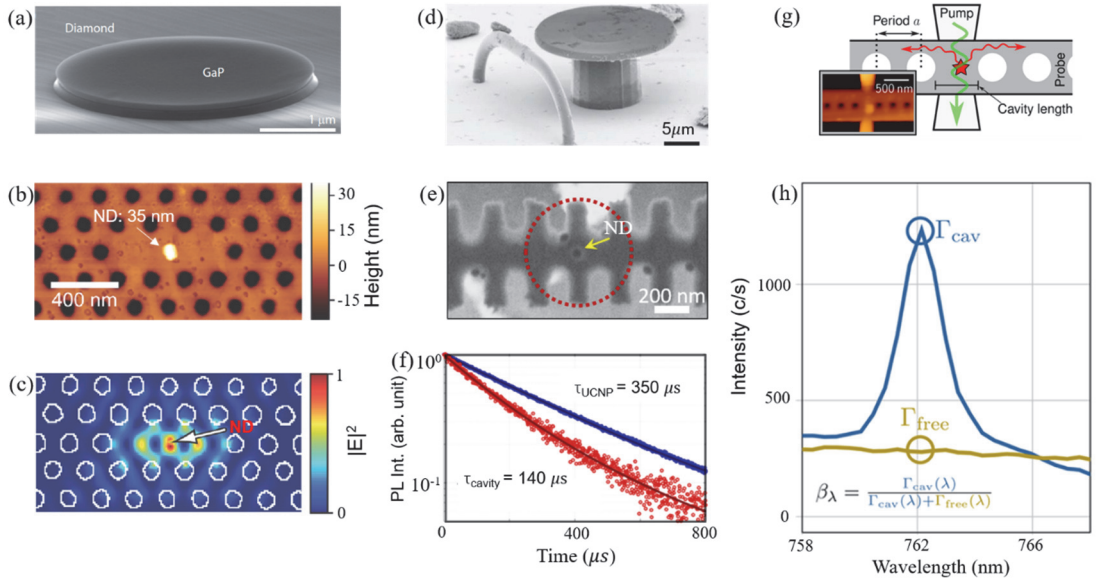

Figure 1. 9. Nanodiamond with NV centres coupled with dielectric resonators and cavities. (a) GaP microdisk deposited on single-crystal diamond, figure adapted from ref. [78]. (b) Atomic force microscopy (AFM) image of a diamond nanocrystal placed in a GaP photonic crystal cavity and (c) the simulated electric field profile of the cavity's fundamental mode, figures adapted from ref. [82]. (d) A scanning electron microscopy (SEM) image of a disc resonator and an arc waveguide, figure adapted from ref. [80]. (e) ND in the pocket, indicated by the yellow arrow. The red outline represents the approximate size and position of the pumping spot to identify particles that contribute primarily to the PL signal, figure adapted from [84]. (f) For the cavity with a particle in the pocket, a 20-fold PL enhancement at the resonance (668 nm) was observed. Lifetime measurements for cavities with a particle in the pocket, figure adapted from [84]. (g) Schematic of a photonic crystal cavity with an ND positioned in the interaction region. The 532 nm excitation laser is directed through the waveguide, where its evanescence field excites the ND off-resonantly. The emission of the ND is enhanced within the direction of the cavity (Purcell effect). The small inset shows an AFM image of a ND positioned inside the interaction region of the PhC cavity. (h) The free space emission spectrum of the ND cluster with off-resonant excitation for an excitation via the pump beam (yellow), and the same emission with ND in the cavity (blue), figure adapted from [83].

1.5.4 Nanodiamonds coupled with plasmonic resonators and cavities

Dielectric resonators can typically support high-Q resonances but are relatively large in size (one wavelength or larger), while plasmonic resonators are characterized by lower Q-factors but have much smaller (i.e., sub-wavelength) dimensions. Sub-wavelength confinement of optical fields in plasmonic resonators can strongly modify the spontaneous emission of the embedded NV centres despite having only modest quality factors. In [85] the researchers developed a general bottom-up approach to the fabrication of an emerging class of free standing ND-based hybrid nanostructures with external functional units represented by plasmonic nanoparticles. Here, the precise control of the structural parameters (including size, composition, coverage and spacing of the external functional units) was achieved. Schietinger et al firstly demonstrated that the emission properties of a single NV center can be controlled through coupling to plasmon resonances [46]. Electromagnetic field hot spots provide efficient near-field coupling between ND and gold nanoparticles and, despite the mismatch in their size and shape, yield an increase of the radiative decay rate by a factor of 5.8 and 8.9 for single gold nanoparticle-ND and gold dimer-ND systems, respectively. Gold nanoparticles and NDs also mutually enhance light emission when coupled to engage the surface-enhanced fluorescence process [86]. The positioning of an ND in the vicinity of a gold bowtie nanoantenna can also be used to tune the plasmonic spectrum of the nanoantenna on the order of a linewidth [54]. Plasmonic apertures decorated by cylindrical diamond nanoposts support modes with small modal volumes and can provide good spatial overlap between highly localized optical fields and NV centres due to nearly uniform field distributions in the transverse direction which results in enhancement of the spontaneous emission rate [87]. This kind of plasmonic apertures also promises great scalability. Theoretical calculations also show that an optimal plasmonic aperture can simultaneously enhance optical pumping by a factor of 7, spontaneous emission rates by Fp ~50, and offer collection efficiencies up to 40% [53]. Diamond-Ag nano-cavities consisting of periodic grooves in a Ag film filled with a dielectric material around a central aperture can also enhance the radiative decay rate of single NV centers [88]. When NDs are placed in the nanoscale gap between two Ag nanocubes in a dimer configuration one can achieve linearly polarized emission [89]. For two distributed 1D Bragg mirrors placed at opposite sides of a coupled NV centre and integrated with a dielectric-loaded SPP waveguide [90], a 42-fold enhancement of the decay rate via spontaneous emission can be achieved at the cavity resonance. The shortcomings of plasmonic nanostructures are high losses resulting from nonradiative quenching of excitation and plasmon absorption in metals. Recently, employing low-loss single-crystal Ag cube enabled the demonstration of ultrabright single-photon emission, where nanocavity-coupled NVs produced up to 35 million photon counts per second (see Fig. 1. 7 (a)) [91]. The intrinsic properties of single-photon systems render them as ideal tools for quantum enhanced sensing and microscopy. As an additional benefit, their size is typically on an atomic scale, which enables sensing with very high spatial resolution. In [92] the researchers report on utilizing a single NV center in an ND for performing 3D scanning-probe fluorescence lifetime imaging microscopy of a plasmonic nanorod. By measuring changes in the lifetime of a single NV centre, information on the LDOS is acquired at the nanoscale (see Fig. 1.10 (b)). Efficient and controllable funneling of photon streams from NV

centres is essential for interfacing nanoscale volumes with complex optical configurations exploited in quantum information and communication systems. Hybrid plasmon-NV centre coupled metasurfaces featuring circular nanoridges were proposed to funnel the photon emission along a given off-normal direction (see Fig. 1.10(c-d)) [93]. The design principle there relied on phase matching of circularly diverging surface plasmons excited by an NV centre to a well-collimated off-normal propagating photon stream, which was achieved in a modified bullseye antenna by displacing appropriately the centers of its circular nanoridges. Single photons carrying spin angular momentum (SAM), i.e., circularly polarized single photons, which are typically generated by subjecting a quantum emitter to a strong magnetic field at low temperatures, are at the core of chiral quantum optics enabling nonreciprocal single-photon configurations and deterministic spin-photon interfaces. A conceptually new approach to the room-temperature generation of SAM-coded single photons is described in [94]. It exploits an optical metasurface to transform nonradiative coupling between NV centres and surface plasmons into a collimated stream of single photons with the designed handedness (see Fig. 1.10(e-f)).

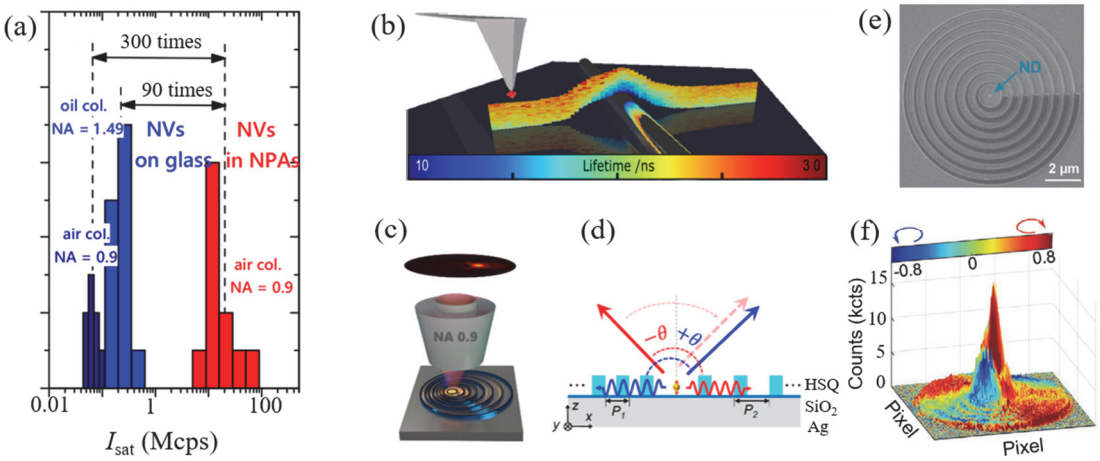

Figure 1. 10. Nanodiamond with NV centres coupled with plasmonic resonators and cavities. (a) State-of-the-art enhancement of emission from a single NV^- centre, resulting in over 1×10^6 counts/s at saturation, figure adapted from ref. [91]. (b) Two-dimensional stripe scan across a silver nanowire, color-coded lifetime data as a function of height and position perpendicular to a silver nanowire, the scale bar is 100 nm, figure adapted from ref. [92]. (c) Schematic of unidirectional and off-axis emission from a hybrid plasmonic-QE coupled system, figure adapted from [93]. (d) The cross-section view of the system in (c). The gratings with different periods on two sides can unidirectionally outcouple the counter propagating SPPs into oblique angles. e) SEM image of circular width-gradient nanoridges for generation of right-hand circularly polarized photons. The selected ND with many NV centers is situated in the center of circular nanoridges. f) 3D representation of the superimposed beam intensity and polarization far-field distributions, with the height reflecting the light intensity and the color indicating the polarization. The dominant peak is red-colored, demonstrating that the majority of photons carry the designed SAM, i.e., possess the right-hand circular polarization, figures (e-f) adapted from ref. [94].

1.5.5 Nanodiamonds coupled with graphene

Fluorescence resonance energy transfer (FRET) from a donor molecule in an excited state to a suitable acceptor molecule is an interesting process which widely occurs in various material systems. Since the energy transfer from NV centers to various energy acceptors in materials will affect their performance, it is necessary to investigate the energy transfer process between them. Among the possible acceptors, graphene is of great interest given its unique properties, like optical absorption extending over the entire visible spectrum [95]. This may imply an effective energy transfer between an NV center and graphene. If NV center-graphene energy transfer process is well understood, a variety of promising applications could be developed. Energy transfer from a single NV center to a graphene monolayer has been experimentally demonstrated with the energy transfer efficiency reaching 40% (see Fig. 1. 11(a-b)) [96]. Similar energy transfer efficiency was observed with a single NV center in ND as an emitter using optical scanning FRET microscopy. Employing this tool made it possible to quantitatively map the near-field coupling between the NV center and a flake of graphene in three dimensions with nanoscale resolution (see Fig. 1.11 (c-d)) [97]. NV centres on graphene also exhibit strong non-radiative decay, which is usually attributed to the transfer of energy to graphene. Controlling the non-radiative transfer to graphene by electron spin resonance, which has been demonstrated, opens an avenue for incorporating NV centres into ultrafast electronic circuits and for engaging non-radiative transfer processes electronically [98].

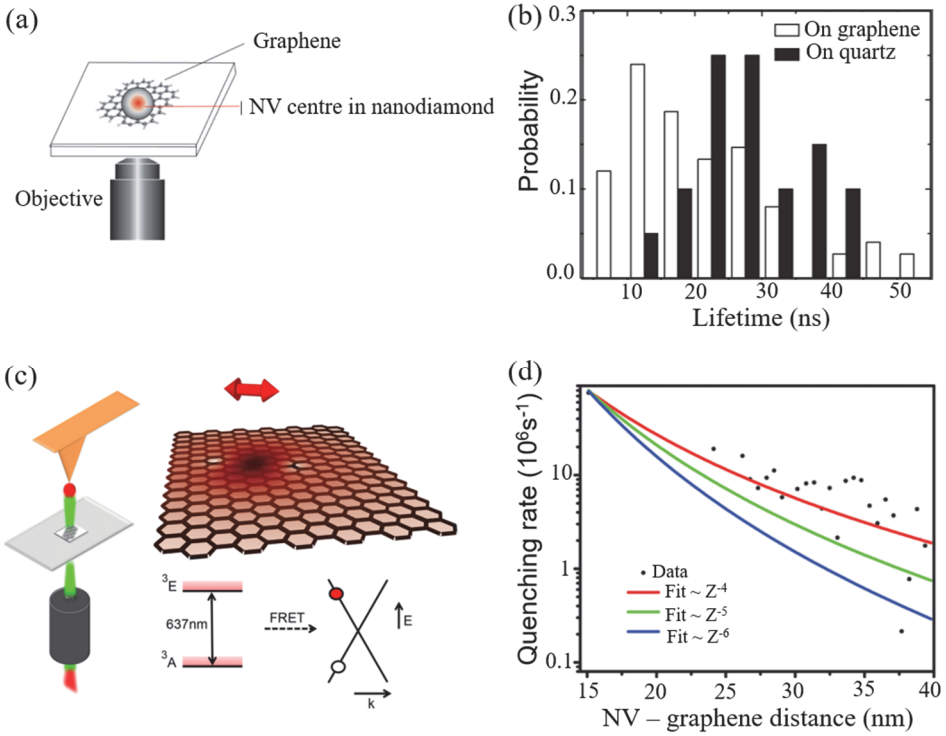

Figure 1. 11. NV centres in nanodiamond coupled to graphene. (a) A nanodiamond with an NV center on graphene substrate, figure adapted from ref. [96]. (b) Lifetime distribution of single NV centers on graphene (white bar) and on quartz (black bar) in (a). It shows that the most probable lifetime of the single NV centers on graphene is shorter than that on quartz. (c) Nanodiamonds are glued onto the apex of a Si tip. A high numerical aperture objective is used to excite a single NV in the nanodiamond and collect NV fluorescence through the graphene layer, figure adapted from [97]. (d) The excitation of the NV center's atomic dipole is converted into an exciton in graphene in (c). Upper half: Sketch of the dipole's near field. Lower half: Energy levels of the lowest optical transition relevant for energy transfer and graphene band structure near the K point. (d) Vertical dependence $\gamma_{NV}(z)$. A fit of the data (red line) agrees with the predicted z^{-4} law ($\gamma_{nr} = \gamma_r \frac{z_0^4}{z^4}$) for a Förster distance of $z_0 = 14.5 \pm 0.4$ nm.

1.6 Electron microscopy for nitrogen vacancy centres in nanodiamonds

To study NV centres in NDs one needs high spatial resolution and, thus, electron beam microscopy provides significant advantages here. No CL was observed from NV^- in all CL studies on NDs, which may be due to the charge state conversion of the centers from NV^- to NV^0 during electron irradiation. Results in [99] show that unintentional electron beam induced chemical etching can also takes place during CL analysis. A typical CL microscope consists of an SEM, or a STEM, and a light collection system which usually includes a parabolic mirror. The parabolic mirror collects the CL signal and couples it to a spectrometer, or time synchronized single photon detector (SPD) or Hanbury Brown – Twiss (HBT) intensity interferometer, to record the emission spectrum, decay trace, 2nd order correlations, respectively. The CL emission intensity from NV centres in NDs is determined by a combination of factors, such as the particle size, the density of color centers, the efficiency of

energy deposition by electrons passing through an ND, and conversion efficiency of the deposited energy into CL emission. Zhang et al. experimentally and numerically studied the relative importance of each of these factors by performing correlated AFM, PL, and CL imaging and calibrated CASINO calculations [100]. They found that the efficiency of conversion from deposited electron energy to CL emission increased rapidly with decreasing particle size down to ~ 80 nm and the CL emission decreased significantly for smaller NDs. Similarly, by acquiring well-correlated CL and secondary electron images of individual NDs in the size range 40 – 80 nm, the CL microscopy can provide spatial resolution in the region of 5 nm, outperforming fluorescence imaging [101]. Tizei et al. were able to identify H3 and NV^0 color centers through careful analysis of the CL spectra and ultrahigh-resolution CL images of multicolor centers in NDs [102, 103].

Measurements of the photon second-order correlation function, $g^{(2)}(\tau)$, are commonly used for the characterization of single photon emitters, like NV centres in diamond. These measurements are usually done with PL in a confocal microscope [104], or in some cases electroluminescence [105]. Recently, Tizei et al. have demonstrated measurements of $g^{(2)}(t)$ by CL in a STEM, which shows the possibility of measuring the quantum properties of the emitted optical beams with deep sub-wavelength resolution [106]. There, low intensity relativistic electrons beams (with energies between 60 and 100 keV) were focused in a ca. 1 nm probe to excite diamond nanoparticles and triggered light emission from single NV^0 centers. Emitted photons were gathered and sent to a HBT intensity interferometer. A dip in the correlation function at small time delays clearly identified a single photon source. In the meantime, different levels of anti-bunching can be observed for selective excitation of NV centres in the same ND by choosing excitation areas with multiple and single NV centres, as shown in Fig. 1.12 (b, c). However, CL-$g^{(2)}(t)$ measurements on multiple centres conducted with ultra-low electron beam currents show strong photon bunching, which is in stark contrast to the PL observations [107].

This can be explained by the fact that a single electron can excite multiple energetic secondary electrons, which in turn can create many optical excitations resulting in the emission of a bunch of photons within a time determined by the excited-state lifetime of the emitters. Therefore, the measurement of $g^{(2)}(t)$ can also be used to acquire the lifetimes of emitters at high spatial resolution. For instance, Martins et al. have demonstrated a significant reduction of the lifetime for NV centres in an ND hybridized with an Ag nanocube compared to NV centres in isolated NDs by measuring the $g^{(2)}(t)$ values for a large number of NDs [108]. The lifetime reduction was caused by the coupling between NV centers in NDs and surface plasmons in Ag nanocubes. Moreover, this work also emphasised the large variability of radiative lifetimes of NV centres in NDs, as shown in Fig. 1.12(a). In separate research work, the CL of NV centres in nanocomposites of ND-Ag exhibits colossal photon bunching, with modulation up to $g^{(2)}(0) > 45$, as shown in Fig. 1.12(d) [109]. Both the EELS and CL reveal optical modes excited by electrons. The probability to observe EELS signal depends on the LDOS which relates to the decay rate of the optical emitter, while the CL probability depends only on the radiative component of LDOS. The combination of EELS and CL helps to study plasmon-ND system. For example, Gur et al. used EELS to characterize DNA origami-based self-assembly of

monocrystalline Au nanoparticles and used CL to visualize light propagation supported by such a waveguide toward an ND [110]. Still in [108], the Ag nanocube plasmonic modes were characterized by EELS.

As discussed above, in all prior CL studies, no CL was observed from NV^-, therefore, the understanding of the dynamics between the NV^- and NV^0 states is important. Garcia et al. have reported conversion from NV^- to NV^0 due to electron-induced carrier generation, as shown in Fig. 1.12(e) [31]. They used ultrafast pump-probe CL spectroscopy to prepare and read out NV states with electron pulses as the pump and laser pulses as the probe. Finally, an ND-based bright sub-20nm CL nanoprobe for electron microscopy has been proposed recently in [111]. The optimization of ND composition, synthesis protocols and electron imaging conditions can produce sub-20-nm labels, which should enable high signal-to-noise localization of individual biomolecules within a cellular context [111].

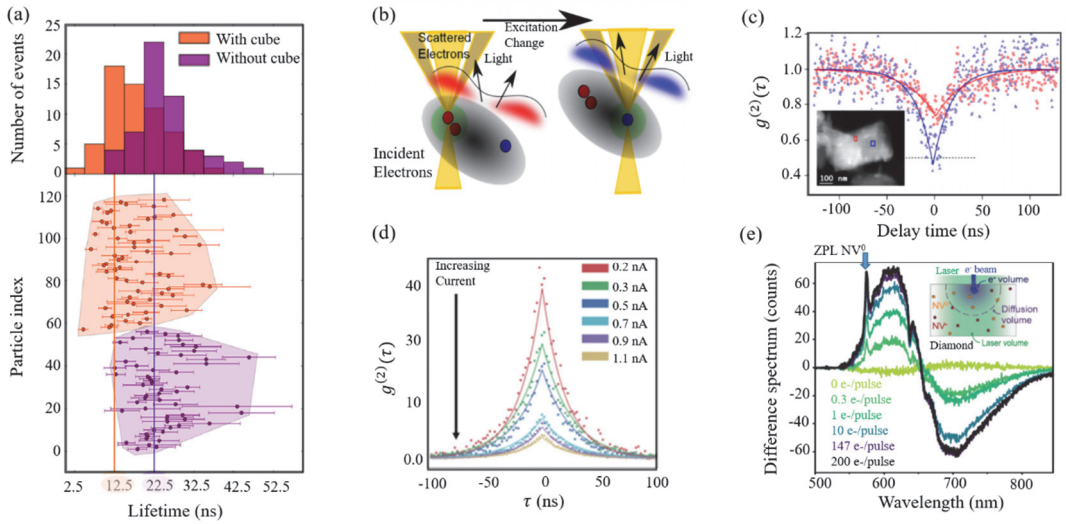

Figure 1. 12. Electron spectroscopy for NV centres in diamonds. (a) Distribution of NV centres in NDs cathodoluminescence lifetime alone (purple) and close to a silver nanocube (orange) measured on a population of 118 diamonds. The two vertical lines indicate the maxima of the NDs' lifetime distribution alone (22.5 ± 2.5 ns in purple) and close to a silver nanocube (12.5 ± 2.5 ns in orange) , figure adapted from ref. [108]. (b) An electron beam excites a volume, defined by the electron probe and diffusion of carriers (light green circle). By shifting the probe one can excite light emission from another region, with possibly corresponding different $g^{(2)}(t)$ value, figure adapted from ref. [106]. (c) $g^{(2)}(t)$ acquired with the electron beam scanning different regions (symbols represent data and lines fits), separated by 130 nm and marked by rectangles of the corresponding colors. Inset of (c), ADF image of a ND acquired in parallel, figure adapted from ref. [106]. (d) Colossal photon bunching in quasiparticle-mediated ND. Measured $g^{(2)}(t)$ (dots) with Bayesian fits (lines) for diamond-Ag nanocomposite probed using electron-beam currents of 0.2–1.1 nA, figure adapted from ref. [109]. (e) Difference spectrum, obtained by subtracting CL and PL spectra from the PP spectrum. Inset of (e) Sketch of the laser and electron excitation on the sample, representing the different volumes of primary electron interaction, diffusion of carriers, and laser volume, figure adapted from ref. [31].

1.7 Artificial intelligence for nanophotonics

Artificial intelligence (AI) now attracts significant attention from the nanophotonics community [7-10]. AI has been applied for the analysis of large datasets from NV centers in bulk diamond and made it possible to dramatically enhance the sensitivity of magnetic field measurements at room temperature [112] as well as characterizing the electron spin states [113]. Supervised machine learning algorithms have been implemented to classify single versus multiple NV centres in NDs using sparse autocorrelation data, as shown in Fig. 1.13(a) [11]. Inspired by optical magnetic detection of single-neuron action potentials using an NV centre in diamond [114], NV centres in NDs are proposed to act as a photonic sensor to study the neural activities of direct artificial neural networks enabled by nanophotonics [7].

AI can help to reveal complex relationships between the nanostructures and their optical response, such as the approximation of light scattering by multilayer nanoparticles [115]. Trained neural networks can predict the optical scattering spectrum of nanoparticles much quicker than conventional simulation methods. Moreover, a trained neural network can be used to solve nanophotonic inverse design problems by using back propagation with the analytical gradient. Recently, an optical information storage concept based on training an artificial neural network on large amounts of experimentally measured optical scattering spectra from silicon nanostructures has been proposed [116]. As shown in Fig. 1.13(c), the silicon nanostructures were designed to have a unique scattering spectrum in order to encoded digital information with a specific bit-sequence. An artificial neural network was employed to interpret visible light scattering, where it played a key role in achieving high accuracy of reading distorted data (see Fig. 1.13(d)).

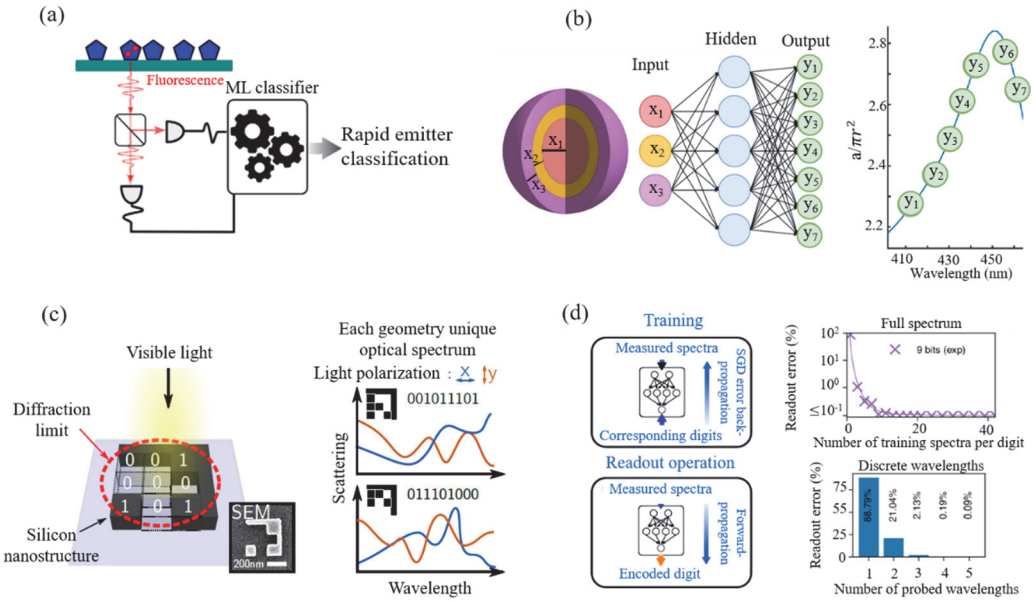

Figure 1. 13. AI applied in nanophotonics. (a) Machine learning assisted rapid single photon emitter detection. The trained model classifies the previously unencountered emission sources as “single” and “not-single” emitters based on the sparse autocorrelation data [11]. (b) The neural network architecture has as its inputs the thickness of each shell of the nanoparticle, and as its output the scattering cross-section at different wavelengths of the scattering spectrum [115]. (c-d) The artificial neural network used to decode information from optical information storage via a spectral scattering analysis from sub-diffraction small nanostructures. (c) Each bit sequence is encoded by a specific geometry which is designed such that it possesses a unique scattering spectrum. (d) A neural network is trained on a large number of spectra such that it learns to decode noisy spectra of formerly not seen structures. Even if only a few wavelengths are probed, the readout accuracy of the network is excellent [116].

Thesis Overview

This thesis investigates the emission properties of nitrogen-vacancy (NV) centres in nanodiamond (ND) which have been charecterized by time-resolved cathodoluminescence. Control of the emission properties of NV centres in ND has been achieved through tailoring the dielectric properties of the host medium. The underlying mechanisms linking dielectric properties, geometry and emission statistics have been analyzed. Machine learning has be employed to derive the cathodoluminescence from plasmonic geometry and vice versa. Its structure is as follows:

- Chapter 1 introduced the cathodoluminescence of plasmonic system, the research progress of artificial intellegence for nanophotonics and the research progress of NV centres in ND for nanophotonics. Including NV centres photonic properties, controlling emission properties of NV centres in ND, NV centres in ND studied by electron beam microscopy.

- Chapter 2 focuses on the experimental and simulation methods. including sample fabrication, nanodiamond characterization (time-resolved cathodoluminescence system), modelling of NV centre emission properties, modelling of CL from plasmonic system and neural network description .

- Chapter 3 presents the experimental demonstration of decay rate enhancement of diamond NV centres on diamond film, in which the NV centres have been characterized by time-resolved cathodoluminescence. Control of NV centre decay rates by changing diamond film thickness has been studied. Moreover, lifetime distributions and spectra characteristics of NV centres in ND have been analyzed.

- Chapter 4 demonstrates the engineering the collapse of lifetime distribution of NV centres in ND, in which the NV centres have been characterized by time-resolved cathodoluminescence. The distribution of the decay rates of NV centers in nanodiamonds can be made narrower by as much as five times once the nanodiamonds have been embedded into chalcogenide films.

- The chapters 3 & chapter 4 of the thesis deal with the problem of controlling CL by changing the environment of the emitter. The chapter 5 in a sense deals with the inverse problem: Can I obtain information about the emitter and its environment (i.e. configuration of apertures) from CL? Chapter 5 demonstrates identifying nanoscale objects through luminescence and artificial intelligence. Cathodoluminescence spectra emitted by sets of subwavelength plasmonic apertures can be predicted from their configurations and, inversely, information about the configurations of subwavelength plasmonic apertures can be inferred from the cathodoluminescence spectra they emit.

- Chapter 6 presents a summary together with general conclusions and discusses future work.

Chapter 2

Experimental and simulation methods

In this chapter, I describe the main methods employed to obtain the results presented in this thesis, from sample fabrication and numerical modelling, to sample characterization. Firstly, I introduce the thin film deposition techniques, which include plasmonic and chalcogenide materials. The compositional space of binary alloy chalcogenides can be rapidly and systematically explored through the synthesis of compositional gradient thin films using combinatorial evaporative physical vapor deposition. Moreover, this chapter introduces the home-built time-resolved cathodoluminescence system with which the majority of the experimental results are obtained. Simulations are based on the finite element method and include modelling of NV centre emission properties in different dielectric environments, modelling of the cathodoluminescence (CL) of plasmonic apertures and metasurfaces. Finally, I describe the machine learning approach employed in the analysis of the CL spectra of plasmonic systems.

2.1 Sample fabrication & characterization

My work considers a range of sample geometries, such as thin dielectric and plasmonic films, plasmonic apertures and met surfaces. To this end, sample fabrication included thin films deposition (silver, gold, chalcogenide, and diamond), fabrication of nanostructures (metasurface, plasmonic apertures), and nanodiamond deposition.

2.1.1 Thin film deposition

In the following, I describe the deposition methods of thin films of different materials:

- **Plasmonic metals.** I deposited silver (Ag), gold (Au), nanofilms on silicon substrate by thermal resistance evaporation (Auto 306 Resistance Evaporation) which heats and evaporates metal by the Joule heat generated by a large electric current passing through the evaporation source. The thickness of the deposited thin films was measured by a stylus profilometer (P-16+ Stylus Surface Profiler) along the external edges of the film. The thickness of the thin films was typically several hundred nanometers (100-300 nm).

- **Diamond film.** The diamond thin film was grown on silicon substrate by plasma-enhanced chemical vapor deposition (OPT Plasmalab System 100 PECVD), in which the plasma has strong chemical activity and is easy to react, depositing the diamond film on the substrate. The thickness of the deposited diamond film was measured by a scanning electron microscope (Helios Nanolab-600 DualBeam FIB/SEM) along the cut edges (cut by the focused ion-beam) of the film. The thickness of the thin films was typically ~ 200 nm.

Deposition and thickness measurement of the diamond film was performed by my colleague Dr Artemios Karvounis.

- **Chalcogenides**. Chalcogenide semiconductor alloys offer a uniquely broad pallet of optical properties which can be controlled by stoichiometric design, complementary to the existing material platforms which are noble metals with the shortcomings of Joule losses, cost and passive character. The binary variants of antimony telluride (SbTe) were selected as an archetypical chalcogenide [117]. Deposition of chalcogenides was performed by my colleague Dr Davide Piccinotti. A thin film of SbTe with varying composition and ranging in thickness from 20 to 50 nm was deposited over a 28 mm × 28 mm area of a silicon (Si) substrate (thickness: 40 – 100 nm) using a high-throughput physical vapour deposition system [118]. The system was equipped with off-axis Knudsen cell (a Knudsen cell is an effusion evaporator source for relatively low partial pressure elementary sources, which make it is easy to control the temperature of the evaporating material) sources symmetrically arranged around the target substrate, which was held under $\leq 10^{-8}$ mbar vacuum at room temperature. The density gradient of Sb and Te (each of ≥ 99.9999 % purity) along the substrate was independently controlled using fixed wedge shutters, which ensured that for every SbTe composition (i.e., at every point on the substrate) the atomic components mix simultaneously. During the synthesis process, the phases of these alloys were formed directly as amorphous [119]. Samples were vacuum sealed immediately upon production and between characterization measurements. Figure 2.1 shows the image of a characteristic SbTe film on silicon.

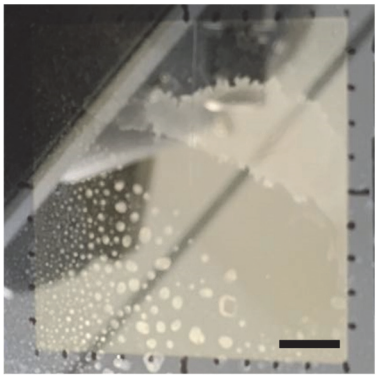

Figure 2.1. Image of a characteristic SbTe sample with gradient composition and NDs deposited from solution on its surface. SbTe films are deposited over an area 28 mm × 28 mm (highly reflective area) on Si substrate with dimensions of 35 mm × 35 mm. The texture of the film surface is due to the deposited NDs. The scale bar is 5.5 mm. Sample fabricated by Dr Davide Piccinotti.

2.1.2 Focused-ion beam milling

Patterning of plasmonic films in the form of metasurfaces or arrangements of apertures was performed by Focused-ion beam (FIB) milling by my colleagues Dr Jun-Yu Ou and Dr Oleksandr Buchnev. FIB milling uses highly focused ion beams such as Ga^+ beam to scan and cut the thin film surface inside a vacuum chamber. The FIB can directly "mill" the sample

surface, through the sputtering process which can be controlled with nanometer precision. It is possible to perform very precise nano-machining to produce minute components or to remove unwanted material by carefully controlling the energy and intensity of the ion beam. A FIB becomes even more powerful when it is combined with a SEM. In a DualBeam system, the electron and ion beams intersect at a coincident point near the sample surface, allowing immediate, high-resolution SEM imaging of the FIB-milled surface. Such systems combine the benefits of both the SEM and FIB and provide complementary imaging capabilities. We employed the Commercial Dual Beam^{TM} FIB-SEM system (Helios Nanolab-600 DualBeam FIB/SEM) from FEI Ltd.

2.1.3 Nanodiamond deposition

In my experiments, I employed commercially available water solutions of NDs (obtained from Sigma Aldrich) with sizes of ~120 nm and each containing a large number of NV centers (~1200). Two methods were considered for the deposition of NDs on the substrate. The first involves spraying NDs solution by an air brush (Harder & Steenbeck Evolution X). The NDs solution was sprayed out by the compressed N_2 as shown in Fig. 2.2(a). The control of spraying time is important to achieve fully cover the substrate (see Fig. 2.2(b-d)). Therefore, one advantage of this method is the difficulty in controlling of the spraying time and the N_2 pressure. The other disadvantage is that the flux output from the air brush is large, which waste some NDs solution. The second approach involved drop casting NDs from the solution directly on the substrate. Here, the choice of solvent is important. For instance, in the case of water solution the contact angle between water and Si or glass substrate is too high (44^0 on Si substrate [120]), which does not allow the solvent to spread rapidly resulting in the formation of large ND clusters (see Fig. 2.3(a)). The second approach was employed to deposit NDs in all works reported in this thesis.

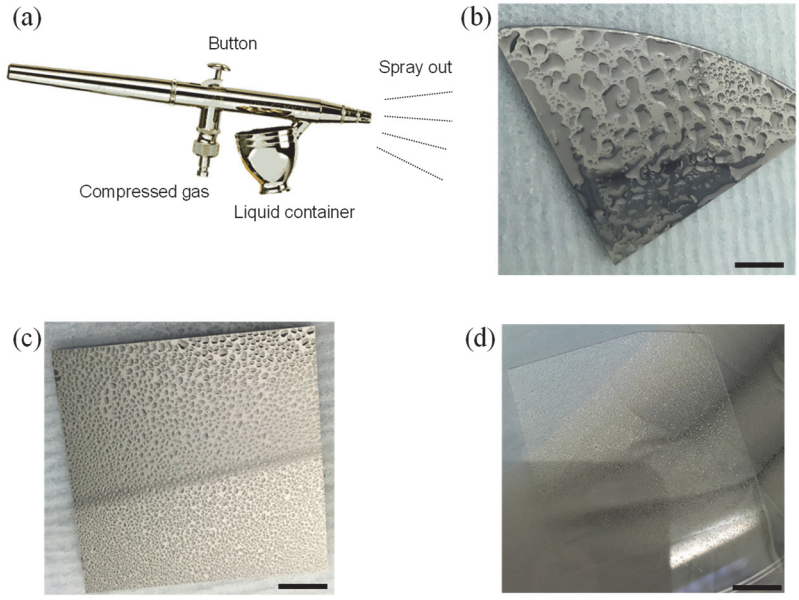

Figure 2.2. Spray coating NDs. (a) The construction of the air brush. (b-c) Spray coated NDs on a Si substrate with spray time 4s (b) and 1s (c). (d) Spray coated NDs on a glass substrate with spray time 1s. Scale bar is 4 mm in (b) and 6 mm in (c-d).

To achieve a more homogeneous distribution of NDs over the substrate and avoid the formation of very large aggregates, the NDs should be diluted in solution with a smaller contact angle with substrates, such as methanol (22^0 on Si substrate [120]). To this end, the NDs were diluted in methanol (~0.02mg/mL) and mixed for 10 min in an ultrasonic vibrator. Then they were dispersed onto the substrate by a micropipette as shown in Fig. 2.3 (b). The methanol solution spreads quickly resulting in the NDs being sparsely distributed on the Si substrate after the methanol was evaporated as shown in Fig. 2.3(c).

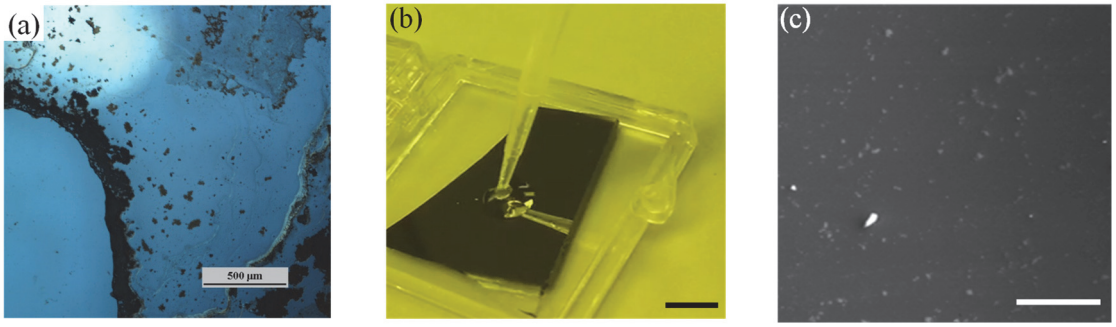

Figure 2.3. Examples of NDs drop casting on substrates. (a) Drop casting NDs from water solution to a glass substrate. The black areas represent large ND aggregates. The scale bar is 500 μm. (b) NDs diluted in methanol transferred by micropipette to a Si substrate. Scale bar is 5 mm. (c) Distribution of ND clusters on Si substrate. The scale bar is 50 μm.

2.1.4 Spectroscopic ellipsometry

Spectroscopic ellipsometry is a useful technique used for characterizing the optical properties of thin films. It is applicable to many different types of materials and can be used to determine the complex dielectric constants of thin films. Fig. 2.4 shows the principle of ellipsometry, a light source linearly polarized by a polarizer then incident onto the sample. The reflected light is circularly polarised and the degree of polarisation is measured by the detector, with the help of an analyzer. The axes denoted with *p* and *s* in Fig. 2.4 represent the perpendicular and parallel polarization planes, respectively.

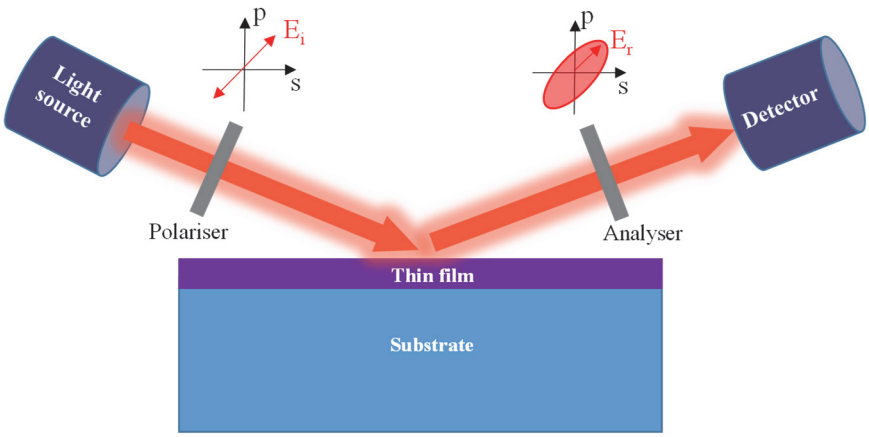

Figure 2.4. The principle of spectroscopic ellipsometry. The sample of unknown complex permittivity is illuminated by linearly polarized light. The light changes polarization as it interacts with the sample. The reflected light is circularly polarised and the degree of polarisation is measured by the detector, with the use of an analyser. The axes denoted with p and s represent the perpendicular and parallel polarization planes, respectively. The incident p-waves and s-waves usually have a phase difference that depends on the sample properties. E_i and E_r represent the incident and reflected electric field, respectively. The parameters obtained in ellipsometry measurements are usually denoted Δ and Ψ, which describe the change in polarization that occurs when the measurement beam interacts with a sample surface.

The incident light beam contains electric fields both parallel (p) and perpendicular (s) to the plane of incidence. The surface differentiates between the p- and s-polarized light, causing a change in the outgoing polarization. This is represented by both an amplitude ratio (tan(Ψ)) and phase difference (Δ), which are related by [121]:

$$tan\,\Psi e^{i\Delta} = \frac{R_p}{R_S}, \tag{2.1}$$

Where R_p and R_s are reflection coefficients for the p waves and s waves. After multiple measurements are made at a different angle of incidence, the 'pseudo' optical constant can be calculated from the equation:

$$\langle\tilde{\varepsilon}\rangle = sin^2\theta_i[1 + tan^2\theta_i(\frac{1-\rho}{1+\rho})^2], \tag{2.2}$$

Where θ_i is the angle of incident light and ρ is the complex reflectance ratio given by $\rho = tan(\Psi)e^{i\Delta} = \frac{R_p}{R_S}$. Usually, a dispersion model that describes the dielectric constant is used to fit the data. In my work, the Lorentz oscillator model is used to fit the ellipsometry data from the SbTe film, due to the measured spectral dispersion of SbTe's relative permittivity is reproduced very well by a single Lorentzian oscillator absorption model as demonstrated in [122]. The Lorentz model is a theory based on the classical theory of interaction between light and matter, used to describe frequency dependent polarization due to bound charges. The main assumption of the Lorentz model is that an atom with electrons bound to the nucleus behaves very similarly to a small mass bound to a large mass via a spring [123]. The dielectric function in the Lorentz

model can be expressed as:

$$\varepsilon = \varepsilon_\infty + \frac{A\omega_0^2}{(\omega_0^2-\omega^2)-i\Gamma\omega}, \tag{2.3}$$

Where ε_∞ takes into account the contribution of high energy transitions, ω_0 is the resonant frequency of the oscillator, Γ is the damping factor, A represents the oscillator strength. ε is a complex quantity and it can be separated into its real and imaginary parts:

$$\varepsilon = \varepsilon_1 + i\varepsilon_2 = \varepsilon_\infty + \frac{A\omega_0^2(\omega_0^2-\omega^2)}{(\omega_0^2-\omega^2)^2+(\Gamma\omega)^2} + i\frac{A\Gamma\omega_0^2\omega}{(\omega_0^2-\omega^2)^2+(\Gamma\omega)^2}, \tag{2.4}$$

In the ellipsometry measurements of Chapter 4, I used a J.A. Woolam M-2000 spectroscopic ellipsometer to measure the induced polarisation change in the SbTe thin films for incident angles of 65°, 70°and 75°. Then I used the CompleteEase (J.A. Woolam) software to do the data analysis and dispersion model fitting. The root mean squared error can be calculated by the following equation:

$$\mathrm{MSE} = \sqrt{\frac{1}{3n-m}\sum_{i=1}^{n}\left[\left(K_{Exp_i} - K_{Mod_i}\right)^2 + \left(L_{Exp_i} - L_{Mod_i}\right)^2 + \left(M_{Exp_i} - M_{Mod_i}\right)^2\right]}, \tag{2.5}$$

Where m is the number of fitting parameters, n is the number of wavelengths, the subscripts Exp and Mod represent the experimental and modelled data, respectively. The parameters K, L and M are given by:

$$K = \mathrm{Cos}(2\Psi), \tag{2.6}$$

$$L = \mathrm{Sin}(2\Psi)\mathrm{Cos}(\Delta), \tag{2.7}$$

$$M = \mathrm{Sin}(2\Psi)\mathrm{Sin}(\Delta). \tag{2.8}$$

2.2 Time-resolved cathodoluminescence

The time-resolved luminescence spectroscopy can be used to monitor molecular interactions and motions that occur in the picosecond - nanosecond time range, which makes it is useful in the analysis of biomolecular structure and dynamics [124]. It is also a powerful analysis tool in investigating the temporal evolution of fluorescence from nano-materials [125]. Its time-domain implementation requires recording the time-dependent intensity profile of the emitted light upon excitation by a short pulse with high energy. Two different techniques are typically employed for the measurement of light emission lifetimes: phase-resolved [126] and time-resolved fluorometry [124]. The phase-resolved method measures the phase shift of the luminescence signal relative to a modulated CW excitation signal that allows extracting the lifetime of the excited state, while the time-resolved techniques record the emission intensity in response to excitation by a narrow optical or electron pulse, which provides more kinetic information than phase techniques.

An important challenge involves the rapid decay of the excited emitter, typically in the range of 100 ps – 10 ns. The solution to this problem is provided by time-resolved fluorometry, which can be further subdivided into analogue and digital (photon counting) techniques. Time-

correlated single-photon counting (TCSPC) is one of the photon counting techniques (digital), which was employed for the measurement of picosecond to microsecond lifetimes together with high repetition rate light sources. TCSPC technique provides a wide dynamic range, from picosecond to microsecond, and has become the method of choice for those working with high repetition rate excitation sources (>10kHz), weak fluorophores and short lifetimes. The lifetimes of NV centres in NDs are in the nanosecond scale [34, 35], which are suitable to be studied in this technique. In the following, I present the implementation of TCSPC in the context of time-resolved cathodoluminescence.

2.2.1 Time-correlated single photon counting

TCSPC is based on the principle that the probability distribution of detecting a photon at time *t* after the excitation pulse is proportional to the fluorescence intensity at that time [127]. The fundamental experimental configuration is summarized in Fig. 2.5. A synchronized electronic 'Start' signal is sent to TAC for triggering, at the same time, a light or electron pulse excites the sample which emits photons are detected by the detector, the detector sends a 'Stop' signal (this signal can be delayed) to the TAC to finish a counting circle. The arrival of each emitted photon is timed with reference to the excitation event by a Time-to-Amplitude Converter (TAC). The TAC produces time-to-pulse height conversion (TPHC) signal which proportional to the elapsed time between 'Start' and 'Stop' timing signals. An Analog-to-Digital Converter (ADC) then digitizes this TPHC constructs a histogram of photon time distribution equivalent to the actual radiative decay. This histogram typically contains many thousands of photons.

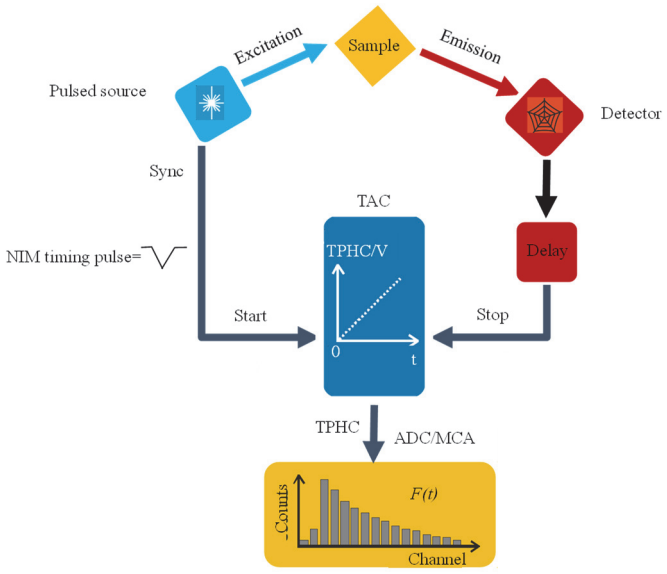

Figure 2.5. Time-correlated single-photon counting (TCSPC) schematic (Forward Time-to-Amplitude Converter (TAC) mode). A synchronized electronic 'Start' signal sent to TAC for triggering, at the same time, a light or electron pulse excites the sample which emits photons are detected by the detector, the detector sends a 'Stop' signal (this signal can be delayed) to the TAC to finish a counting circle. The arrival of each emitted photon is timed with reference to the excitation event by a Time-to-Amplitude Converter (TAC). The TAC produces time-to-pulse height conversion (TPHC) signal which proportional to the elapsed time between 'Start' and 'Stop' timing signals. An ADC then digitizes this TPHC constructs a histogram of photon time distribution equivalent to the actual fluorescence decay. Figure adapted from ref. [128].

During the operation, the TAC timing cycle is initiated by a 'Start' signal generated by the excitation electronics (such as a wave function generator). If no emitted photons are detected within the TAC range, then the TAC simply resets and awaits the next 'Start' signal. If a photon is detected a 'Stop' signal is presented within the TAC range, the TAC converts the time interval between 'Start' and 'Stop' timing inputs to a proportional analogue voltage (TPHC). Only one conversion can occur per cycle so if more than one photons are detected during the same cycle, all will be disregarded except the first one. This is a fundamental TAC limitation and applies to all TCSPC instrumentation. If enough 'late' photons are disregarded, then distortion of the perceived decay will occur and the recovered lifetime will be shorter than the true value, which is called the 'pile-up' effect [129]. The 'pile-up' effect can be minimized by reducing the probability that more than one photon will be detected within the TAC range in response to any excitation event. The throughput of a TCSPC instrument described by the parameter α, the Stop-to-Start ratio, and defined as [128]:

$$\alpha = \frac{R_p}{R_t} \times 100\%, \tag{2.9}$$

in which R_t and R_p are the 'Start' and 'Stop' rates respectively. It is widely accepted that simply limiting α to around 2% can make the 'pile-up' effect negligible [128]. During the measurement of weakly emitting samples, a Stop-to-Start ratio of 2% is usually difficult to achieve and pile-

up is negligible. However, reducing the excitation intensity is usually necessary with stronger εμιττινγ samples, in particular, at low repetition rates, therefore, the data collection rate is limited not by the sensitivity of the instruments, but also by the pile-up effect itself [128].

2.2.2 Time resolved cathodoluminescence

In the TR-CL technique, the emitter under study is excited by an electron pulse, which can be generated by blanking the electron beam e.g. in a scanning electron microscope (SEM) [130]. The beam blanking system can be realized by a plate capacitor based on electrostatic blanking. Beam blanking is activated by the external trigger signal. When a voltage difference is applied to the capacitor plates, the electron beam is blanked. If the voltage is decreasing, there is only an angular change of the electron beam. The electron beam is transmitted if the voltage is totally removed. Therefore, pulses of electrons are generated by sweeping the electron beam across the aperture (see Fig. 2.6).

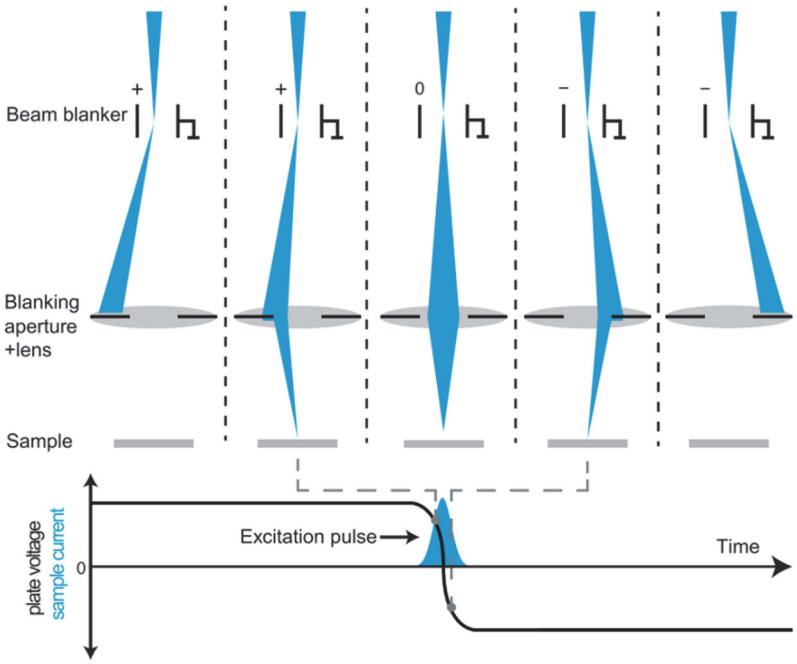

Figure 2.6. Schematic of the process of electron pulses created by beam blanking. At t = 0, the electron beam is angularly deflected and fully blanked by an aperture at the location of the electron lens. Reversing the voltage across the blanker plates scans the electron beam over the aperture. Figure adapted from ref. [131].

Figure 2.7 illustrates the dynamic process of CL signal generation by pulsed electron beam excitation [132]. The rise time of the electron pulse usually does not affect the CL lifetime measurements, while the fall time of the electron pulse has to be shorter than the CL lifetime of the sample. In fact, the fall time controls the time resolution of the TR-CL system.

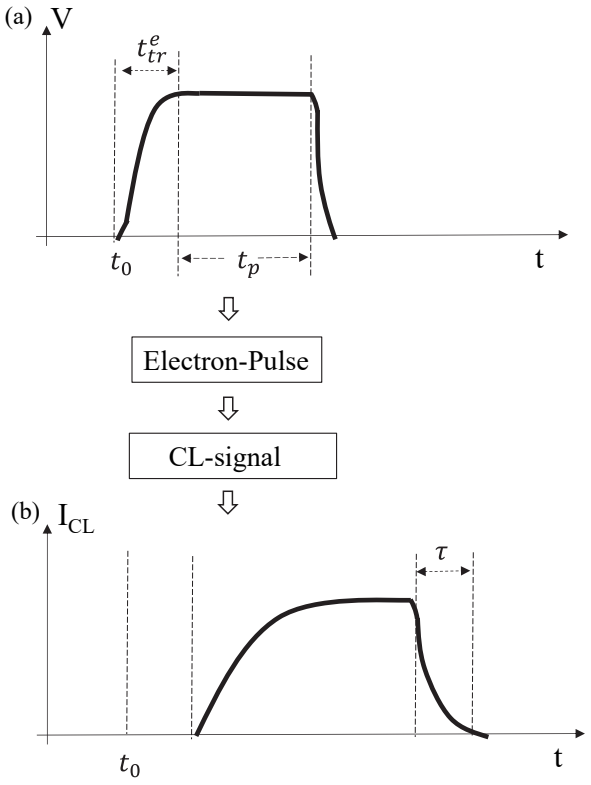

Figure 2.7. Pulsed electron beam excited CL signal. (a) The waveform output from the wave function generator. t_r^e is electron transit time, t_p is electron pulse width. (b) Pulsed electron beam CL signal intensity in time domain. τ is emitter lifetime. Figure adapted from ref. [132].

2.2.3 Implementation of scanning electron microscope based time resolved cathodoluminescence system

The home-built TR-CL system is based on a modified SEM; these modifications not only include a highly efficient CL collection system which has been introduced in chapter 1, section 1.2, but also a time synchronized fast single photon detection system and a beam blanking system. My contribution is to synchronize all modules to in order to implementthe principle of TCSPC and characterize the system's performance. I was also involved in the beam blanker installation. Figure 2.8 shows the instrumentation of the SEM based TR-CL system. In the time synchronization part of the system, the waveform generator (ROHDE & SCHWARZ AM300 dual-channel Arbitrary / Function Generator) sends the trigged signal to drive the beam blanker and simultaneously a synchronized pulse to a pulse converter (IBH Model TB-01), which in turn sends a signal to the single photon detector controller (Horiba FluoroHub). The parabolic mirror collects and collimates emitted light directly to the input slit of the grating-based spectrometer (Horiba iHR320 imaging spectrometer) with an internal grating that allows selecting the versatile wavelength range to the output slit. Photons were detected by a picosecond photon detection module (Horiba TBX). In the beam blanking system, we have measured the beam blanker capacitance at ~14pF corresponding to the charging and discharging time scale of ~700 ps with 50 Ohm input impedance. There are two capacitor plates in the beam blanker that allow deflect the electron beam, one grounded and one at high voltage. The pulse generator connected to the beam blanker circuit generates a 0-11V pulse with variable

frequency and pulse width, which can be set by the external input from the WFG. The electron beam pulse is created by the beam blanker which is controlled by the WFG. The time synchronization is achieved by the WFG and single photon detector controller.

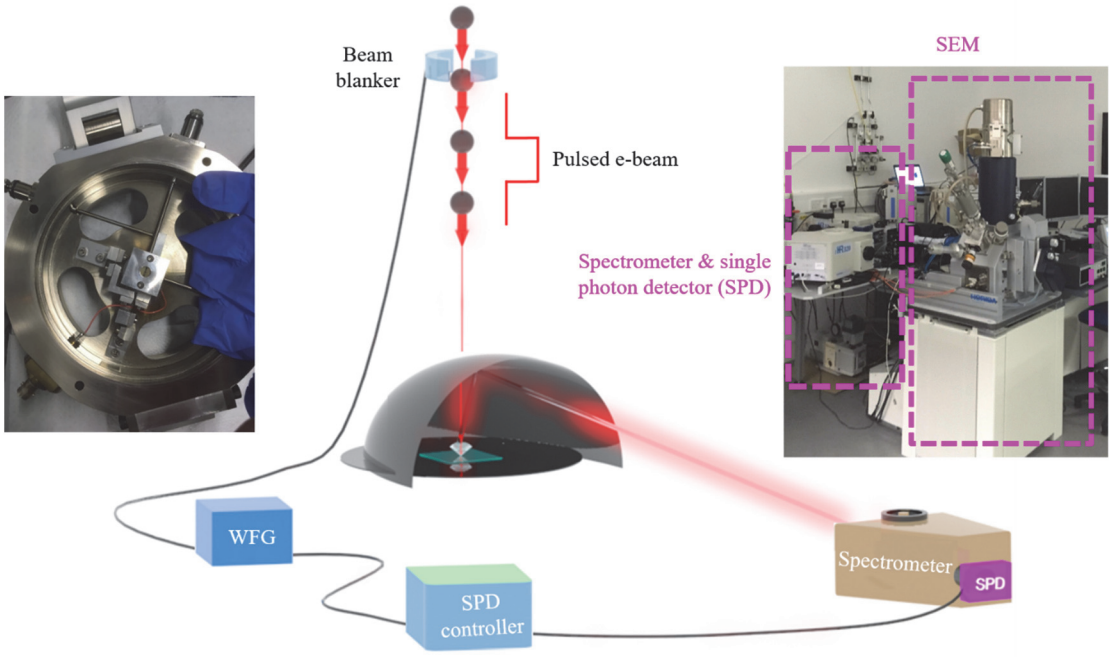

Fig. 2.8. Instrumentation of SEM based TR-CL system. The pulsed e-beam is created by abeam blanker which is controlled by a wave function generator. The emitted photons are collected by a parabolic mirror, while CL spectra are recorded by a vis/IR spectrometer. An internal filter wheel in the spectrometer allows selecting photons within a prescribed bandwidth, which are then directed to the single photon detector entrance. Time synchronization is achieved by the single photon controller and a wave function generator. The left inset presents the beam blanker; the right inset shows the TR-CL system in our lab. WFG: wave function generator, SPD: single photon detector.

2.2.4 The time resolution of the time resolved cathodoluminescence system

The time resolution is a key parameter to evaluate the performance of the TR-CL system. Figure 2.9 illustrates the diagram of the electronic pulse signal generated from the WFG through the pulse generator to the capacitor. Several factors influence this process: 1) the rise times of the signal generated by the WFG and the pulse generator; 2) the response time (charging and discharging) of the capacitor in the beam blanker; 3) the SPD module gate time (transition time in the CCD). One way to quantify the response time of the system is to measure the decay time of emitters with a lifetime much shorter than the system response time. The lifetime of transition radiation from the gold surface is in the femtosecond scale [133], which is suitable to measure the time resolution of TR-CL system that is expected in the ns range.

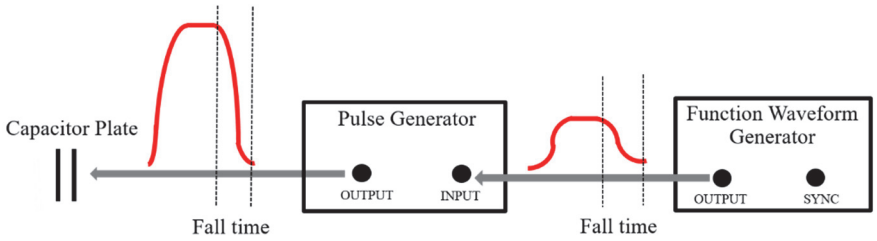

Fig. 2.9. Rise and fall time of the voltage pulse driving the beam blanker. An electronic pulse signal created by the waveform function generator triggers the pulse generator which outputs a 10 V pulse and drives the capacitor of the beam blanker.

Here, we characterized the electron beam pulse in our TRCL system by measuring the lifetime of transition radiation from the gold film on Si_3N_4 membrane following ref. [134]. The full width at half maximum (FWHM) is ~ 6 ns as shown in figure 2.10. This means our TR-CL system time resolution is ~ 3 ns. The transition radiation is relatively weak at 10kV, so we compensate with a high electron beam current at 15 nA. The emitters we consider in our work are the NV centres in diamond whose lifetimes are >10 ns (for the cases studied). Therefore, our TR-CL system is adequate to study the dynamic emission properties of NV centres.

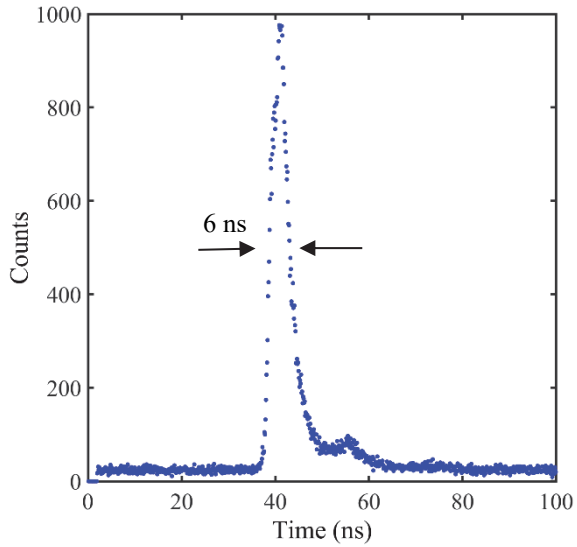

Fig. 2.10. Pulse width characterization at 10kV. The time histogram was binned at 109 ps (minimum interval time between the arrival of two photons). The pulse full width at half maximum (FWHM) is shown (6ns). Emissions are the transition radiations from the gold film on Si_3N_4 membrane. The second peak at ~50 ns is due to the jitter of the wave function generator.

2.3 Cathodoluminescence of nitrogen vacancy zero centres in nanodiamonds

Our samples contain a high concentration of NDs, which leads to the formation of large aggregates on the substrate surface (see the top right inset in Fig. 2.11). Only isolated ND clusters are selected for the CL measurement. Figure 2.11 shows the CL spectrum of NV centres in an isolated ND cluster with a size of about 2 μm under the excitation of a 10 kV energy and 1.9 nA current electron beam. There is a clear NV^0 centre ZPL line at a wavelength of 575 nm

(see top left inset in Fig. 2.11), while the NV^- centre ZPL line does not appear in the CL spectrum (see section 1.5). In this thesis, all the NV centre spectra are measured in CL, thus only NV^0 centres are considered. Due to the CL measurement being performed at room temperature, there is a broad phonon sideband with a peak wavelength at around 680 nm. By performing CL mapping for this NDs cluster at a wavelength of 575 nm, we observe a strong spatial variation of intensity (see bottom right inset in Fig. 2.11), which indicates a non-uniform distribution of NV^0 centres and/or non-uniform excitation.

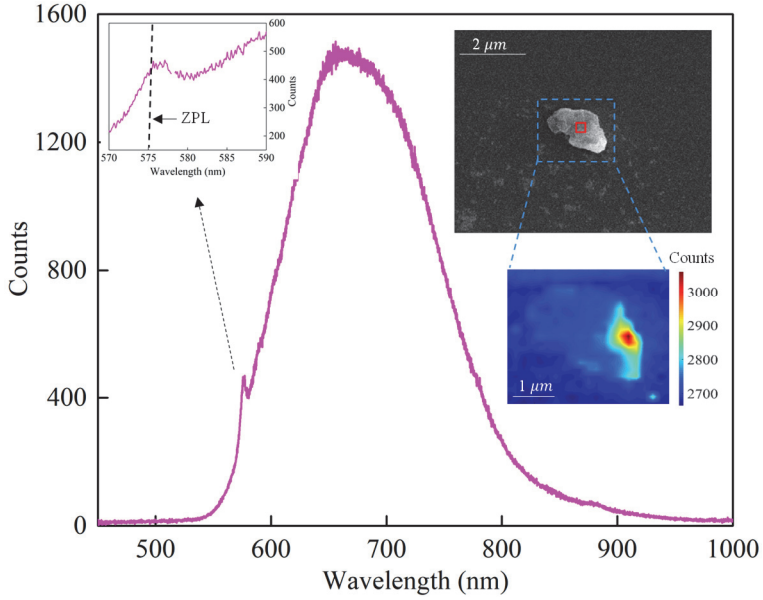

Fig. 2.11. CL spectrum of NV centres in a ND cluster. Top left inset: zoom-in of the CL spectrum of NV^0 centre around the zero phonon line; Top right inset: SEM image of the ND cluster, the spectrum taken at the position as the red box marked. Bottom right inset: inset of CL map of the ND cluster at a wavelength of 575nm.

2.3.1 Nitrogen vacancy zero centres cathodoluminescence spectrum fitting

In order to separately analyze the spectrum properties of ZPL and PSB, I performed CL spectrum fitting for these two peaks. Firstly, the spectra were transferred to the frequency domain and fit the PSB with the following formula:

$$I(\omega) = A_1 e^{-\frac{(\omega - B_1)^2}{C_{1/2}}} + D + E\omega, \tag{2.10}$$

In this formula, there are three parts, $A_1 e^{-\frac{(\omega - B_1)^2}{C_{1/2}}}$ is a Gaussian model for the PSB peak, $E\omega + D$ is the linear part for the background. We can know that A_1, B_1, C_1 stands for the amplitude, centre frequency and full width of half maximum (FWHM) or linewidth of the PSB. Figure 2.12 (a) shows the fitting graph matched well with the raw data (the normalized RMSE is ~2%). The second step is to remove the slope of the ZPL peak. The slope was firstly fit with a linear function then subtracted by the partial raw data contains the ZPL part (see Fig. 2.12(b)). Finally, the ZPL peak with removed slope was fit with a Gaussian model:

$$I(\omega) = A_2 e^{-\frac{(\omega - B_2)^2}{C_{2/2}}}, \tag{2.11}$$

Similarly, A_2, B_2, C_2 stand for the amplitude, centre frequency and FWHM of the ZPL peak of NV^0 centres, respectively. Figure 2. 13 (c) shows the fitted matching well with the raw data (the normalized RMSE is ~3%).

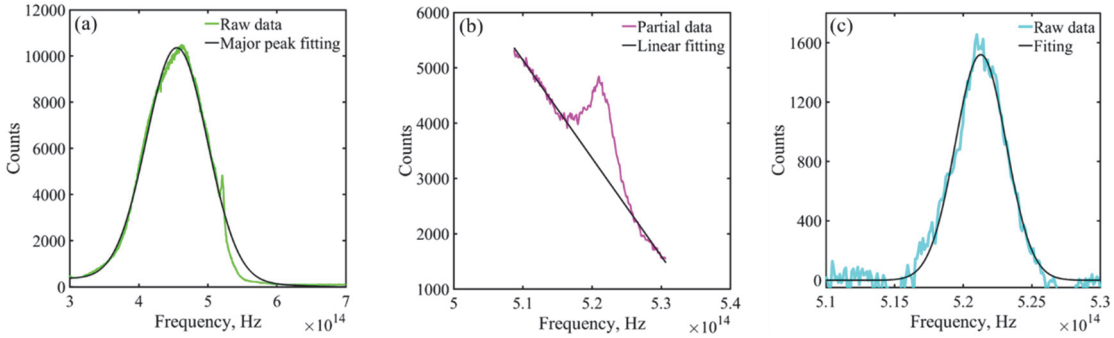

Fig. 2.12. CL spectrum fitting. (a) Phonon sideband fitting. Experimental data (green line), spectrum fitting (black line). (b) Removal of the linear trend at the ZPL Experimental data (purple line), slope fitting (black line). (c) Zero phonon line fitting. Experimental data (aqua line), spectrum fitting (black line).

2.3.2 Intra-cluster variation of nitrogen vacancy zero centres spectra

I quantified the variation of the CL response within a single ND cluster by CL mapping (see Fig. 2.13). The CL spectra in each pixel were fitted by the method presented above. Figures 2. 13(b-g) show the spatial variation of all the fitted parameters. The spatial maps of parameters A_1 and A_2 corresponding to the peak values of PSBs and ZPLs are seen in Fig. 2. 13(b-c). There are relatively high values of A_1 and A_2 in the NDs clusters, the variations of PSBs and ZPLs peaks are both as high as 10 times (see Fig. 2.13(h)), which is due to the high concentrations of NV centres in NDs clusters. Similar variations of PSBs and ZPLs peaks mean the concentration of NV centres contributes simultaneously to the PSBs and ZPLs. The maps of parameters B_1 and B_2 present the spatial variation of the centre frequencies of PSBs and ZPLs as seen Fig. 2. 13(d-e), the values are homogeneously distributed in these two with variations less than 2% (see Fig. 2.13(i)). The maps of parameters C_1 and C_2 present the FWHMs of PSBs and ZPLs as shown in Fig. 2. 13(f-g). The FWHMs of PSBs do not change much as well (16%), as shown in Fig. 2. 14(j). However, there is a large variation for the FWHMs of ZPLs, the reason is that PSB depends on temperature which is always constant in the lab while the ZPLs related to the strain effect of the cluster [102]. Fig. 2.14(a-b) show the normlized RMSE of the fittings of major peak and second peak, in which there is higher normalized RMSE in the area with less density of NDs due to the noise levels are relatively high. However, in the area of NDs the normalized RMSE is always less than 10%.

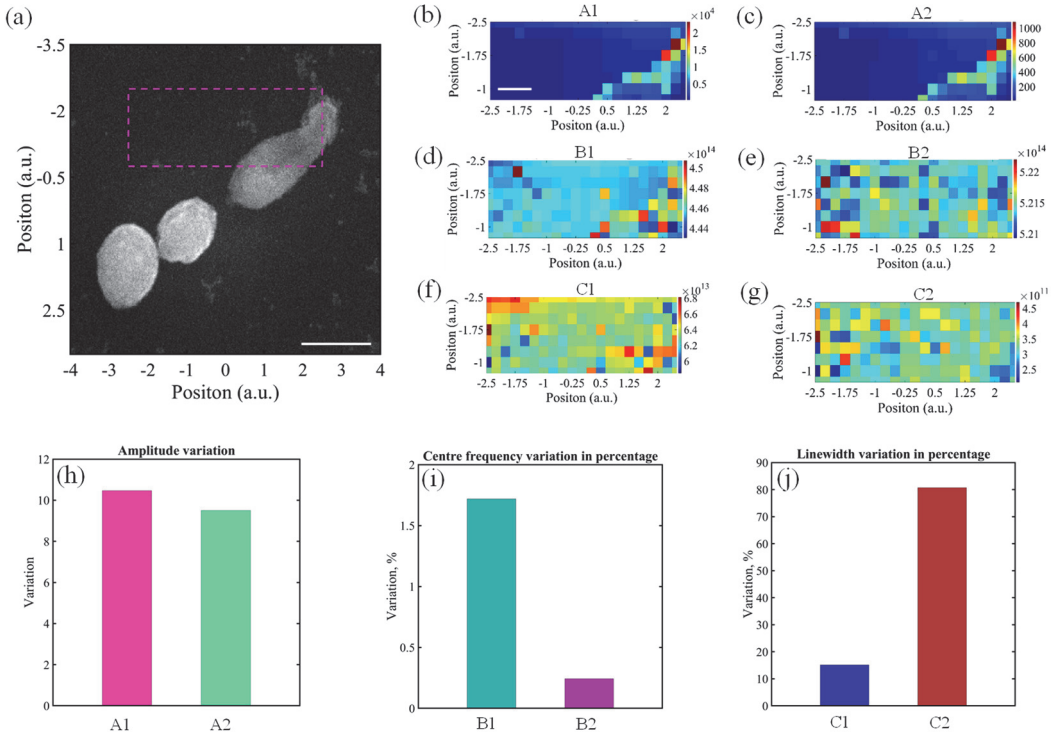

Fig. 2.13. Mapping of the CL spectrum fitting results. (a) SEM image of an ND cluster. The purple dash line box in the area has the CL mapping measurement. The scale bar is 1 μm. (b-g) Parameters A_1 (PSB amplitude), A_2 (ZPL amplitude), B_1 (PSB centre frequency), B_2 (ZPL centre frequency), C_1 (PSB linewidth), C_2 (ZPL linewidth) maps derived from CL spectrum fitting results (the area corresponding to the purple dash line box in (a)). The scale bar is 500 nm. (h-j) The variations of the parameters maps in (b-g), which calculated by (maximum - minimum)/average.

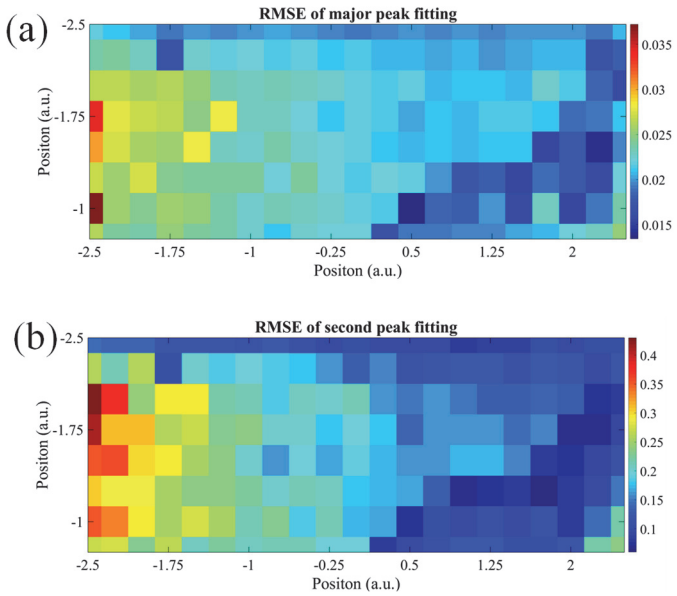

Fig. 2.14. Normalized RMSE of the spectrum fittings. Normalized RMSE of the spectrum fittings of the major peaks (a) and second peaks (b), respectively.

2.3.3 Inter-cluster variation of nitrogen vacancy zero centres spectra

In order to evaluate the variation of CL spectra across different ND clusters, we characterize

six clusters with characteristic sizes and shapes (see Fig. 2.15 (a)). All spectra are recorded under the same SEM conditions (10 kV, 1.9 nA) and spectrometer integration time with 3s. The electron beam is positioned at the centre of each cluster. We observe that their PSBs overlap, while their ZPLs have some difference to each other as illustrated in Fig. 2.15 (b-c). The variations of PSBs and ZPLs amplitude have a large variation due to the NV centres concentration variation between NDs clusters as shown in Fig. 2.15 (d). The variations of centre frequencies and FWHMs are similar with the intra-cluster situation, the variations of centre frequencies are smaller than 2% (see Fig. 2.15(e)). The variation of FWHM in ZPL is larger than in PSB (see Fig. 2.15(f)), which can also be observed in Fig. 2.15(c). The factors leading to these difference maybe come from the strain effect [102].

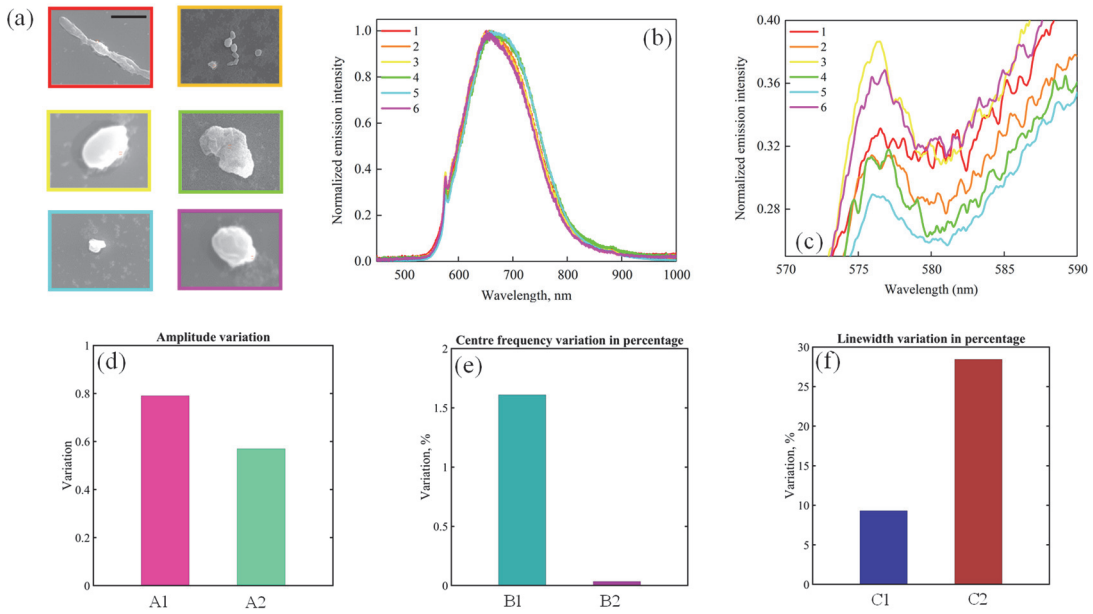

Figure 2. 15. CL of NV centres in different NDs clusters. (a) SEM image of six different NDs clusters, scale bar is 1μm. (b) Normalized CL spectrum of NDs clusters in the (a). (c) Enlarged CL spectrum of NDs clusters in (a) around the wavelength of 575nm. There is no quantitative study. We need to see all fitted parameters here. (d-f) The variations of parameters A_1 (PSB amplitude), A_2 (ZPL amplitude), B_1 (PSB centre frequency), B_2 (ZPL centre frequency), C_1 (PSB linewidth), C_2 (ZPL linewidth) derived from CL spectrum fitting results of these six NDs clusters in (a). Calculated by (maximum - minimum)/average.

2.3.4 Time resolved cathodoluminescence of nitrogen vacancy centres in nanodiamonds

We measured the decay time of photons emitted by NV^0 centres around their ZPLs, in which we set the centre wavelength of the gratings in the spectrometer as 575nm as shown in Fig. 2. 16 (a). The slit width of the output of the spectrometer can be set from 0 to 2 μm which corresponds to the bandwidth from 0 to 3.6 nm. To understand whether the lifetime depends on the bandwidth of photons at the wavelength of 575nm selected for TR-CL, we collected the decay trace of NV centres in the same NDs cluster with a series of slit widths as shown in Fig. 2.16 (b). The decay traces are fit by two exponentials:

$$I(t)=a_1\big(1-\delta(t+a_2)\big)+0.5a_1\delta(t+a_2)(e^{-\frac{t+a_2}{\tau_1}}+e^{-\frac{t+a_2}{\tau_2}})+a_3, \qquad (2.12)$$

where the fast exponential term corresponds to the carrier lifetime [31], while the slow exponential term represents the lifetime of NV^0 centers. Figure 2. 16 (b) shows the fits matching very well with the raw data (all the normalized RMSE is ~5%). I observe the NV centres lifetime varied with the bandwidth of photons selected for TR-CL as shown in Fig. 2. 16 (c), the variation is smaller than 6 ns. I set the bandwidth for all our TR-CL measurements as 3.6 nm to have the highest output from the spectrometer.

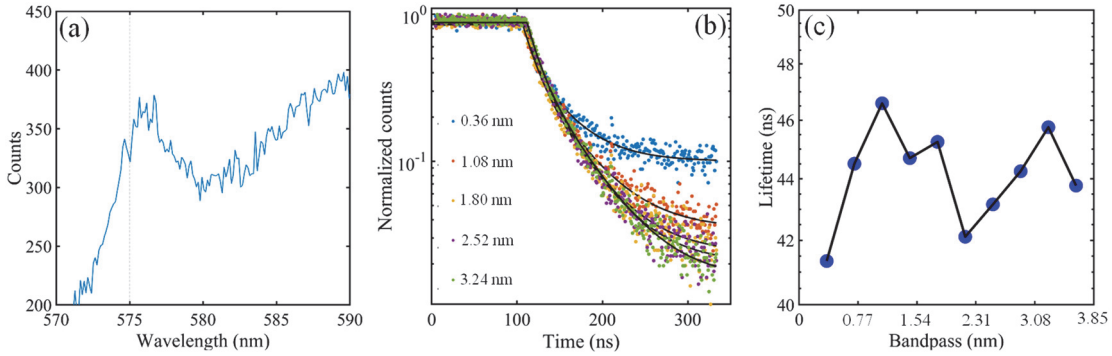

Fig. 2.16. Dependence of lifetime on the spectrometer bandwidth. (a) CL spectrum of NV centre around zero phonon line. (b) Decay traces (dot lines) and fitted curves (solid lines) of NV^0 centres for bandwidths of 0.36 nm, 1.08 nm, 1.8 nm, 2.52 nm and 3.24 nm, respectively. (c) NV^0 centre lifetimes vs bandwidth.

The centre wavelength of photons selected for TR-CL measurement may also affect the measured lifetimes. To study this, we selected centre wavelengths of the spectrometer from 565 nm to 715 nm with fixed bandwidth at 3.6 nm. We observe there is also a variation of lifetimes when changing the centre wavelength (see Fig. 2. 17 (b)), the variation is smaller than 8 ns (17%). I set the centre wavelength of the spectrometer always at 575 nm for all the TR-CL measurements.

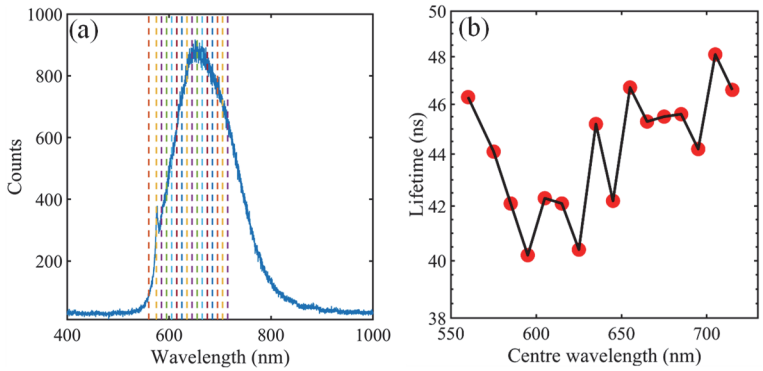

Fig. 2.17. Lifetime relation with detected centre wavelength. (a) The centre wavelengths of photons selected for TR-CL (dash line). (b) Correlation of NV^0 centre lifetimes and the centre wavelength of photons selected for TR-CL.

2.3.5 Statistical distribution of lifetimes of nitrogen vacance centres in nanodiamonds

As discussed in chapter 1, there is a large variation of NV centres in NDs across the substrate. I selected 60 NDs clusters with similar size on Si_3N_4 membrane for TR-CL measurements. Fig. 2. 18 present the distribution of the measured lifetimes of NV centers. I characterized the statistical distribution of the lifetimes by the corresponding average (μ) and the standard deviation (σ). NV centers on Si_3N_4 are seen to exhibit an average lifetime (μ=24 ns) and a broad distribution (σ=8 ns).

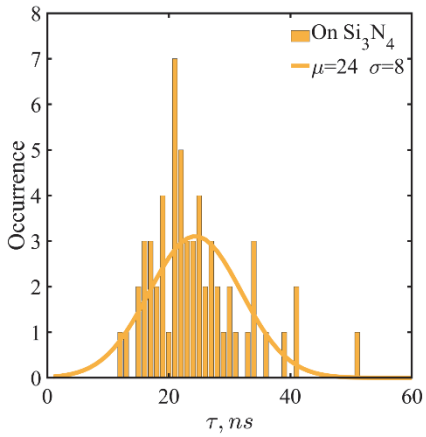

Fig. 2.18. Lifetime distribution NV^0 centres in NDs on Si_3N_4 membrane. The histogram is obtained from measurements of 60 different ND clusters is fitted by a Gaussian distribution, where μ is the mean and σ is the standard deviation (in ns).

2.4 Numerical modelling

The calculation of the properties of emitters forms a central part of the current thesis. However, this problem can be treated analytically only for relatively simple systems. For instance, analytical expressions have been found for fluorescence emission at dielectric and metal film interfaces [135]; light emission by magnetic and electric dipoles close to a plane interface [136]; dipole lifetime in stratified media [137]. However, the hybrid system of NV centres in NDs on bulk and thin film substrates, as well as metasurfaces, is substantially more complex and cannot be tackled analytically. Therefore, I employed a commercial solver of Maxwell's equations, COMSOL v5.3a.

2.4.1 Finite element modelling

Finite element analysis (FEA) is a numerical method aiming to approximately solve problems that can be formulated with partial differential equations and functional minimization [138], which first applied to a torsion problem by Courant [139]. FEA becomes more and more popular, especially in the solid mechanics community since then. Moreover, the development of powerful supercomputer and the elimination of spurious results make the FEA have numerous applications in electromagnetics problems during the last decades. Furthermore, it has important advantages compared with alternative numerical simulation methods, such as the

finite difference time domain (FDTD) approach. In terms of this work, the most important reason is its ability to handle very complex geometries efficiently. FEA is applied to solve the partial differential equations within a space Ω, subject to boundary conditions on boundary $\partial\Omega$ of this space:

$$L\phi = f, \tag{2.13}$$

where f is the excitation, L is a linear differential operator, and ϕ is unknown. The first step of FEA method is to appropriately discretize the domain and approximate the ϕ based on its values ϕ_i in these discrete locations indexed by i and interpolation in the whole domain Ω by a basis function N_i:

$$\phi \backsimeq \sum_i N_i \phi_i, \tag{2.14}$$

then, a residual is defined in the Galerkin formulation [140]:

$$R = L\sum_i N_i \phi_i - f, \tag{2.15}$$

which is the difference between the exact and approximate solutions. Using appropriate weighting functions $W = \sum_j W_j$ to minimize this residual to average R over Ω, which leads to the following linear system of equations:

$$K \cdot \Phi = F, \tag{2.16}$$

where $K_{ij} = \int_\Omega W_i L N_j$, $\Phi_i = \phi_i$ and $F_i = \int_\Omega W_i f$. Well established methods from linear algebra can be used to solve the system equation (2.16). When the electromagnetics is high frequency, FEA is applied to the wave equation for the electric (or magnetic field) over a space Ω:

$$\vec{\nabla} \times \frac{1}{\mu_r} \vec{\nabla} \times \vec{E} - k_0^2 \varepsilon_r \vec{E} = -ik_0 Z_0 \vec{J}, \tag{2.17}$$

with boundary conditions: $\hat{n} \times \vec{E} = 0$ and $\hat{n} \times \vec{\nabla} \times \vec{E} = \vec{N}$ on the disjoint surface boundaries of Ω, $\partial\Omega_D$ and $\partial\Omega_N$, respectively. In this formulation, a dependence of the type $e^{i\omega t}$ has been assumed, while $k_0 = \frac{\omega}{c}$, μ_r and ε_r are the relative permeability permittivity tensors, respectively, and $Z_0 = \sqrt{\mu_0/\varepsilon_0}$ is the impedance in free space. The equation (2.17) has infinite degrees of freedom, therefore, it has to be discretized to solve the problem numerically. The discretization is taken by approximating the domain Ω with standard geometrical shapes which usually called elements. The elements are usually chosen in triangles for two-dimensional problems, while in tetrahedra for three dimensional because are easier to cover arbitrarily shaped domains (see Fig. 2.20).

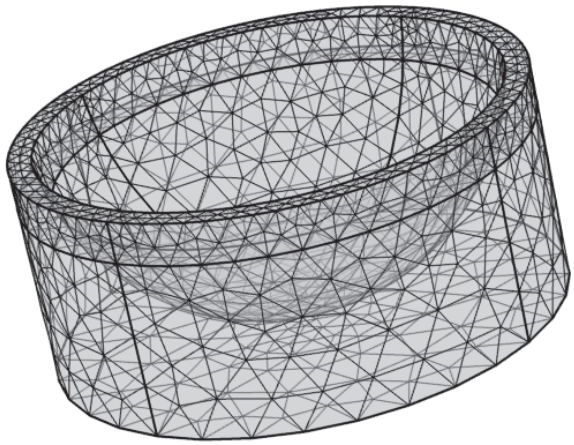

Figure 2. 19. Example of three-dimensional tetrahedral mesh elements.

After the discretization has finished, a continuous approximation of $\vec{E}$ can be obtained with a set of interpolating basis function after the values of $\vec{E}$ inside each element have been approximated by assigning values in certain points. Linear interpolating functions are usually employed to assign the electric values at nodes of the element. In addition, higher order polynomials or vector bases can also be used to assign the electric values [141]. Particularly, vector interpolating functions used to assigned values at the edges of the element leading to an appealing approach that is known to minimize spurious errors [140]. Hence, e, $\vec{E}$ in each element can be approximated as [141]:

$$\vec{E}^e(x,y,z) = \sum_{i=1}^{m} \vec{N}_i^e(x,y,z) E_i^e, \tag{2.18}$$

where E_i^e is the tangential component and $\vec{N}_i^e(x,y,z)$ is the vector basis function of the electric field at edge i of element e with m nodes. Then, the electric field over the entire domain Ω is obtained by summing over all element edges (excluding those at $\partial\Omega_D$ where the tangential component of $\vec{E}$ vanishes):

$$\vec{E} = \sum_{i=1}^{l} \vec{N}_i \vec{E}_i, \tag{2.19}$$

at this point Eq. (2.17) is multiplied by the testing function W or weighting function and integrated over the whole domain Ω resulting in [141]:

$$\iiint_V \left[(\vec{\nabla} \times \overrightarrow{W}) \mu_r^{-1} (\vec{\nabla} \times \vec{E}) - k_0^2 \overrightarrow{W} \varepsilon_r \vec{E}\right] dV =, \tag{2.20}$$

$$= \iint_{\partial\Omega} \hat{n} \cdot \left[\overrightarrow{W} \times (\mu_r^{-1} \vec{\nabla} \times \vec{E}\right] dS - \iiint_V \left[-\mathrm{i} k_0 Z_0 \overrightarrow{W} \cdot \vec{\jmath}\right] dV, \tag{2.21}$$

by separating the surface integral on domains $\partial\Omega_D$ and $\partial\Omega_N$ to introduce the boundary conditions. In the end, expanding the test function similarly to the electric field by $\overrightarrow{W} = \sum_{j=1}^{l} \vec{N}_j \vec{E}_j$ and replacing in Eq. (2.20), which obtain the following linear system of equations results [141]:

$$K \cdot E = b, \tag{2.22}$$

where K is the stiffness matric with the form:

$$K_{ij} = \iiint_V [(\vec{\nabla} \times \vec{N}_j)\mu_r^{-1}(\vec{\nabla} \times \vec{N}_i) - k_0^2 \vec{N}_j \varepsilon_r \vec{N}_i]\, dV - \iint_{\partial\Omega} \hat{n} \cdot [\vec{N}_j \times (\mu_r^{-1}\vec{\nabla} \times \vec{N}_i]dS - \iiint_V [-ik_0 Z_0 \vec{W} \cdot \vec{J}]\, dV, \quad (2.23)$$

and

$$b_j = -\iiint_V [ik_0 Z_0 \vec{N}_j \cdot \vec{J}]\, dV, \quad (2.24)$$

A commercial software package COMSOL 5.3a based on FEA was employed to do the simulation work in this thesis. Two types of error occur during FEA calculations. The first type inherently exists in the approximation procedure, all the details of the field variation cannot be captured due to the geometry domain generally is of arbitrary shape, is approximated by elements of a specific shape. But this type of error can be reduced by refining the mesh. In my simulations, errors were reduced by refining the mesh and monitoring the fields at a specific boundary, the mesh was stopped refining until the error of the new mesh is not different from the previous step with within a 6% or smaller error margin. The second type of errors come from the finite number of digits used, such random errors were found to be of the order 10^{-5} or smaller in the simulation work here, which were not given further consideration.

2.4.2 Modelling of nitrogen vacancy centre in nanodiamond emission

I have modelled the emission properties of NV centres in NDs on different substrates according to the following procedure. To explain the modelling method, I take an example of a single NV centre in ND on a Si substrate. The simulations were also performed using the RF module of COMSOL 5.3a. The simulation domain of my model is shown in Fig. 2.21. It is represented by a cylinder with a diameter of 1.5 μm and a height of 3 μm. All surfaces of the cylinder were terminated with scattering boundaries. A ND was modelled as a 120 nm large dielectric sphere with the refractive index 2.40 [142]. The refractive index of the Si substrate was set to $4.00 + 0.03i$ [143]. A NV center radiating at the wavelength of 575 nm was introduced as a volume polarization density oscillating inside a sphere with radius r_s = 5 nm, which was placed in the center of the ND. The direction of the polarization (and, therefore, the orientation of the effective electric dipole moment) was set either parallel or perpendicular to the substrate. The total power emitted by the NV center, P_{rad}, was calculated by integrating the power flow over the surface of a sphere with a radius r_t = 6 nm, which encapsulated the emitting NV center. The lifetime of the NV center was obtained as $\tau = \frac{\tau_{bulk} P_{bulk}}{P_{rad}}$, where P_{bulk} is the total power emitted by the NV center inside the bulk diamond and τ_{bulk} corresponds to the known bulk lifetime $\tau_{bulk} = 19$ ns [35]. P_{bulk} was calculated in the same way as P_{rad} except that the entire simulation domain was set as diamond. The total decay rate was calculated as $\gamma_{tot} = \frac{1}{\tau} = \frac{P_{rad}}{\tau_{bulk} P_{bulk}}$. The radiative decay rate was given by $\gamma_{rad} = \frac{P_0}{\tau_{bulk} P_{bulk}}$, where P_0 is the power radiated into the far-field zone above the substrate (since the substrate was lossy, the power radiated into the substrate was eventually absorbed). The non-radiative decay rate was calculated as $\gamma_{non} =$

$\gamma_{\mathrm{tot}} - \gamma_{\mathrm{rad}}$. Except these are two types of error occur during FEA calculatons. Another type of the error occurs in this simulation due to there is still some reflection from the SBC, here, the errors were reduced by increasing the simulation domain and monitoring the fileds at the SBC, the simulation domain size was stopped increasing until error of the new domain size is not different with previous step with within a 5% or smaller error margin.

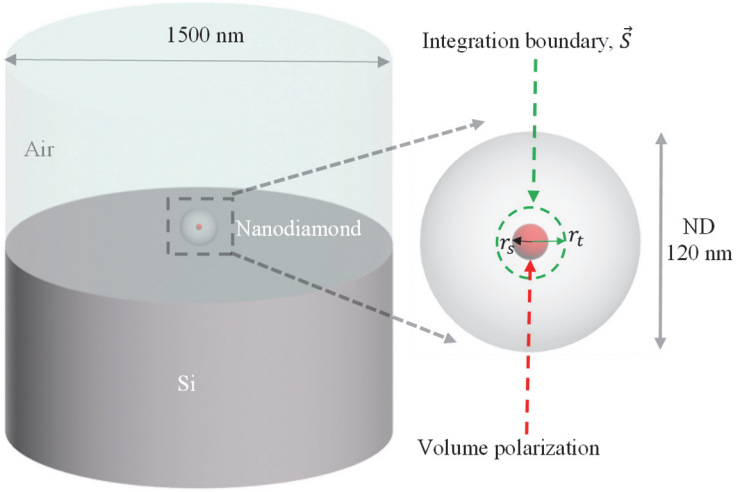

Fig. 2.20. Schematic illustration of lifetime calculations for single ND on Si substrate. The NV^0 center is introduced as a volume polarization density with the orientation along the x-axis (parallel) or z-axis (perpendicular) oscillating inside a sphere of radius r_s =5 nm. The total radiated power is calculated as the surface integral of power flow $\vec{P}$ through a spherical surface $\vec{S}$ of radius r_t =6 nm encapsulating the emitting dipole, which is situated entirely inside the ND with a radius of 60 nm.

2.4.3 Modelling of cathodoluminescence from a plasmonic substrate

In my work, CL from plasmonic films is also modelled by COMSOL 5.3a. To illustrate the simulation process, I take as an example a 50 nm thick Au film on a 100 nm thick Si_3N_4 membrane. The CL process is modelled with a vertically oriented electric placed 30 nm above the Au film surface [144]. The simulation domain is a cylinder with a radius of 1.5 μm and a height of 3 μm. The size of the simulation domain is chosen in a way that ensures negligible interaction between the domain boundaries and the dipole emitter. The domain is terminated by scattering boundaries, which ensure no backscatter into the simulation domain, as shown in Fig, 2.22 the boundary in the shape of a spherical cap is used to evaluate the far-field radiation through integrating the Poynting vector over the boundary surface. The shape of this boundary is chosen in a way that corresponds to the collection angle of the parabolic mirror used in the cathodoluminescence experiments. The distance between the dipole emitter and the far-field evaluation boundary was set to ~2λ to minimize evanescent field contribution. Similar to the modelling of NV centre emission in ND, except these two types of error occur during FEA calculations. Another type of the error occurs in this simulation due to there is still some reflection from the SBC, here, the errors were reduced by increasing the simulation domain and monitoring the fields at the SBC, the simulation domain size was stopped increasing until the

error of the new domain size is not different with the previous step with within a 5% or smaller error margin.

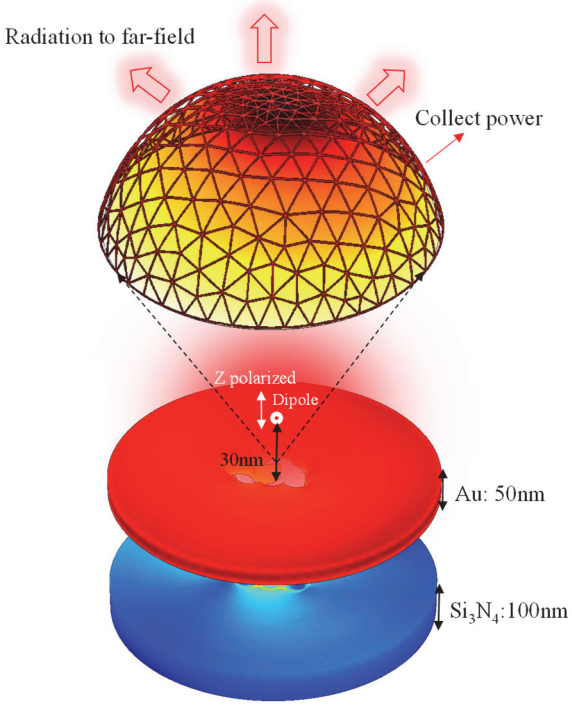

Figure 2. 21. Modelling of CL from air holes in Au film (50 nm) on Si_3N_4 membrane (100 nm). A z-polarized electric dipole 30nm above the Au film surface. The distance between the dipole and the spherical cap for power collection is 1.5 μm.

2.5 Feedforward neural networks

A feedforward neural network is an artificial neural network wherein connections between the nodes do not form a cycle [145]. Take supervised learning as an example, suppose we have a training sample set $(x(i),\ y(i))$. Then the neural network algorithm can provide a complex and nonlinear hypothetical model $h_{W,b}(x)$, which has parameters W, we can fit our data with this parameter. The simplest neural network consists of only one neuron as Fig. 2. 23 shows.

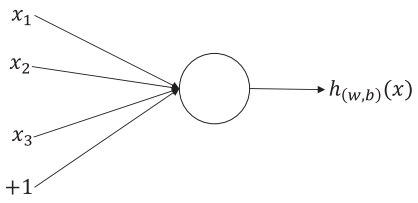

Figure 2. 22. Diagram of a single neuron.

This neuron is an arithmetic unit with x_1, x_2, x_3 as input and +1 as bias, and the output is

$$h_{W,b}(x) = f(W^T x) = f(\sum_{i=1}^{3} W_i\, x_i + b), \tag{2.25}$$

Where the function f is activation function, which usually is a sigmoid function with range [0, 1] or hyperbolic tangent function with range [-1, 1]. The neural network is formed by connecting

many single neurons together so that the output of one neuron can be the input of the other neurons. Figure 2. 24 shows a simple neural network.

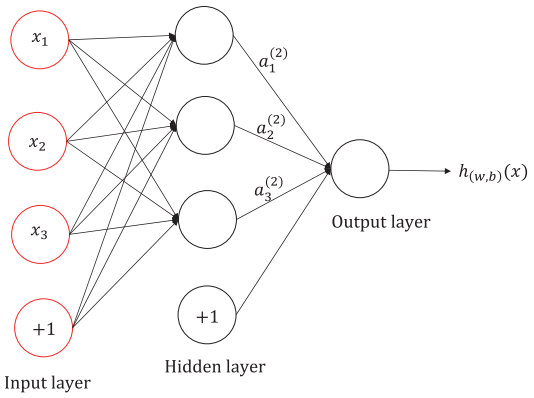

Figure 2. 23. A simple feedforward neural network.

The circles with x_1, x_2, x_3 represent the input to the neural network, a circle labelled '+ 1' is a bias node and there is single output. The layer composed of all the nodes in the middle is a hidden layer because we cannot observe their values in the training sample set. The parameters $(W, b) = (W^{(1)}, b^{(1)}, W^{(2)}, b^{(2)})$, in which $W_{ij}^{(l)}$ is the connection parameter between layer l with unit j and layer l+1 with unit i, $b_i^{(l)}$ is the bias term of layer l+1 with unit i. $a_i^{(l)}$ is the activation value of layer l with unit i. $a_i^{(1)} = x_i$ is the input value of unit i. For a given set of parametersW, b, the neural network can calculate the output according to function $h_{W,b}(x)$. The calculation steps of this neural network are as follows:

$$a_1^{(2)} = f\left(W_{11}^{(1)}x_1 + W_{12}^{(1)}x_2 + W_{13}^{(1)}x_3 + b_1^{(1)}\right), \tag{2.26}$$

$$a_2^{(2)} = f\left(W_{21}^{(1)}x_1 + W_{22}^{(1)}x_2 + W_{23}^{(1)}x_3 + b_2^{(1)}\right), \tag{2.27}$$

$$a_3^{(2)} = f(W_{31}^{(1)}x_1 + W_{32}^{(1)}x_2 + W_{33}^{(1)}x_3 + b_3^{(1)}), \tag{2.28}$$

$$h_{W,b}(x) = a_1^{(3)} = f(W_{11}^{(2)}a_1^{(2)} + W_{12}^{(2)}a_2^{(2)} + W_{13}^{(2)}a_3^{(2)} + b_1^{(2)}), \tag{2.29}$$

We can also build the feedforward neural network that contains multiple hidden layers and multiple outputs as shown in Fig. 2.25. According to the previously mentioned equations to calculate the activation values of hidden layers step by step.

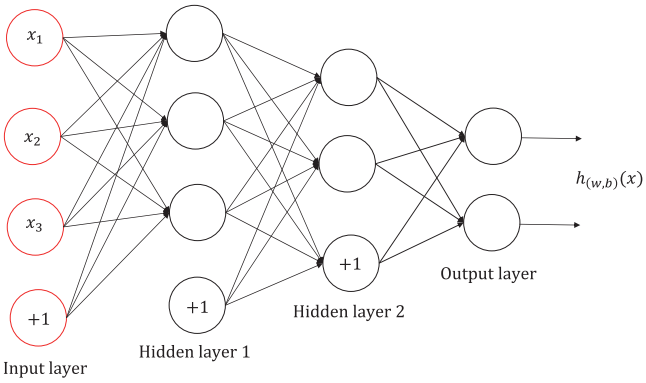

Figure 2. 24. Feedforward neural network with two hidden layers.

2.5.1 Implementing and training feedforward neural network in Matlab

The Deep Learning Toolbox™ provides a framework for designing and implementing deep neural networks with algorithms, pre-trained models, and apps. Convolutional neural networks (ConvNets, CNNs) and long short-term memory (LSTM) networks can be used to perform classification and regression on image, time-series, and text data. We can build network architectures such as generative adversarial networks (GANs) and Siamese networks using automatic differentiation, custom training loops, and shared weights. With the Deep Network Designer app, we can also design, analyze, and train networks graphically. Feedforwardnet is the feedforward neural network function in this toolbox. For example, use the 'feedforwardnet' function to create a three-layer feedforward network, this network has one hidden layer with 20 neurons, an input layer with and an output layer we can define: net = feedforwardnet(20). We also set the input as a 16 x N matrix and output as a 30 x N matrix, where N is the number of the dataset for the training and the validation process. The created feedforward neural network is shown in Fig 2.26. Then use the train function to train the feedforward network. After the network is trained and validated, the network object can be used to calculate the network responding to any input.

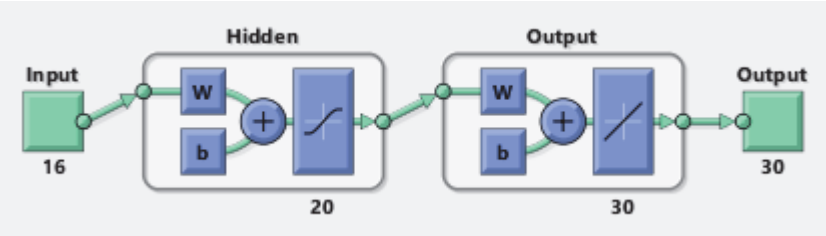

Figure 2. 25. Feedforward neural network has one hidden layer with 20 neurons, an input layer with 16 neurons and an output layer with 30 neurons.

2.6 Summary

In summary, I have shown the sample fabrication methods which cover thin film deposition, nanostructuring, NDs disperse on substrates. The chalcogenide film deposition technique makes it possible to control the permittivity various in the whole sample area. I have also shown the simulation methods which employing the finite element analysis method (COMSOL) to model the emission properties of single NV centre in ND, model the CL from plasmonic apertures. I have shown the characterization process in detail, here, I employed the TR-CL technique which has been introduced from principle to instrumentation in lab. A key parameter of TR-CL system is the time resolution which is about 3ns of our system characterized by measuring the response time of TR from the gold surface. I also have shown the CL spectrum and lifetimes properties of NV centres in NDs clusters, investigated how the lifetime varied on bandwidth and centre wavelength of photons selected for TR-CL, which pave the way for my next step experiments, such as always set the bandwidth and centre wavelength for a constant value.

Chapter 3

Decay rate enhancement of diamond nitrogen vacancy centres on diamond thin films

3.1 Introduction

Thin film based Fabry-Perot (FP) cavities have been applied in many areas of optical science, such as mode selectors [146] or wavelength filters [147]. Light is reflected at both boundaries and a resonant standing wave pattern forms due to the refractive index difference below and above the film. Such resonances have been employed to enhance light-matter interactions in a wide range of settings. For instance, plasmonic nanoparticles hybridized with FP cavities boost sensing figure-of-merit, which provides interesting features such as remote-sensing ability, incident-angle independent resonances, strong polarization dependence, lateral ultra-small sensing volume and strongly improved detection resolution [148]. There is a modification of spontaneous emission rate in planar dielectric microcavity [149], besides, FP cavities enhance spontaneous emission have been observed [150].

In this chapter, I report a two-fold increase of the decay rate for ensembles of NV^0 emitters resting on a thin diamond film, as compared to a bare silicon substrate, which I observed experimentally using time-resolved cathodoluminescence (TR-CL). The increased decay rates are attributed to the existence of non-radiative channels and the coupling of the emitters to FP modes of the thin film.

3.2 Lifetime distribution of nitrogen vacancy centres in nanodiamonds on diamond thin films

Silicon is one of the most important semiconductor materials of modern information technologies. Chips based on silicon power silica fibres, computers process signals and photonic technology based on it providing integrated optical solutions [151]. Diamond has high hardness, ultra-wide band gap, excellent carrier mobility and excellent thermal conductivity, which is also one of the basic materials for realizing the 'Post-Moore Era' of electronic, optoelectronic and quantum chips [152]. Thus studying of their emission properties in different environments and in particular CMOS compatible materials is of great interest. In my experiments, the NDs were deposited by drop casting on two substrates: a 200 nm thick diamond film on silicon and a bare silicon wafer (see Fig. 3.1(b)). Deposition of the diamond film was performed by my colleague Dr Artemios Karvounis (see Chapter 2, section 2.1.1). I characterized NV centers in the deposited NDs at room temperature using the TR-CL system

which based on SEM operating in fixed-spot mode (see Chapter 2, section 2.3).

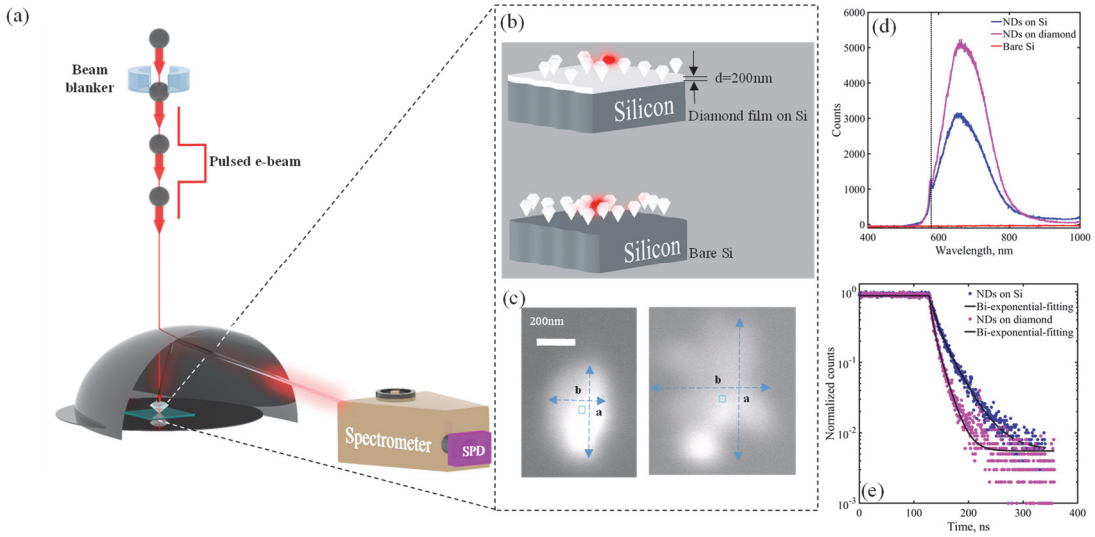

Figure 3. 1 (a) Schematic of the scanning electron microscope-based system for time-resolved electron-induced light emission spectroscopy which has been described in detail in chapter 2, section 2.2. (b) The samples consist of NDs deposited on two different substrates: i) a 200 nm thick diamond film on 500 µm thick silicon and ii) a 500 µm thick silicon substrate. (c) SEM images of ND clusters are shown at the bottom. The blue rectangle marks the position of the electron beam during TR-CL measurements. The dimensions of the cluster are indicated by the longer and shorter edge lengths, a and b, respectively. (d) CL spectrum of NVs on Si (blue line), on diamond film (purple line) and background signal (red line). The dashed line indicates the wavelength zero phonon line. (e) TR-CL trace of NVs on Si (blue circles), on diamond film (purple line) and bi-exponential fittings (black lines).

I selected 60 ND clusters on each type of substrate with sizes in the range 120-1500 nm (see Fig. 3.1 (c)) and studied the emission of the neutral NV^0 centers at the zero phonon line, as shown in Fig. 3.1(d). Thus, only photons in the range of 575 ± 1.8 nm were selected at the input of the single photon detector. Figures 3.2 (a-b) present the distribution of the measured lifetimes of NV centers deposited on a bare Si substrate and on a diamond film, respectively. I characterized the statistical distribution of the lifetimes by the corresponding average (µ) and the standard deviation (σ). NV centers on bare Si substrate are seen to exhibit long lifetimes (µ=30 ns) and a broad distribution (σ=6 ns). On the other hand, for NV centers on the diamond film, I observe a substantial shortening of the average lifetime (µ=17 ns) accompanied by a narrower distribution (σ=4 ns). Figures 3.2 (c-d) present the distribution of the measured intensities of NV centers deposited on a bare Si substrate and on a diamond film, respectively. NV centres on bare Si substrate has lower average intensity ($\alpha\beta = 0.633 \times 10^4$ counts) and smaller distribution ($\alpha\beta^2 = 0.141 \times 10^4$ counts) compared with NV centres on diamond (higher intensity $\alpha\beta = 0.731 \times 10^4$ counts and broader distribution $\alpha\beta^2 = 0.271 \times 10^4$ counts). The shorter lifetimes and lower intensities of NV centres on diamond means the enhanced total decay rates resulted from more emitted powers decay in the nonradiative channel which due to the NV centres have stronger interactions with Si substraste through the diamond film cavity.

The lifetime reduction in this work is comparable to reduction of the lifetime for NV^0 centres in an ND hybridized with an Ag nanocube [108], in which the lifetime reduction was caused by the coupling between NV^0 centers in NDs and surface plasmons in Ag nanocubes (see table 3.1).

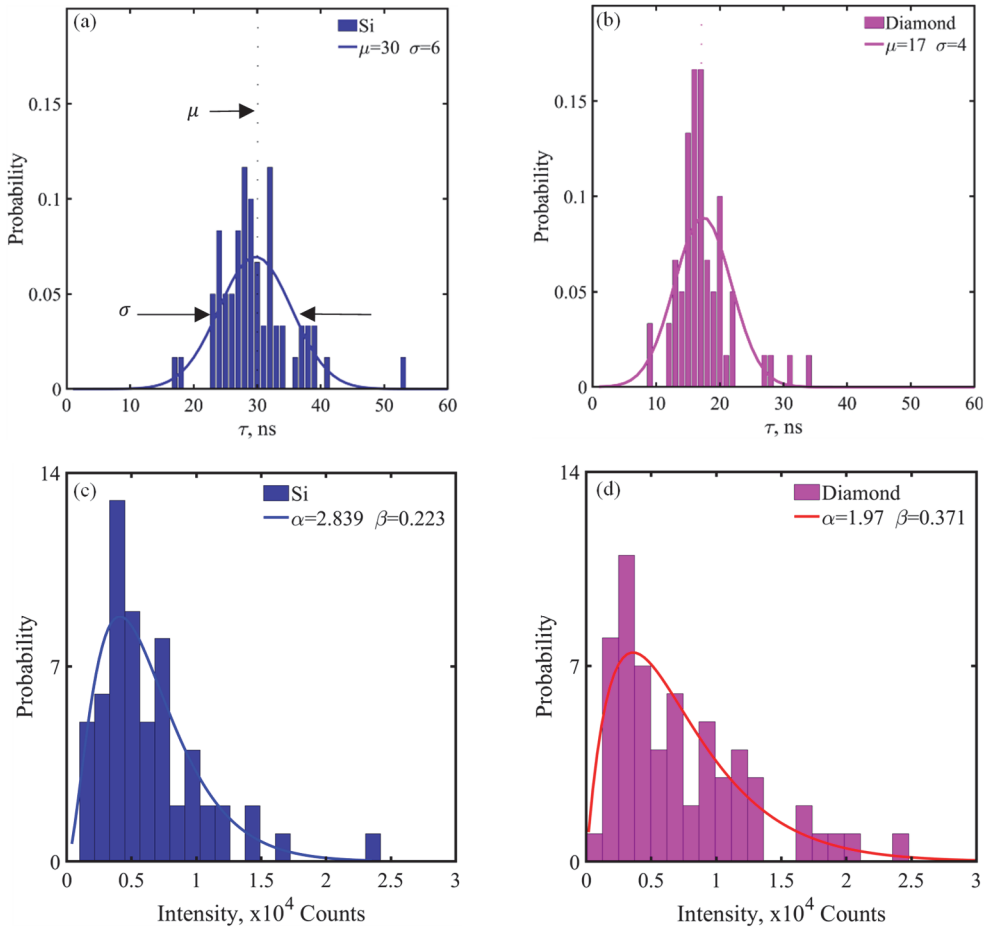

Figure 3.2. Lifetime distributions of NV^0 centers in diamond nanoparticles deposited on silicon (a) and diamond nanofilm cavity (b). The histograms are obtained from measurements of 60 different ND clusters on each substrate and are fitted by a Gaussian distribution, where μ is the mean (dotted vertical lines) and σ is the standard deviation (in ns). Intensity distributions of NV^0 centers in diamond nanoparticles deposited on silicon (c) and diamond nanofilm cavity (d). The histograms are fitted by a Gamma distribution, where $\alpha\beta$ $(0.633\ on\ Si, 0.731\ on\ diamond)$ is the mean and $\alpha\beta^2$ $(0.141\ on\ Si, 0.271\ on\ diamond)$ is the standard deviation (in $\times 10^4$ counts).

Table 3.1. Comparison of decay rate enhancement of NV^0 centre in nanodiamond.

	Resonator	Lifetime of NV^0 centre in ND on substrate only (ns)	Lifetime of NV^0 centre with decay rate enhancement (ns)
Ref. [108]	Ag cube	22.5	12.5
My work	Diamond film	30	17

3.3 Spectral characteristics of nitrogen vacancy centres in nanodiamonds on diamond thin films

Here, I study the influence of the diamond thin film on the spectral characteristics of CL from NDs. The phonon sideband (PSB) centre frequency, PSB line width, zero phonon line (ZPL) amplitude, ZPL centre and ZPL linewidth of CL spectrum were obtained by the methods described in chapter 2. Fig. 3.3 (a-b) presents the distribution of the PSB centre frequency of NV centers deposited on a bare Si substrate and on a diamond film, respectively. NV centers on both substrates are seen to exhibit similar PSB centre frequency (μ=4.536 × 10^{14} Hz on Si and μ=4.530 × 10^{14} Hz on diamond) while there is a broader distribution on diamond (σ =5.3 × 10^{12} Hz) than on Si (σ =3.1 × 10^{12} Hz). This phenomenon is the same for the PSB linewidth, NV centers on both substrates are seen to exhibit similar PSB linewidth (μ=6.461 × 10^{13} Hz on Si and μ=6.046 × 10^{13} Hz on diamond) while there is a broader distribution on diamond (σ =3.3 × 10^{12} Hz) than on Si (σ =2.12 × 10^{12} Hz).

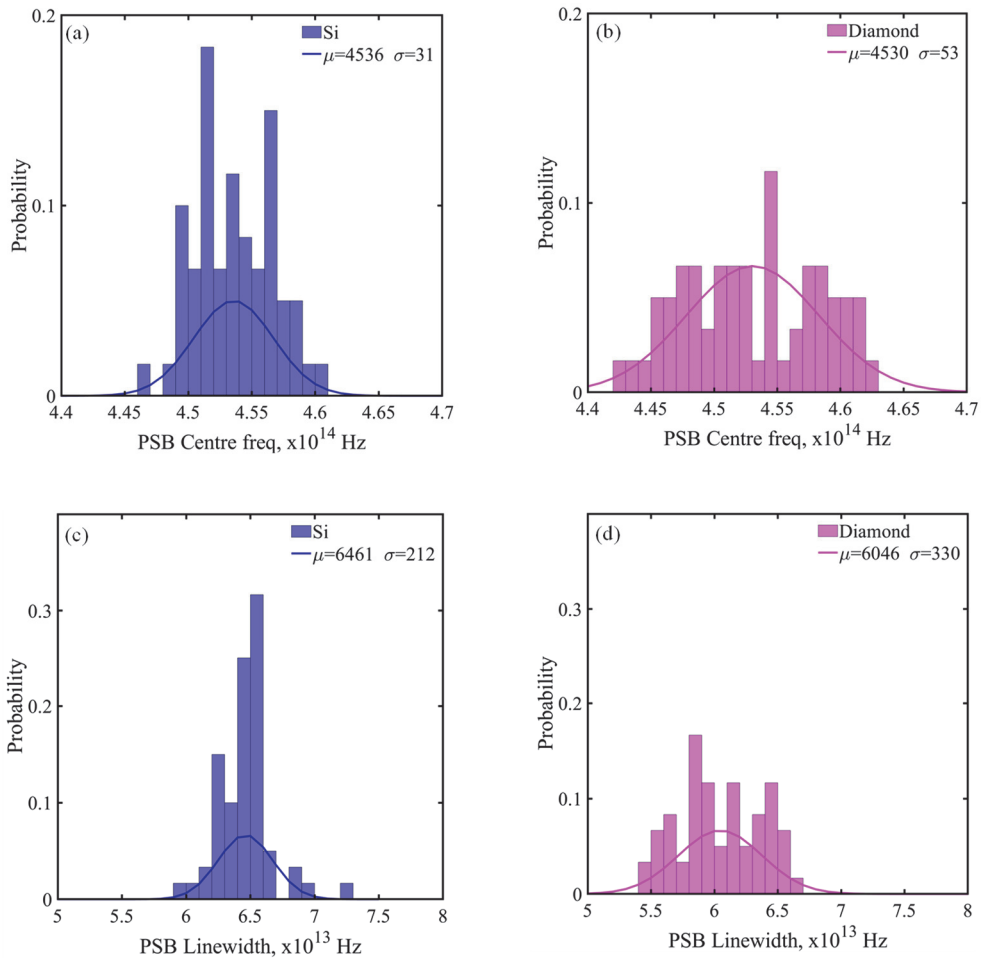

Figure 3.3. Phonon side band (PSB) fitting results of NDs on Si and diamond film, repectively. PSB centre frequency distributions of NV0 centers in diamond nanoparticles deposited on silicon (a) and diamond nanofilm cavity (b). Phonon side band (PSB) linewidth distributions of NV^0 centers in diamond nanoparticles deposited on silicon (c) and diamond film cavity (d). The histograms are obtained from measurements of 60 different ND clusters on each substrate and are fitted by a Gaussian distribution, where μ is the mean and σ is the standard deviation (in × 10^{10}Hz).

In contrast to the PSB distributions, the ZPL distributions have a relatively larger difference between Si and diamond substrate Fig. 3.4 (a-b) shows the distribution of the ZPL amplitude of NV centers deposited on a bare Si substrate and on a diamond film, respectively. Although there is strong variation of the ZPL amplitude across each substrate, the distributions are similar with most ND clusters exhibiting amplitudes smaller than 1000 counts. This expected as local variations of NV^0 ZPL spectrum are known eve in the case of NV^0 centres within the same particle [102].There are however large differences in the ZPL centre frequency and ZPL linewidth distributions as shown in Fig. 3.4 (c-f). Similarly to the PSB centre frequency distribtuions, NV centers on both substrates are seen to exhibit similar ZPL centre frequency (μ=5.207×10^{14} Hz on Si and μ=5.208×10^{14} Hz on diamond). H however, in contrast to the PSB spectrum distributions, the ZPL centre frequency and linewidth distributions have very different shapes on the two substrates, with single and two peaks in the diamond and Si substrates, respectively. While differences in the average and spread of the distributions can be attributed to variations in strain and/or electrostatic environment, the presence of two-peaked distributions deserves careful consideration and one possible explanation could be found on the broader distribution of sizes in the case of the Si substrate, which also appears to present a similar two-peak distribution, albeit less pronounced (see Fig. 3.10). However, I note that there is no correlation between lifetimes and cluster size, which implies that the peculiar distribution shapes of ZPL peaks do not manifest in the time resolved measurements.

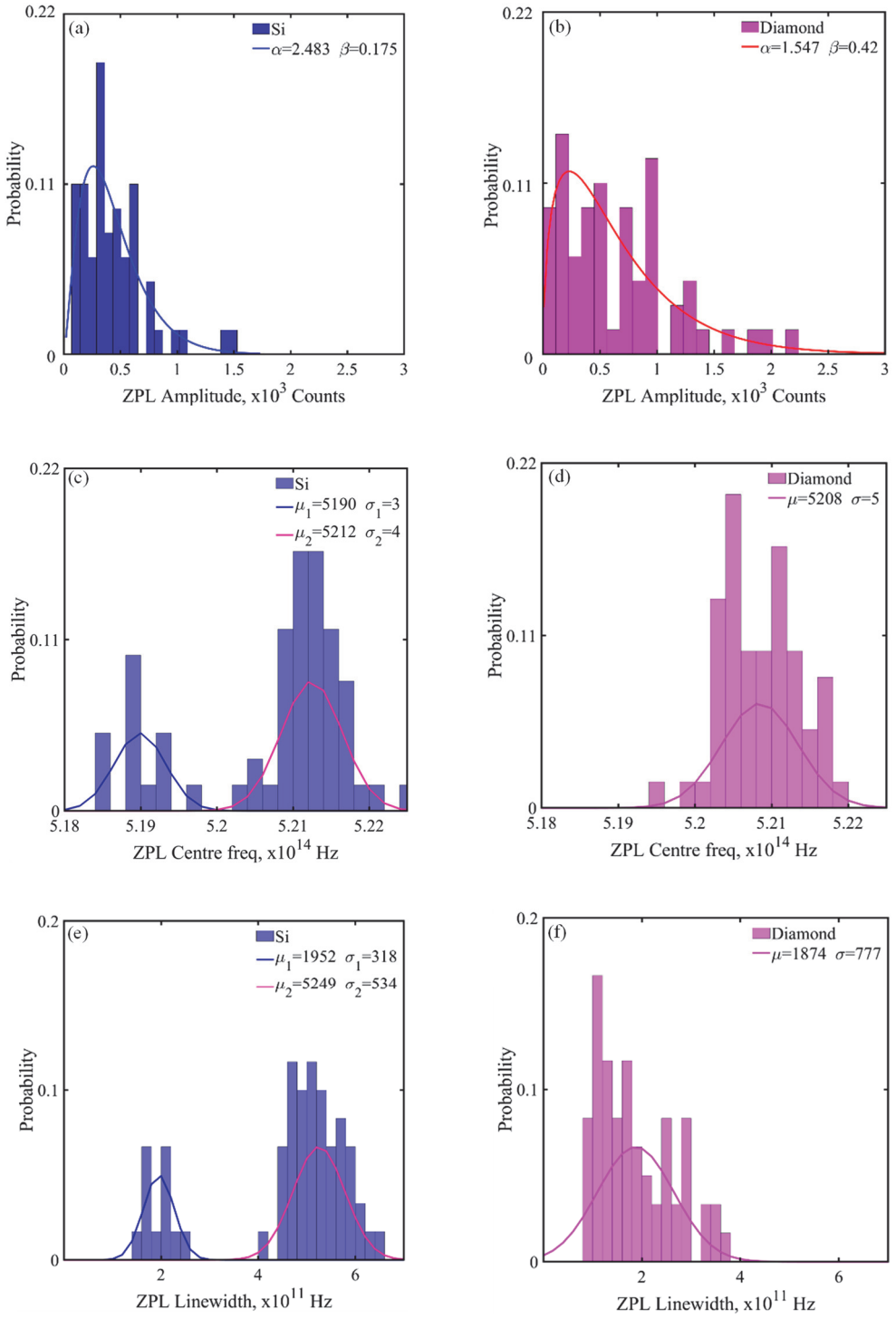

Figure 3.4. Zero phonon line (ZPL) fitting results of NV centres in NDs on Si and diamond film, respectively. ZPL amplitude distributions of NV^0 centers in diamond nanoparticles deposited on silicon (a) and diamond film cavity (b). ZPL centre frequency distributions of NV^0 centers in diamond nanoparticles deposited on silicon (c) and diamond nanofilm cavity (d). ZPL linewidth distributions of NV^0 centers in diamond nanoparticles deposited on silicon (e) and diamond nanofilm cavity (f). The histograms are obtained from measurements of 60 different ND clusters on each substrate and are fitted by a gamma distribution in (a) and (b), where $\alpha\beta$ (0.435 on Si, 0.650 on diamond) is the mean and $\alpha\beta^2$ (0.076 on Si, 0.273 on diamond) is the standard deviation, and double Gaussian distributions in (c) and (e), where μ_1 is first the mean and σ_1 is the first standard deviation (in $\times 10^{10}$ Hz), μ_2 is second the mean and σ is the second standard deviation (in $\times 10^{10}$ Hz), and one Gaussian distribution in (d) and (f) where, μ is the mean and σ is the standard deviation (in $\times 10^{10}$ Hz).

3.4 Simulation and collection efficiency calculation

I argue that the changes in the lifetime distribution observed for NV centers on a diamond film are a result of strong interactions between diamond nanoparticles and guided optical modes in the diamond film. To demonstrate this, I performed full-wave 3D electromagnetic modelling of the emission from a dipole embedded in a diamond nanoparticle placed on a diamond film of varying thickness. Figure 3.5 shows the schematic illustration of the model used in lifetime calculations for a single ND on diamond film on Si. More details about modelling NV centre emission has been introduced in chapter 2. The collection efficiency of the parabolic mirror depends on the orientation of the electric dipole of an NV^0 center, as shown in Figure 3. 4.

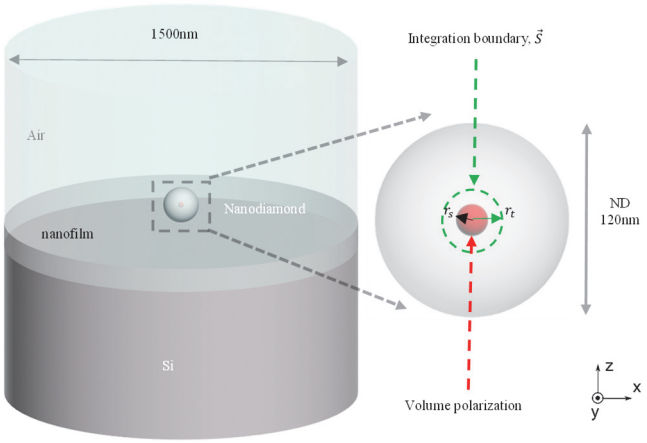

Figure 3.5. Schematic illustration of the model used in lifetime calculations for a single ND on diamond film on Si. The NV^0 center is introduced as a volume polarization density with the orientation along the x-axis (in the plane of the substrate) or z-axis (normal to the substrate) oscillating inside a sphere of radius r_s =5 nm.

In my experiments, the NDs are at the focus of the parabolic mirror. We define $\eta_x^{\parallel} = \frac{P_x}{P_x+P_y+P_z}$, $\eta_y^{\parallel} = \frac{P_y}{P_x+P_y+P_z}$, $\eta_z^{\perp} = \frac{P_z}{P_x+P_y+P_z}$, where P_x, P_y, P_z are the radiated powers collected by the parabolic mirror for dipoles moments of NV^0 centres orientated along x, y, z directions, respectively. Table 3.1 shows the collect efficiencies of a parabolic mirror for a dipole with x, y z-orientation. A summary of the simulated decay rates for different dipole orientations is shown in table 3.2. I can see both the collection efficiency and decay rates are strongly depends on the dipole orientations.

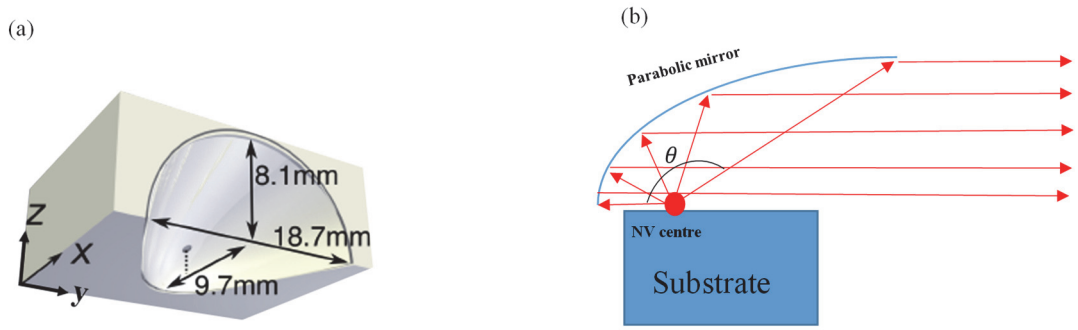

Figure 3.6. Parabolic dimensions. (a) Schematic of the parabolic mirror used for collecting photons emitted by NV centres. (b) Diagram of photon collection. Angle θ is about 135^0 according to the dimensions in (a).

Table 3.2 Collection efficiencies of parabolic mirror for a dipole with x, y z-orientation

Substrates	$\eta_x^{\parallel}$	$\eta_y^{\parallel}$	$\eta_z^{\perp}$
Si	64.04%	18.29%	17.67%
Diamond	48.73%	25.96%	25.31%

Table 3.3 Summary of simulated lifetimes and rates of vertical and horizontal dipole emission and photon loss.

Substrates	$\tau_{Sim}^{\parallel}(ns)$	$\gamma_{Tot}^{\parallel}(\times \mu s^{-1})$	$\gamma_{Non}^{\parallel}(\times \mu s^{-1})$	$\gamma_{Rad}^{\parallel}(\times \mu s^{-1})$
Si	130.55	7.66	5.30	2.36
Diamond	105.15	9.51	7.47	2.04

Substrates	$\tau_{Sim}^{\perp}(ns)$	$\gamma_{Tot}^{\perp}(\times \mu s^{-1})$	$\gamma_{Non}^{\perp}(\times \mu s^{-1})$	$\gamma_{Rad}^{\perp}(\times \mu s^{-1})$
Si	38.21	26.17	17.04	9.12
Diamond	49.31	20.28	16.33	3.95

The average lifetimes can be calculated as:

$$\overline{\tau}_{sim} = \frac{1}{\overline{\gamma}_{sim}} = \frac{1}{(\eta_x^{\parallel} + \eta_y^{\parallel})\gamma_{Tot}^{\parallel} + \eta_z^{\perp}\gamma_{Tot}^{\perp}} \tag{3.1}$$

3.5 Discussion

The modelling also allowed me to distinguish between radiative and non-radiative decay channels. A comparison of computationally obtained and experimentally measured total lifetimes is presented in Table 3.3. In agreement with my experimental results, my simulations show that the lifetime is shorter in the presence of a thin diamond film (81 ns) than in the case of a bare Si substrate (91 ns). I attribute the difference between the values of experimental and numerical lifetimes mainly to the fact that in my numerical calculations I considered single ND particles, whereas experimental measurements involved clusters of NDs. In particular, my numerical results indicate that the faster decay rates obtained for thin diamond films are due mainly to non-radiative loss in the underlying bulk Si (see table 3.2). Importantly, the enhancement or suppression of radiative and non-radiative decay rate depends strongly on the

film thickness (see Fig. 3.7 (a)), which indicates coupling to slab modes in the film[21]. Indeed, at the thickness of 90 nm radiative (non-radiative) decay rates are suppressed (enhanced), whereas at 160 nm film thickness the situation is reversed. Figs. 3.7 (b) and 3.7 (c) present the simulation results of single ND on diamond film in terms of the energy absorption rate in various diamond film thickness by an NV centre with its electric dipole moment oriented parallel to the substrate. Evidently, for an ND on 90 nm thick diamond film the overall energy absorption rate is higher than an ND on 160 nm thick diamond film and the areas featuring high absorption are seen to extend further along with the film and into Si substrate. Consequently, higher absorption should lead to a stronger reduction of emission.This is illustrated in radiated field maps plotted in Figs. 3.7 (d) and 3.7 (e) for the film thickness of 90 nm and 160 nm, respectively. The modelled dependence of the radiative decay rate on the film thickness can be fitted with a sine function: $k + l\sin(\omega x + m)$, as shown in Fig. 3.7 (a). From the fitting parameters, I obtain the period of the sine function, $T^{\mathrm{rad}}_{\mathrm{diamond}} = \frac{2\pi}{\omega^{\mathrm{rad}}_{\mathrm{diamond}}}$ =126 nm, which is close to the thickness of a diamond film supporting the fundamental Fabry-Perot mode at λ=575nm: $T^{\mathrm{FP}}_{\mathrm{diamond}} = \frac{575\ \mathrm{nm}}{2n_{\mathrm{diamond}}}$ = 120 nm. I, therefore, conclude that the decay rate can be efficiently controlled by changing the thickness of the supporting thin film. In particular, the tuning depth of NV radiative decay rate for a thin diamond film can be as high as $\frac{2l^{\mathrm{rad}}_{\mathrm{diamond}}}{k^{\mathrm{rad}}_{\mathrm{diamond}}}$ = 89%, where $l^{\mathrm{rad}}_{\mathrm{diamond}}$ and $k^{\mathrm{rad}}_{\mathrm{diamond}}$ are the fitting parameters of the sine function. Finally, I argue that in our study the average lifetime is largely independent of the inhomogeneity in the substrate and immediate dielectric environment, as well as NV emitter position and orientation of its electric dipole moment. Indeed, the large number of NV emitters per particle yields a Purcell factor effectively averaged over different positions and dipole orientations of the emitters in NDs. Furthermore, my measurements involved clusters of different sizes and aspect ratios with no strong correlation observed between the cluster size/shape and decay rate (see Fig. 3.11).

Table 3.4. Experimentally measured ($\overline{\tau}_{Exp}$) and numerically simulated (τ_{Sim}) NV center lifetimes on the diamond film and the bare silicon substrate. Experimental values correspond to the average of the distribution.

Substrates	$\overline{\tau}_{Exp}(ns)$	$\overline{\tau}_{Sim}(ns)$
Si	30	91.49
Diamond	17	81.73

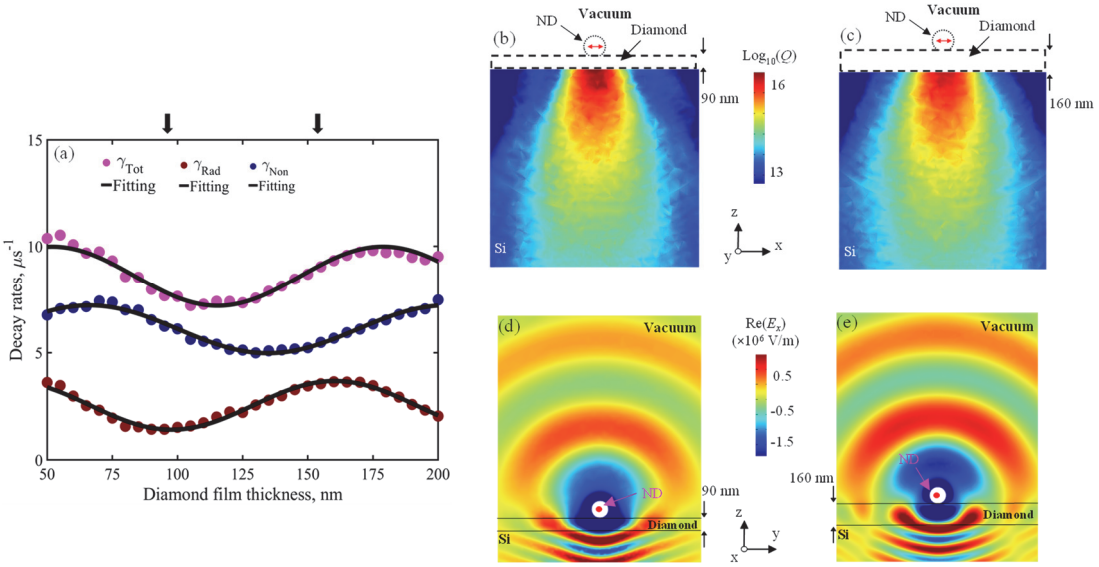

Figure 3.7. Modulating decay rate of NV centres by changing diamond film thickness. (a) Modelled decay rates of an NV center on a diamond film as a function of the film thickness. The electric dipole moment of the emitter is oriented parallel to the plane of the substrate. The solid line corresponds to a sine function fit to the numerically calculated decay rates (solid circles). (b-c) Simulated distribution of absorption in *xz*-plane presented in terms of heat, *Q*, dissipated Si substrates with diamond film thickness are 90 nm and 160 nm, respectively. (d-e) The real part of x-component of the electric field emitted in zy-plane by an NV center of a ND sitting on a diamond film with a thickness of 90 nm and 160 nm, respectively (the electric dipole moment of the NV center is oriented along x-axis).

To further demonstrate the coupling between the NV centres and the dielectric thin film cavities, I have numerically studied a single ND on a 100 nm thick Si_3N_4 membrane which is lossless at the wavelength of 575 nm. Due to there is no loss in this system, so all the radiation decay in the radiative channel. Fig. 3.8 shows an illustration of a single ND on Si_3N_4 membrane. In this Si_3N_4 nanofilm cavities, I also observe a substantial modulation of the radiative decay rates as a function of film thickness indicating the presence of a slab mode in the Si_3N_4 membrane as shown in Fig 3.9(a). The dependence of decay rate on the Si_3N_4 membrane thickness is also fitted with a sinusoidal function: $k + lsin(\omega x + m)$. The fitting parameters are $k_{Si_3N_4} = 13.87\ ns^{-1}$, $l_{Si_3N_4}$=2.60 ns^{-1}, $m_{Si_3N_4}$=3.69, $\omega_{Si_3N_4}$=0.04 nm^{-1}. From the fitting parameters, we can obtain the periods of the sine functions are $T_{Si_3N_4} = \frac{2\pi}{\omega_{Si_3N_4}}$ =157nm, which are close to the periods of Fabry-Perot modes of Si_3N_4 membrane and diamond film at 575nm: $T^{FP}_{Si_3N_4} = \frac{575nm}{2n_{Si_3N_4}}$ =140.39nm. The periods of the sine functions match with the periods of Fabry-Perot modes, which verifies that ND is coupled with the modes of the Si_3N_4 membrane cavities. the modulation depth is $\frac{2l_{Si_3N_4}}{k_{Si_3N_4}}$ = 37.49%. The radiated field maps plotted in Figs. 3.9 (b) and (c) for the film thickness of 50 nm and 125 nm, respectively. I can observe there is stronger radiation to the far-field when the film thickness is 125 nm.

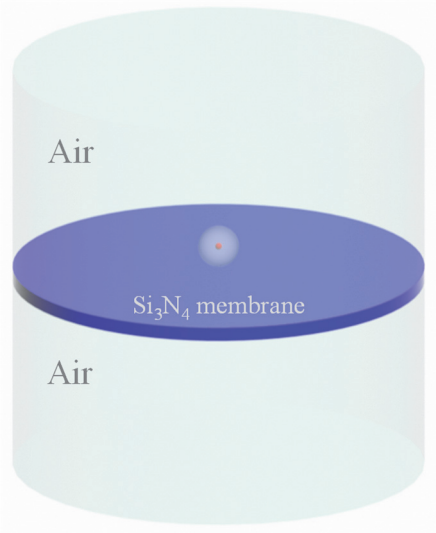

Figure 3.8. Ilustration of a single ND on Si_3N_4 membrane.

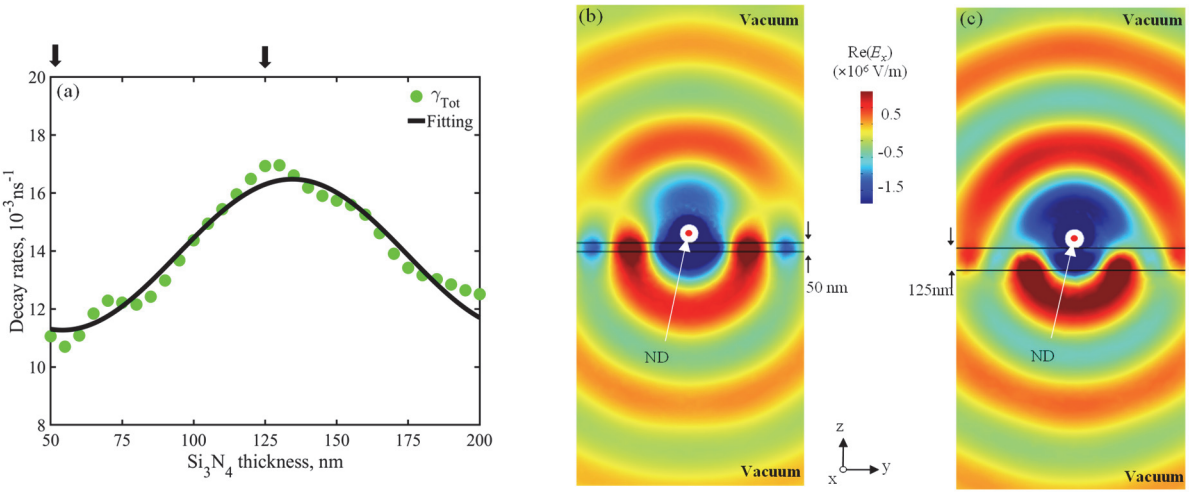

Figure 3.9. Modulating decay rate of NV centres by changing Si_3N_4 membrane thickness. (a) Decay rates of NV^0 center emitters on Si_3N_4 membrane cavity as a function of Si_3N_4 membrane thickness. The emitter is oriented in the plane of the substrate. Solid lines correspond to sinusoidal fits to the numerically calculated decay rates (solid circles). (b-c) The real part of x-component of the electric field emitted in zy-plane by an NV center of a ND sitting on Si_3N_4 membrane with a thickness of 50 nm and 125 nm, respectively (the electric dipole moment of the NV center is oriented along x-axis).

3.6 Nanodiamond cluster size and aspect ratio distributions

The ND clusters measured in the experiment have different sizes and aspect ratios. Fig. 3.10 (a-b) show the size and aspect ratio distributions of NDs clusters on Si and diamond. There are different size and aspect ratio distributions on these two substrates, the average size of NDs clusters on the silicon is about 2 times of NDs clusters on the diamond, moreover, more NDs clusters on the diamond have the aspect ratio close to '1' than on the NDs clusters on the silicon.

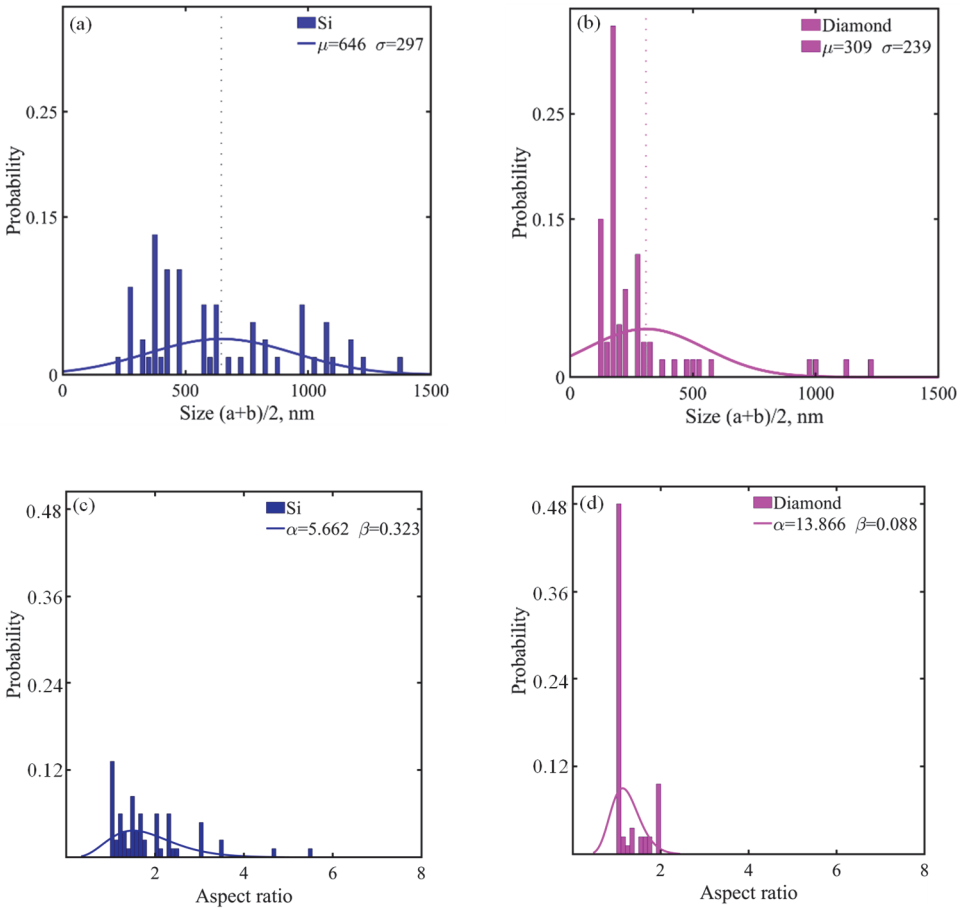

Figure 3.10**.** Size distributions of NDs clusters on silicon (a) and diamond thin film cavity (b). The histograms are obtained from measurements of 60 different ND clusters on each substrate and are fitted by a Gaussian distribution, where μ is the mean (dotted vertical lines) and σ is the standard deviation (in nm). Aspect ratio distributions of NDs clusters on silicon (c) and diamond thin film cavity (d). The histograms are fitted by a gamma distribution in (c) and (d), where **α** is the mean and **β** is the standard deviation.

To rule out the factor that NDs clusters with different sizes and aspect ratio maybe influence the NV centre lifetimes. The correlations between the recorded lifetimes and ND cluster geometry are examined in Fig. 3.11 for diamonds nanoparticles placed on the diamond film and bare Si substrate, where the decay rates are presented as functions of size (Fig. 3.11 a) and shape (Fig. 3.11 b). In both cases, the decay rates are nearly independent of ND cluster size and cluster aspect ratio. I can conclude that the NDs sizes and aspect ratios would not influence the NV centre lifetimes in this experiment.

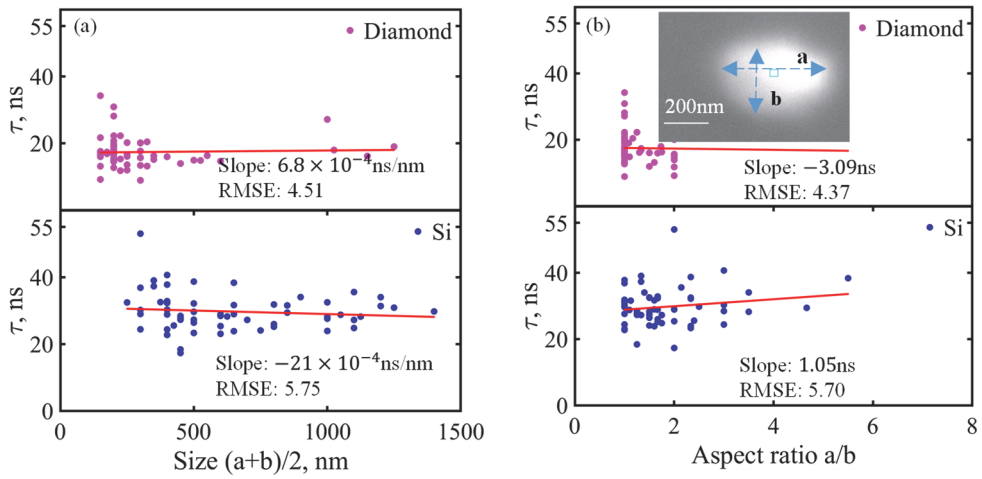

Figure 3.11. Experimentally measured NV center lifetime vs cluster size (a) and aspect ratio (b) for diamond nanoparticles deposited on a diamond thin film (top) or a silicon substrate (b). The correlation between lifetime and cluster size and aspect ratio is quantified by the slope and RMSE as obtained by a least-squares fit. The cluster size and aspect ratio are calculated as $(a+b)/2$ and a/b, respectively, where a (b) is the length of the cluster longer (shorter) (see inset to fig. 3.11 (b)).

3.7 Summary

In summary, I have demonstrated by TR-CL experiments and finite element calculations that even a thin dielectric diamond thin film is sufficient to tune radiative decay rate by ~90% (~40% by employing Si_3N_4 membrane). In particular, I experimentally demonstrate a two-fold enhancement of the decay rate of NV^0 centers in NDs when deposited on a thin diamond film as opposed to a thick Si substrate. Given that the decay rates of NV center emitters are distributed, I measure large ensembles of ND clusters and compare the emission statistics for the two substrates and observe shifts of the full distribution of decay rates towards shorter lifetimes, in the case of the diamond substrate. Moreover, by analyzing the spectral characteristics of NV centres, I observed the ZPL distributions have a relatively larger difference between Si and diamond substrate which is in contrast to the PSB distributions. Furthermore, my measurements indicate the absence of correlations between the NV lifetimes and the geometrical characteristics of the ND clusters, thus the observed decay rate enhancement cannot be attributed to such factors. Numerical modelling, on the other hand, indicates strong interactions between the substrate and the NDs through the excitation of optical slab modes in the film, which in turn leads to a strong dependence of the radiative and non-radiative decay rates on the film thickness. Thus, my results provide insights into the mechanism of decay rate enhancement of NV emission from NDs deposited on thin films and puts forward simple means of controlling the corresponding emission statistics.

Chapter 4

Controlling nitrogen vacancy centre lifetime with chalcogenide films

4.1 Introduction

Controlling emission can be considered one of the most important objectives of current photonics research as it will probably lead to important and dramatic advances in device performance [153]. Chalcogenides were selected as they provide very good opportunities for static and dynamic tuning of the emission properties of NV centres in nanodiamond. Particularly, the dielectric properties of chalcogenides can be statically tuned by composition control. Usually, dynamic control can be achieved through thermal [154], optical [155] and electrical [156] methods. Recently, Qu et al. utilized a metal-insulator-metal architecture incorporating a 350-nm-thick chalcogenide phase change material (PCM) layer to dynamically manipulate the thermal emission with zero-static power [157]. More recently, multispectral thermal emission using a PCM-plasmonic metasurface in the mid-IR wavelength range (2 – 3 μm) was studied [158]. Local strain due to volume expansion of a GeSbTe (GST) upon amorphization has been proposed to precisely control the emission energy of semiconductor quantum dots (QDs) on which a GST thin film is deposited [159, 160]. There is a red-shift of the photoluminescence (PL) peak of quantum dots (QDs) on amorphous GST, which can be recovered by recrystallization with laser annealing. Two closely located QDs can be tuned to the same energy by controlling the direction and magnitude of the peak shift through the precisely adjustment of the position and size of an indenter which formed by a thin layer GST through amorphization from a crystalline phase [161].

The real-life applications of NV centres in NDs have been difficult because of the broad distribution of their lifetimes. The broadening results from strong variations of both radiative and nonradiative decay rates, and quantum efficiency of NV centres [162], which in practice are controlled by many factors, such as crystal strain [162], contamination during fabrication [39], coupling to Mie resonance of NDs [40, 41], locations and orientations of NV centres within NDs [163, 164], and the presence of large ensembles of NV centres in NDs [108]. I believe the situation here can be improved by employing chalcogenides. Chalcogenides are compound materials based on one or more of the chalcogen elements from group 6a of the periodic table (sulphur, selenium and tellurium, but excluding oxygen), covalently bonded to network formers such as As, Ge, Sb, Ga, Si or P [165]. They provide strong responses to optical, electrical and thermal stimuli controlled by material stoichiometry and phase (amorphous or crystalline). Their composition can be tuned to make the permittivity exhibits dielectric,

plasmonic or even epsilon-near-zero (ENZ) response in the visible range [117, 122]. A variety of chalcogenide phase-change active plasmonic and photonic devices have been numerically and experimentally demonstrated, such as optically reconfigurable metasurface [155], fiber-integrated phase-change reconfigurable optical attenuator [166], near-infrared rewritable, non-volatile subwavelength absorber [167], bidirectional switch [168], etc.

In this chapter, In this chapter, I have demonstrated that the permittivity of chalcogenides can be statically changed in the range of -24 to +13 for the real part and 10 to 35 for the imaginary part. I report that the statistics of the decay rates of NV centres can be efficiently controlled by changing the immediate dielectric environment of NDs with variable compositional chacogenide films. I demonstrate this experimentally by characterising the lifetime distribution for large ensembles of NV centres in NDs embedded in thin chalcogenide films with the optical constants tuned continuously from plasmonic to lossy dielectric. My analysis indicates that the distribution of lifetimes can become narrower by over five times, featuring a spread of 1 ns around the average lifetime of 11 ns. Aside from exploring structural phase transitions as a means for dynamic emission control, using high-throughput physical vapor deposition and characterization techniques, I have explored the effect of stoichiometric variation of the dielectric and plasmonic characteristics of the host chalcogenide on the emission of the embedded NDs.

4.2 Sample Description

Antimony telluride (SbTe) is a binary chalcogenide alloy as a narrow-gap semiconductor with phase-change properties [169], thermoelectric properties [170, 171], and can be a 3D electrical topological insulator [172, 173]. SbTe has been applied in filling nanohole arrays and ultraviolet hollow-core waveguides cladding recently due to it can have low-epsilon optical properties [174, 175]. In my experiment, I have study the behaviour of NV centres in NDs embedded in SbTe film. Deposition of chalcogenides was performed by my colleague Dr Davide Piccinotti. NDs were embedded in SbTe using the following procedure. First, a thin film of SbTe of varying composition and ranging in thickness, $d/2$, from 20 to 50 nm were deposited over a 28 mm × 28 mm large area of silicon (Si) substrate using a high-throughput physics vapour deposition system. The obtained SbTe film was then coated via drop casting with a dispersion of NDs, which was prepared by diluting NDs in methanol and mixing the solution for 10 min in an ultrasonic bath. After methanol evaporated, a second SbTe film (with thickness $d/2$) was deposited over the first SbTe film using the same procedure as above, which yielded an SbTe film with overall thickness d incorporating NDs. Figure 4.1 (a) shows a fragment of the sample featuring ND clusters covered by SbTe. As a reference, I also prepared a sample containing exposed NDs, where the dispersion of NDs was applied onto an SbTe film of thickness d, i.e. after the second round of the deposition. All samples were vacuum sealed immediately upon production, and also between characterisation measurements.

The complex permittivity of the synthesized SbTe films was a strong function of composition. It was measured using variable angle spectroscopic ellipsometer J. A. Woollam M2000 with an

automated stage programmed to sample a 10×10 point array within the central 19 mm × 19 mm region (point-to-point separation 2.1 mm). Figures 4.1(c) and 4.1(d) show the real, Re(ε) and imaginary, Im(ε), parts of SbTe permittivity mapped across the samples at a wavelength of 575 nm (which corresponds to the zero phonon line of NV^0 centres). Re(ε) is seen to vary from –23 to 13 crossing zero for a wide range of compositions. Im (ε) remains fairly high for all compositions, in the range 15 – 30. To more clearly show how the loss of the SbTe depends on the position in the film, the real and imaginary of refractive index ($n = Re(\sqrt{\varepsilon}), k = Im(\sqrt{\varepsilon})$) of SbTe were shown at the same wavelength in Fig. 4.1(e) and 4.1(f), respectively. In which, n is seen to vary from 1.5 to 5 and k always remains high value , in the range 2.5 – 6, which means the SbTe film in the whole domain has high loss. Variation in the thickness of the obtained SbTe films is also inherent to the process of synthesizing films from two off-axis sources with wedge shutters [118, 119]. The thickness was measured using a stylus profilometer along the external edges of the film and then interpolated across the central area. Figure 4.1(b) reveals that the thickness of SbTe films, *d*, obtained after two rounds of deposition varied across the samples from about 40 to 100 nm.

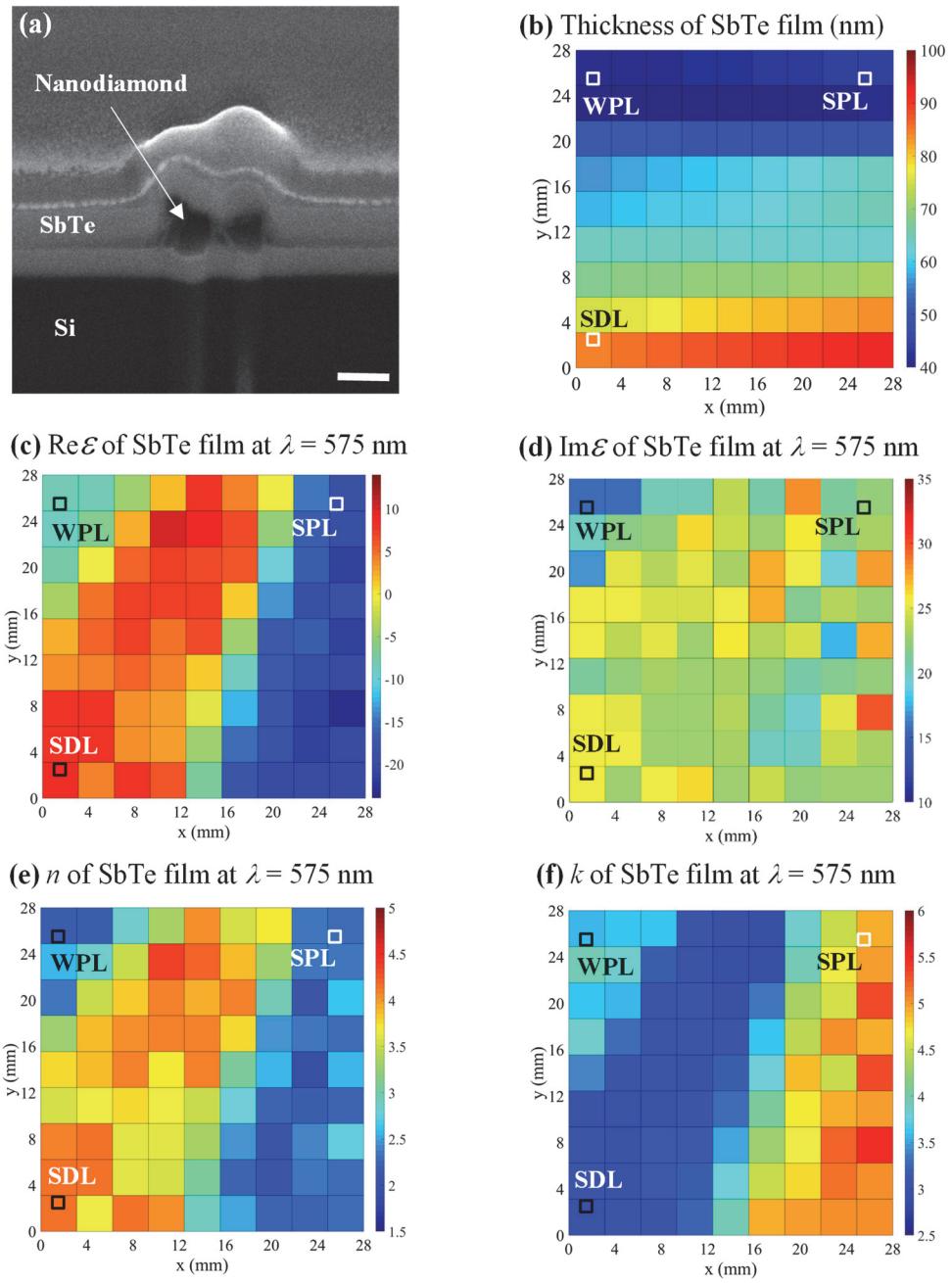

Figure 4. 1. NDs embedded in SbTe film sample descriptions. (a) SEM image of nanodiamonds embedded in SbTe films. The scale bar is $2\mu m$. Image taken by Dr. Jinkyu So. (b) Map of the thickness of SbTe films. (c) & (d) Real and imaginary parts of the permittivity, (e) & (f) real and imaginary parts of the refractive index of SbTe films mapped at the wavelength of 575 nm. Squares mark the areas of the samples where the lifetime statistics of nitrogen-vacancy centres were collected. WPL: weak plasmonic; SPL: strong plasmonic; SDL: strong dielectric.

4.3 Lifetime and brightness of nitrogen vacancy centres in nanodiamonds embedded in SbTe

The lifetime of NV^0 centres was characterized in three distinct areas of SbTe films, which are marked in Fig. 4.1(b)-4.1(f) by squares. They all had similar imaginary parts of the permittivity (at the level of ~20) and exhibited strong plasmonic response (SPL) with $\mathrm{Re}(\varepsilon) = -15$, weak plasmonic response (WPL) with $\mathrm{Re}(\varepsilon) = -7$ and strong dielectric response (SDL) with $\mathrm{Re}(\varepsilon) = 7$, respectively. For each area, we selected a total of 15 ND clusters. The results of my measurements are summarized in Fig. 4.2(a) in the form of boxplots. Evidently, the reference sample featuring NDs on top of SbTe film displays a large variation of the lifetimes for all three areas with the spread exceeding 7 ns and the average lifetime of NV^0 centres nearing 20 ns, which is consistent with the data reported in the previous studies [108]. At the same time, the average lifetimes of NV^0 centres in NDs incorporated by SbTe film are seen to become a factor of two shorter, converging at 11 ns for all three areas. More intriguingly, the spread of the lifetimes for this sample is reduced dramatically and becomes ~1 ns in SPL and WPL areas, and ~2 ns in SDL area. Similar variations are observed in figure 4.2(b) for the distributions of brightness of NV^0 centres, which we also characterised during TR-CL measurements. More specifically, the brightness data exhibit a wide spread for NDs placed on top of an SbTe film regardless of the local dielectric response of the film, but the spread becomes a factor of three narrower (at least) for NDs incorporated into SbTe film. The average brightness of NV^0 centres appears to also decrease, by about five times, for NDs imbedded in an SbTe film, which is consistent with the decrease of their average lifetime revealed by figure 4.2(a). To quantitative observe the variation of lifetime and brightness of NV^0 centres in NDs, the histogram of lifetime and brightness were fitted by a Gaussian distributions as shown in Fig. 4.3(a-f), from which I get the means and standard deviations of the distribution. The standard deviation of the lifetimes for this sample is ~1 ns in SPL and WPL areas, and ~2 ns in SDL area, and the mean of the lifetimes for this sample is ~11 ns in SPL, WPL, SDL areas. The standard deviation of the brightness for this sample is ~500 counts/s in SPL area, ~200 counts/s in WPL area, and ~800 ns in SDL area (narrowed 3~12 times compared with NDs on SbTe), and the mean of the lifetimes for this sample is ~1200 counts/s in SPL area, ~1600 counts/s in WPL area, and ~1400 counts in SDL area (reduced 3~4 times compared with NDs on SbTe).

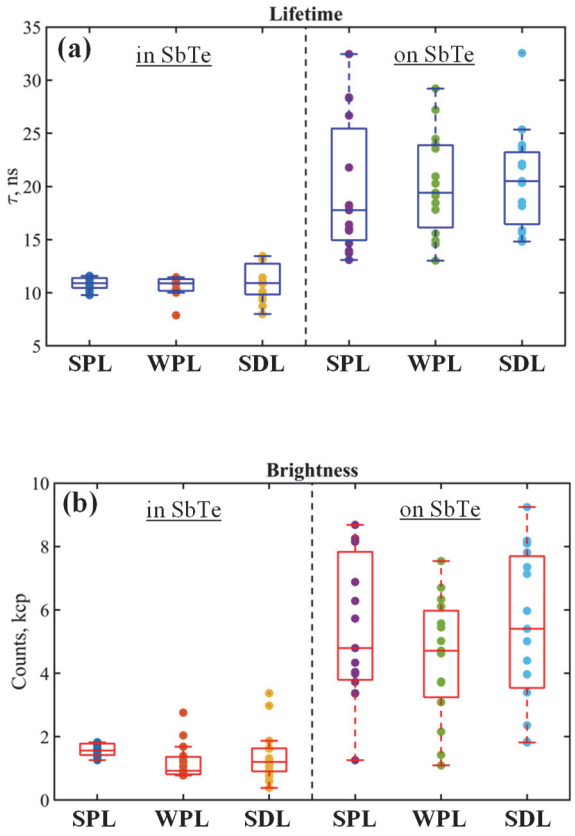

Figure 4. 2. Boxplot of NV centres lifetime and brightness distributions.(a) Boxplot of the distribution of lifetimes extracted from time-correlated histograms in areas of SbTe films with SPL (strong plasmonic), WPL (weak plasmonic) and SDL (strong dielectric) response, as marked in figures 1(b)-1(f). (b) The brightness of emission from nanodiamonds corresponding to lifetime data in (a), kcp is kilo count per second. On each box, the central mark indicates the median, and the bottom and top edges of the box indicate the 25th and 75th percentiles, respectively. The whiskers extend to the most extreme data points not considered outliers. The points represent the experimental data.

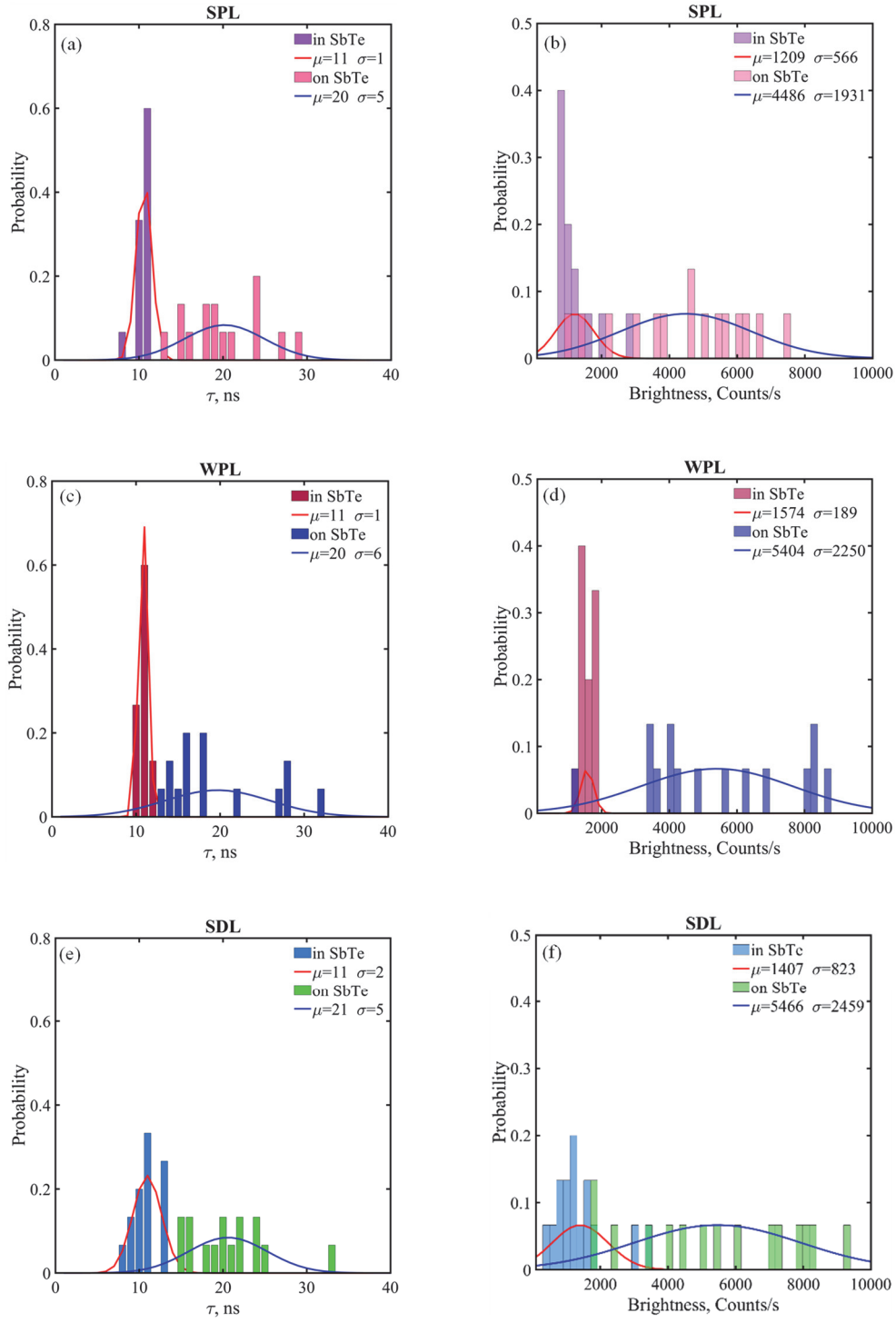

Figure 4. 3. Gaussian distributions of NV centres lifetime and brightness. (a) (c) (e) Lifetime distributions of NV^0 centers in diamond nanoparticles on top of and embedded in areas of SbTe films with SPL (strong plasmonic), WPL (weak plasmonic) and SDL (strong dielectric) response. The histograms are obtained from measurements of 15 different ND clusters in each area and are fitted by a Gaussian distribution, where μ is the mean and σ is the standard deviation (in ns). (b) (d) (f) Brightness distributions of NV^0 centers in diamond nanoparticles on top of and embedded in areas of SbTe films with SPL, WPL and SDL response. The histograms are obtained from measurements of 15 different ND clusters in each area and are fitted by a Gaussian distribution, where μ is the mean and σ is the standard deviation (in Counts/s).

4.4 Spectral characteristics of nitrogen vacancy centres in nanodiamonds embedded in SbTe

The spectrum of NV^0 centres was also characterized in these three distinct areas of SbTe films, which are marked in Fig. 4.1(b)-4.1(f) by squares. The spectrum fitting procedures were described in methods in chapter 2. The phonon side band (PSB) amplitude correlates with the brightness distribution which was discussed in section 4.3. The distribution of fitting parameters of PSB are shown in Fig. 4.4 (a-f). One can see that the PSB centre frequencies of NV^0 centres in the NDs embedded in SbTe film are red-shifted compared to those of NDs on the SbTe film, while the spread of their distribution exhibits a two-fold decrease. The NDs embedded in SbTe film suffer more external strain effect due to they have larger contact areas with the SbTe maybe leads to the PSB centre frequency red shift and spread becomes narrower. I also can observe that the average and the spread of the PSB centre frequency distributions show no dependence on the permittivity of the SbTe film, which means the strain effect of NDs has little to do with the dielectric environment. Different with the change of PSB centre frequency distributions when NDs embedded in SbTe film, the distributions of PSB linewidths of NDs almostly keep the same regardless of the permittivity of SbTe film and the location of NDs (i.e., in or on SbTe film). The PSB linewidths usually are temperature dependent which is always keep the same, while the strain and dielectric environment have little influence on them, which makes their distributions are largely similar not matter how the NDs are located.

Unlike PSB, which depends on the temperature of the environment during measurements, zero phonon line (ZPL) reflects spectral characteristics of NV^0 centres more directly. The distribution of fitting parameters of ZPL are shown in Fig. 4.5 (a-i). Here the ZPL amplitude is seen to decrease 4~9 times for NDs embedded in SbTe film, and similar times of decrease is also observed for the spread of the distribution, while it shows no dependence on the SbTe film permittivity, (see Fig. 4.5 (a), (d), (e)). The ZPL amplitude is correlated with the brightness of NV^0 centre in NDs, their distributions are in accordance with the brightness distributions in Fig. 4.3. In contrast to the distribution of PSB centre frequency, the distribution of ZPL centre frequency exhibits no dependence on how NDs are placed (i.e., in or on SbTe film), as shown in Fig. 4.5 (b), (e). Unlike PSB centre frequency which depends on the external strain from the surrounding environment, ZPL centre frequency only depends on the internal strain from the NDs themselves, which makes the distributions depends less on how NDs are located. Similar to the PSB linewidth distributions, the ZPL linewidth distributions also largely keep the same no matter how the NDs are placed (see Fig. 4.4(c),(f)), which are due to the ZPL linewidth also only related to the environment temperatures. Both the distributions of ZPL centre frequency and ZPL linewidth depends on how NDs are placed when NDs are in the areas of SbTe with a strong dielectric response (see Fig. 4.4(h), (i)), which can be attributed to the fact that the dielectric SbTe film has weak heat conductivity.

By comparing the distributions of PSB and ZPL NV^0 centre, I can observe that the ZPL shows stronger dependence on the surrounding environmental conditions, such as external strain, temperature, conductivity, etc. Yet, the spectral characteristics of NV centres in NDs embedded in SbTe film do not depend on the dielectric properties of SbTe film, while the lifetime statistics

do. To understand this, I simulated how the emission characteristics of NV^0 centres depends on the dielectric environment in the next section.

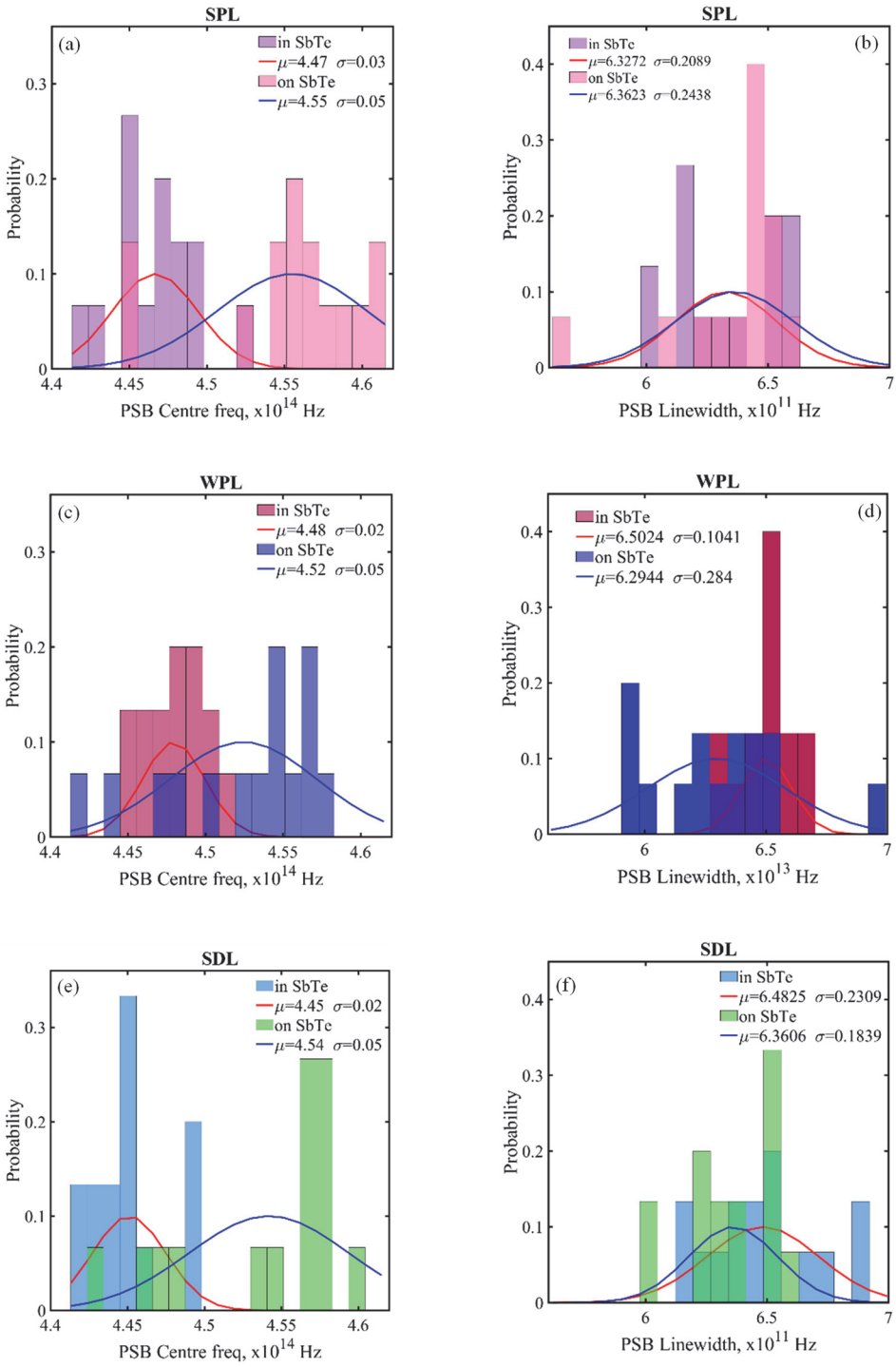

Figure 4. 4. Phonon sideband (PSB) fitting results of NV centres embedded in SbTe film. (a) (c) (e) PSB centre frequency distributions of NV^0 centers in diamond nanoparticles on top of and embedded in areas of SbTe films with SPL (strong plasmonic), WPL (weak plasmonic) and SDL (strong dielectric) response. The histograms are obtained from measurements of 15 different ND clusters in each area and are fitted by a Gaussian distribution, where μ is the mean and σ is the standard deviation (in $\times 10^{14}$ Hz). (b) (d) (f) PSB linewidth of NV^0 centers in diamond nanoparticles on top of and embedded in areas of SbTe films with SPL, WPL and SDL response. The histograms are obtained from measurements of 15 different ND clusters in each area and are fitted by a Gaussian distribution, where μ is the mean and σ is the standard deviation (in $\times 10^{11}$ Hz).

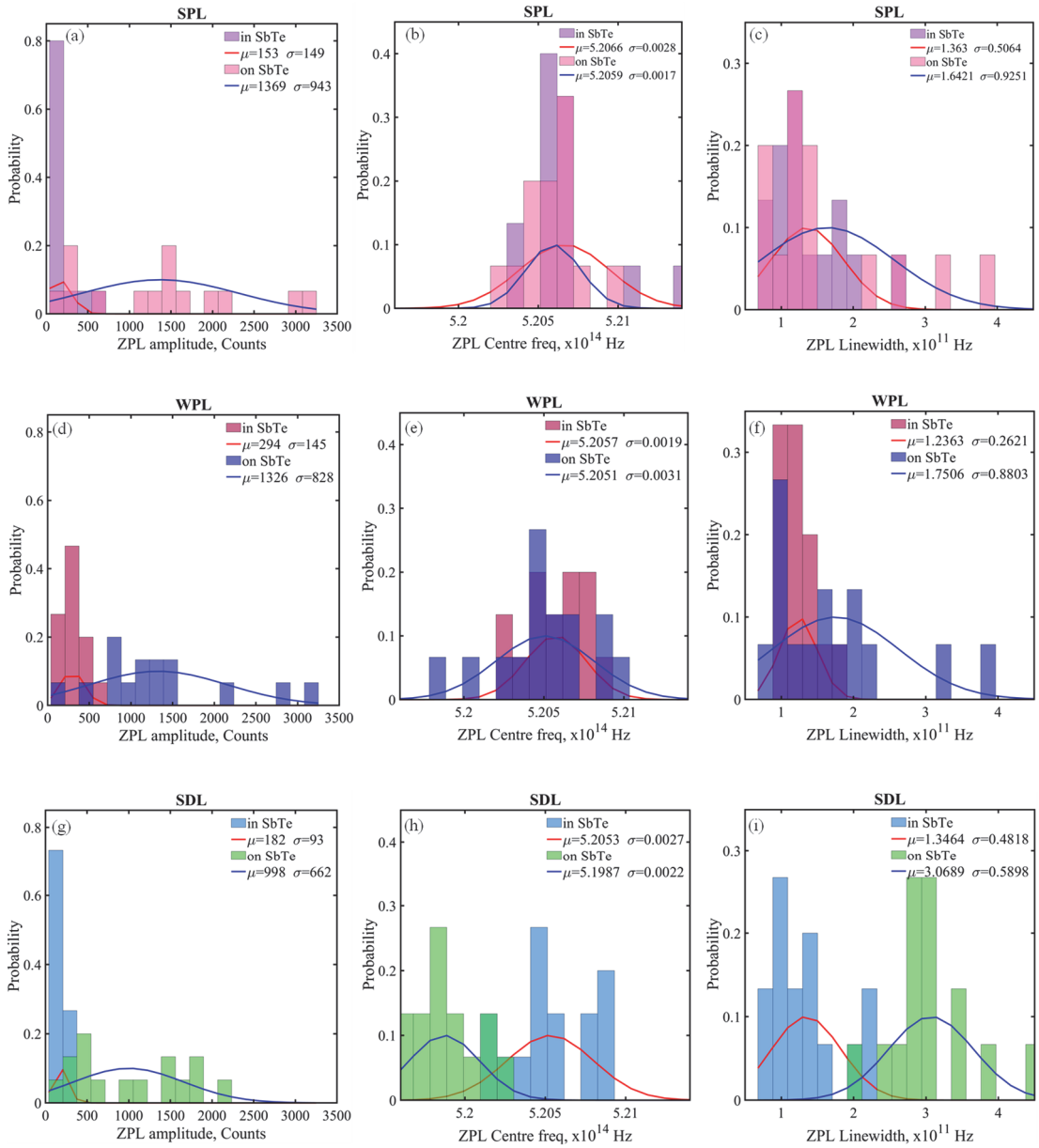

Figure 4. 5. Zero-phonon line (ZPL) fitting results of NV centres embedded in SbTe film (a) (d) (g) ZPLamplitude distributions of NV^0 centers in diamond nanoparticles on top of and embedded in areas of SbTe films with SPL (strong plasmonic), WPL (weak plasmonic) and SDL (strong dielectric) response. The histograms are obtained from measurements of 15 different ND clusters in each area and are fitted by a Gaussian distribution, where μ is the mean and σ is the standard deviation (in counts). (b) (e) (h) ZPL centre frequency distributions of NV^0 centers in diamond nanoparticles on top of and embedded in areas of SbTe films with SPL, WPL and SDL response. The histograms are obtained from measurements of 15 different ND clusters in each area and are fitted by a Gaussian distribution, where μ is the mean and σ is the standard deviation (in $\times 10^{14}$ Hz). (c) (f) (i) ZPL linewidth of NV^0 centers in diamond nanoparticles on top of and embedded in areas of SbTe films with SPL, WPL and SDL response. The histograms are obtained from measurements of 15 different ND clusters in each area and are fitted by a Gaussian distribution, where μ is the mean and σ is the standard deviation (in $\times 10^{11}$ Hz).

4.5 Simulation

To understand the mechanisms responsible for how the lifetime statistics depends on the dielectric properties of SbTe film. I modelled the emission of an isolated 120 nm large ND containing a single NV centre with its electric dipole moment oriented parallel and orthogonal to the substrate. The schematic of my model is shown in figure 4.6, in which the embedded of a single ND is modelled by a thickness d SbTe cap enclosed the ND particle. The simulation details have been described in detail in Chapter 2, section 2.4.2.

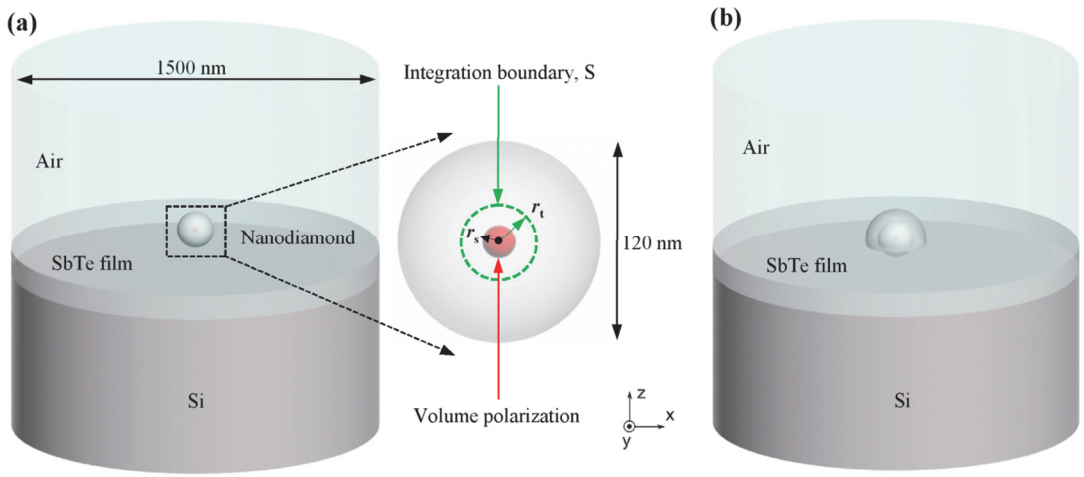

Figure 4. 6. A schematic of the simulation domain used for modelling the emission of a ND containing a single NV centre, when the ND was placed on an SbTe film (a) and embedded in an SbTe film (b). The NV^0 center is introduced as a volume polarization density with the orientation along the x-axis (parallel) or z-axis (perpendicular) oscillating inside a sphere of radius r_s =5 nm. The total radiated power is calculated as the surface integral of power flow $\vec{P}$ through a spherical surface $\vec{S}$ of radius r_t =6 nm encapsulating the emitting dipole, which is situated entirely inside the ND with a radius of 60 nm.

I considered two cases, as studied in my experiments, namely (i) an ND sitting on an SbTe film and (ii) an ND embedded in an SbTe film. Each case included films with WPL, SPL and SDL response, which were placed on a semi-infinite Si substrate. Figure 4.7 presents the simulation results obtained for a lossy SbTe film featuring SDL response in terms of the energy absorption rate in various parts of the structure and electric field emitted into the vacuum by an NV centre with its electric dipole moment oriented parallel to the substrate. Evidently, for an ND embedded in an SbTe film the overall energy absorption rate is higher and the areas featuring high absorption are seen to extend further along with the film and into Si substrate (compare figures 4.7(a) and 4.7(b)). Consequently, higher absorption should lead to a stronger reduction of emission and that was exactly what I observed in our simulations (compare figures 4.7(c) and 4.7(d)). Similar differences in absorption and emission were observed for NDs on and in SbTe films featuring SPL and WPL response.

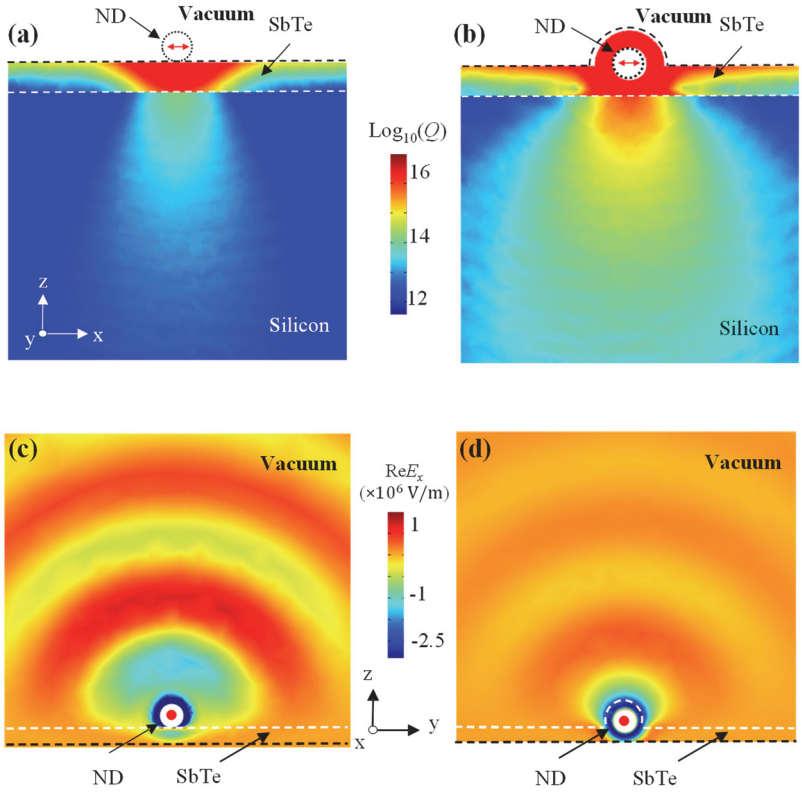

Figure 4. 7. (a) & (b) Simulated distribution of absorption in *xz*-plane presented in terms of heat, *Q*, dissipated in the Si substrate and the SbTe film with a nanodiamond placed, respectively, on and in the film. The SbTe film here was modelled as a strong lossy dielectric (SDL) with ε=7+20i The electric dipole moment of a nitrogen-vacancy centre inside the nanodiamond was oriented parallel to the *x*-axis, as shown by the red arrows. (c) & (d) Simulated distribution of the *x*-component of the electric field (real part) in the *yz*-plane emitted into the vacuum by the nitrogen-vacancy centre inside the nanodiamond placed, respectively, on and in SbTe film. The electric field is not plotted inside the nanodiamond.

4.6 Discussion

The simulated data enabled me to calculate the radiative and non-radiative decay rates for all possible configurations. The results are summarised and compared in table 4.1. For the electric dipole moment of an NV centre oriented perpendicular to the substrate the non-radiative decay rate, $\gamma_{\mathrm{non}}^{\perp}$, is about 4.5 times higher when an ND is embedded in an SbTe film (regardless of the type of SbTe properties). Expectedly, the radiative decay rate, $\gamma_{\mathrm{rad}}^{\perp}$, in this case is lower – by a factor of 2 for plasmonic SbTe films and by a factor of 9 for a strongly dielectric SbTe film. When the electric dipole moment is parallel to the substrate the situation is similar, though the differences in the decay rates, $\gamma_{\mathrm{non}}^{\parallel}$ and $\gamma_{\mathrm{rad}}^{\parallel}$, appear to be larger: $\gamma_{\mathrm{non}}^{\parallel}$ is > 18 times higher and $\gamma_{\mathrm{rad}}^{\parallel}$ is > 3 times lower for all three types of an SbTe film incorporating an ND. I further note that the ratio between the non-radiative and radiative decay rates does not exceed 2 for an ND sitting on an SbTe film, but raises above 9 for an ND imbedded in an SbTe film (approaching 174 when SbTe behaves as a strong dielectric and the electric dipole moment is parallel to the substrate). I analysis, therefore, indicates that the experimentally observed narrowing of the lifetime distribution was enforced by substantially increased non-radiative decay, which completely dominates the relaxation of NV centres in embedded NDs. The

enhancement of non-radiative decay should lead to shortening of the average lifetime and this is what I also observed in the experiment (see figure 4.2(a)).

The calculated data in table 4.1 also suggests that there is another mechanism responsible for changes in the lifetime statistics – an interplay between scattering and absorption of emitted photons. For an ND imbedded in an SbTe film, it renders the total decay rate, γ_{tot}, of an NV centre almost insensitive to the orientation of its electric dipole moment ($\gamma_{\mathrm{tot}}^{\perp}/\gamma_{\mathrm{tot}}^{\parallel} \sim 1$). Thus, if such an ND contains many NV centres (as our samples) this mechanism will efficiently negate the variation of lifetimes across an ND due to random orientations of the electric dipole moments [108]. On the contrary, for an ND sitting on an SbTe film the dependence of γ_{tot} on the electric dipole alignment remains quite strong ($\gamma_{\mathrm{tot}}^{\perp}/\gamma_{\mathrm{tot}}^{\parallel} > 3.5$) and, therefore, can only lead to further spreading of the lifetime distribution (especially when SbTe exhibits plasmonic response).

To have a better comparison between the decay rates of NV^0 centres in a single ND sitting on and embedded in SbTe film with different types of the material response (WPL, SPL and SDL)I plot a bar chart of simulated decay rates in Fig. 4.8 (a) (b). The nonradiative decay rate dominates the emission when NDs is embedded in SbTe film regardless of the orientations of the electric dipole, and both the nonradiative and radiative decay rates are kept similar values in these three areas, which means they do not depend on the permittivity of the SbTe film. Similar behavior can also be observed when ND are placed on top of the SbTe film. The decay rate depends less on the permittivity of the SbTe film, while the radiative decay has virtually the same rate as the nonradiative decay. My simulations agree very well with the experiment results.

Table 4.1. Calculated decay rates of a single NV centre interacting with thin SbTe films, which exhibit weak plasmonic (WPL), strong plasmonic (SPL) and strong dielectric (SDL) response.

	WPL (Re $\varepsilon = -7, d =$ 40nm)		SPL (Re $\varepsilon = -15, d =$ 40nm)		SDL (Re $\varepsilon = 7, d = 95$nm)	
Decay rates	on SbTe	in SbTe	on SbTe	in SbTe	on SbTe	in SbTe
$\gamma_{\mathrm{tot}}^{\parallel}(\mu s^{-1})$	8.97	102.79	8.38	114.36	8.64	88.96
$\gamma_{\mathrm{tot}}^{\perp}(\mu s^{-1})$	36.21	99.58	37.64	103.99	31.47	90.30
$\gamma_{\mathrm{non}}^{\parallel}(\mu s^{-1})$	4.05	101.16	3.12	112.87	4.86	88.45
$\gamma_{\mathrm{non}}^{\perp}(\mu s^{-1})$	20.13	90.97	17.25	93.74	20.07	89.01
$\gamma_{\mathrm{rad}}^{\parallel}(\mu s^{-1})$	4.91	1.62	5.26	1.49	3.78	0.51
$\gamma_{\mathrm{rad}}^{\perp}(\mu s^{-1})$	16.08	8.61	20.39	10.25	11.40	1.28
$\gamma_{\mathrm{non}}^{\parallel}/\gamma_{\mathrm{rad}}^{\parallel}$	0.83	62.29	0.59	75.78	1.29	173.63
$\gamma_{\mathrm{non}}^{\perp}/\gamma_{\mathrm{rad}}^{\perp}$	1.25	10.57	0.85	9.14	1.76	69.42

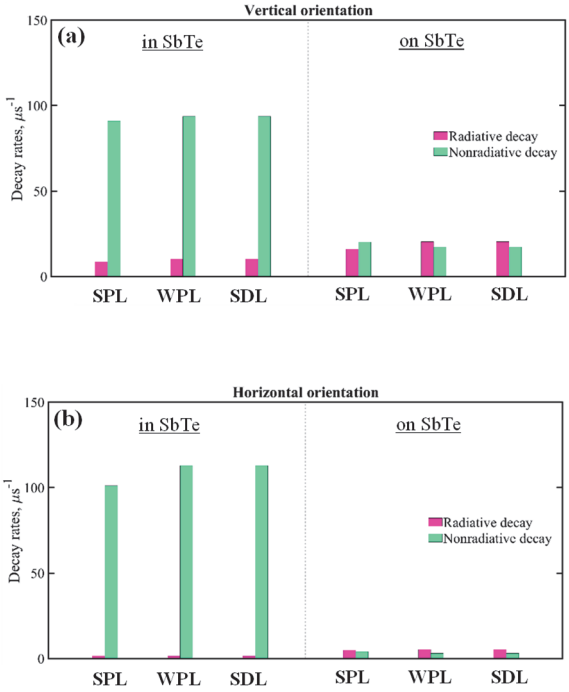

Figure 4. 8. (a) & (b) The calculated decay rates of NV centre in single nanodiamond nanoparticles on top of and embedded in areas of SbTe films with SPL (strong plasmonic), WPL (weak plasmonic) and SDL (strong dielectric) response when the NV centre orientations are vertical and horizontal to the interfaces respectively. The red bar represents radiative decay rates, the green bar represents nonradiative decay rates.

4.7 Summary

In summary, I have experimentally demonstrated that embedding NDs with multipole NV centres in thin chalcogenide films enabled me to dramatically narrow the distribution of the decay rates and shorten the average lifetime of the fluorescent defects. Also, I have analyzed the spectral characteristics of NV centres in chalcogenide materials in detail and found that PSB centre frequency distribution exhibits a red shift and its spread becomes narrower when NDs embedded in SbTe film while PSB linewidth distribution remains almost the same. Unlike PSB, ZPL is less affected by the surrounding environmental conditions, such as external strain, temperature. Moreover, the spectral characteristics of NV centres in NDs embedded in SbTe film are independent of the dielectric properties of SbTe film. My numerical modelling has shown that the observed changes in the lifetime statistics, i.e., more than a five-fold reduction of the spread and a two-fold decrease of the average, are underpinned by two mechanisms. One of the mechanisms is dissipation in lossy chalcogenide films, which enhances non-radiative decay to the extent that it completely dominates radiative decay for NDs embedded in the films. While such a mechanism naturally reduces the brightness of a single NV centre, in practice the intensity of fluorescence (and, in our case, cathodoluminescence) can be maintained at a sufficient level in NDs containing many centres. The other mechanism corresponds to an interplay between scattering and absorption of emitted photons. For embedded NDs it renders the total decay rate of NV centres insensitive to the orientation of their electric dipole moments, which is random in large ensembles of the defects. Given that one can dial (via stoichiometric engineering) optical response of chalcogenides anywhere from strongly plasmonic to strongly dielectric [176], and also can vary the level of losses by switching (optically, electrically or thermally) between amorphous and crystalline phases [177-179], my approach also offers a straightforward way of implementing active control over the emission statistics in NDs.

Chapter 5

Identifying nanoscale objects through luminescence and artificial intelligence

5.1 Introduction

The first few chapter of the thesis deal with the problem of controlling cathodoluminescence (CL) by changing the environment of the emitter (by employing diamond nanofilms and chalcogenide films). This chapter in a sense deals with the inverse problem: Can we obtain information about the emitter and its environment (i.e. configuration of apertures) from CL. The results presented in Chapters 3&4 on the effects of the ambient dielectric environment to the decay rate statistics of NV centers in nanodiamonds (NDs) reveal a complex relation well beyond what is predicted by simple considerations (e.g. based on refractive index only) even for the cases that may appear trivial, e.g. emitters on thin films. The spectrum statistics of NV centres in NDs have also been presented in Chapters 3&4. The surrounding environmental conditions influence the emission spectrum statistics of the NV centres in NDs, for instance, both the zero phonon line (ZPL) and phonon side band (PSB) distributions have differences between Si and diamond substrate. PSB centre frequency distribution exhibits a red shift and its spread becomes narrower when NDs embedded in SbTe film while PSB linewidth distribution remains almost the same. However, the relation between the individual spectra and the corresponding nanoscale emitters is still unclear. Several reasons make it is hard to reveal the complex relations with conventional mathematical methods. Firstly, cathodoluminescence (CL) studied in Chapters 3&4 is emitted from multiple NV centres in NDs, the CL spectra is the collective behaviour of multiple NV centres, which influenced by nanodiamond intrinsic properties as discussed in Chapter 4. Secondly, NDs with NV centres have varied shapes and sizes even they are on the same substrate, which add another dimension of complexity. Thirdly, the sensitivity of CL spectra to the individual ND with similar dielectric environment is so weak that the spectrum diversity can not be observed. Therefore, how to discover the complex relation between nanoscale emitters and their corresponding spectrum, especially their CL spectrum, plays an important role in understanding the underlying machanisms of light matter interaction. Artificial intelligence (AI) compared with conventional mathematical methods can reveal complex, often untraceable, relationships between the nanostructures and their optical response. For example, supervised machine learning algorithms have been implemented to classify single versus multiple NV centres in NDs using sparse autocorrelation data [11]. AI has been used to investigate both optical far fields and near fields for the perfect optical chirality. A theoretical circular dichroism (CD) maximum was achieved with a corresponding experimental result of 82% obtained in the far field, in which the CL spectroscopy was applied to analyze the origin of this strong optical chirality [180]. Recently, artificial intelligence (AI) has attracted significant attention in the nanophotonics community [7, 9, 10, 181]. For instance AI has been

employed to approximate the light scattering of multilayer nanoparticles[115] and retrieve information about an object with a deep learning neural network trained on scattering events from a large set of known objects [10]. Neural networks can retrieve optical scattering spectra of nanoparticles several orders of magnitude faster than conventional simulation methods [115], beat the $\lambda/2$ diffraction limit of conventional optical microscopy several times over by recording the intensity pattern of coherent light scattered from the object into the far-field [10]. Moreover, artificial intelligence can be used to solve nanophotonic inverse design problems by using back propagation methods, e.g. analytical gradient. Finally, optical information storage schemes have been suggested based on training an artificial neural network on large amounts of experimental optical scattering spectra from photonic nanostructures, reaching data densities beyond the diffraction limit [182].

However, the majority of earlier works on retrieving information about nano-objects is based on the scattered by from the nanostructures. The emission patterns from objects can also be used to achieve sub-diffraction-limit imaging [183], requires using high-accuracy localization of photo-switchable fluorophores. Here, I show that artificial intelligence can reveal the links between the structural properties of nanoscale objects and their emission spectra. I propose that instead of the typically considered spatial patterns of emitted fields, the emission spectra can be used to identify nanostructures and their geometrical characteristics beyond the diffraction limit. Such approaches may be of great interest in implementing novel tagging schemes based that do not require imaging.

5.2 Schematic of far-field identification of nano-objects

To illustrate the concept of nanostructure identification through emission properties, I consider plasmonic nanostructures in the form of ensembles of subwavelength apertures in a plasmonic film. The emission spectra are measured by cathodoluminescence and analyzed by feed-forward networks. A schematic is presented in Fig. 5.1 (a). Here, I anticipate that the high k-vectors of plasmons in the nanostructures will imprint information about the nanostructure geometry to far-field emission spectra with small shape changes in the nanostructures leading to large far-field spectrum differences. To prove this idea, I consider apertures in a plasmonic film arranged in a 4x4 grid with 16 distinct sites. Each site may or may not accommodate a single hole, resulting in 2^{16} different configurations. I consider holes with a radius of 50 nm in a 50 nm thick gold film on a 100 nm silicon nitride (Si_3N_4) membrane. The centre-to-centre distance of neighbouring holes is 60 nm which results in a largest configuration size of 280 nm. Our numerical results show that changes in the configuration of the plasmonic apertures result in very different CL spectra as shown in Fig. 5.1 (b), which we attribute to the role of plasmonic excitations in the nanostructures.

The proposed scheme is demonstrated in the following way: (1) I construct a large dataset consisting of plasmonic aperture configurations and collect the corresponding emission spectra. (2) A part of the dataset is employed to train a feed-forward neural network. (3) The trained neural network is fed with emission spectra of “unseen” configurations and is asked to return

the corresponding configurations. In addition, I consider the inverse scenario, where the neural network function is to retrieve spectral characteristics (e.g. peak wavelength or even the full spectrum) from the geometry of the plasmonic apertures.

I first demonstrate the scheme numerically. Here emission spectra are calculated by the methods described in Chapter 2, while neural network details are given in the next section.

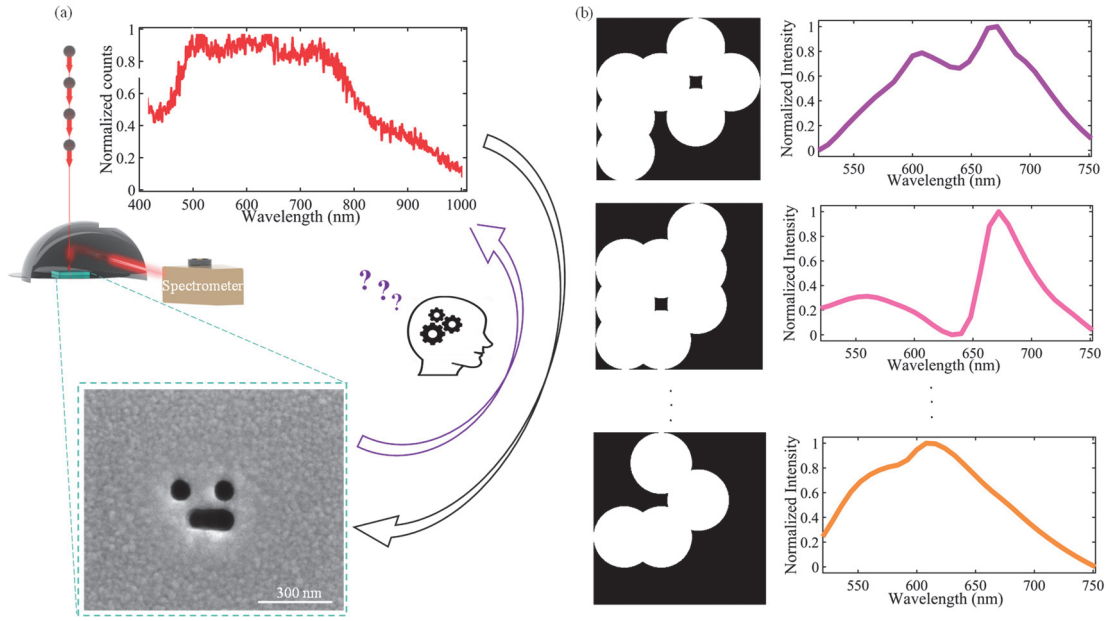

Figure 5. 1 Schematic of predicting CL spectra from subwavelength plasmonic apertures and vice versa. (a) CL system based on SEM. A parabolic mirror collects photons and facing to the spectrometer. Plasmonic aperture is shown in the SEM image (scale bar is 100nm). AI predicts CL spectra and AI predicts configuration. (b) Simulated CL spectra and corresponding plasmonic configurations for three characteristic cases.

However, the emission from dielectric environment with subwavelength apertures does not provide the such properties. To verify my idea, I simulated the emission properties of a vertical orientation emitter in dielectric environment with subwavelength nanostructures. Figure 5.2(a) shows the schematic of this model, all the parameters are the same with the model of subwavelength plasmonic simulation except that the gold film was replaced by a Titanium (Ti) film. The simulated normalized emission spectrum of different configurations have very little difference (see Fig. 5.2(b)), due to the lacking of the strong localized electric near field which is sensitive to the details of the nanostructure. Therefore, it would be hard to know information of the nanostructures from the far-field electric field (emission spectrum).

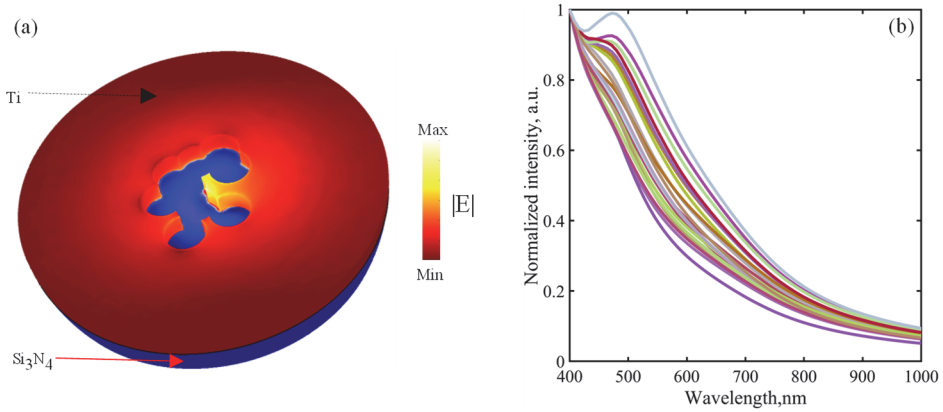

Figure 5. 2. CL from subwavelength dielectric apertures with different configurations. (a) Schematic and |E| (with unit of V/m) map (field map only represents in the Ti film) of one configuration with subwavelength dielectric (Ti) apertures. Air holes with radius of 50 nm are in the Ti film with thickness of 50 nm, Ti film on 100 nm Si_3N_4 membrane. The centre distance of nearest air hole is 60 nm. Configurations are randomly generated. (b) Simulated CL spectrum from the 20 randomly generated configurations in (a).

5.3 Neural network description

Neural networks are implemented in a statistics and machine learning toolbox in a commercial software (MATLAB 2019a). In the forward scenario (prediction of plasmonic aperture configuration based on emission spectra) the network consists of three layers, an input layer, a feedforward neural network (FFNN) layer with 20 neurons and an output layer. In order to prepare the CL spectrum for input to the network, I consider the emission counts at 30 fixed wavelengths. In a similar fashion, the configuration of plasmonic apertures is encoded in the following format: each configuration is represented by 16 bits with each bit corresponding to a site in the 4x4 grid. A value of "0" ("1") indicates absence (presence) of a hole at the site. Thus configuration "0000000000000000" corresponds to continuous film, while "1111111111111111" to a 4x4 array of holes. In addition to predicting the full configuration, I also consider single-number characteristics of the configuration: total hole number, neighbouring hole number, average neighboring hole number and total hole area of the configuration.

A similar network is employed for the inverse scenario (prediction of emission spectra from plasmonic apertures). Here, in addition to the full spectrum, I consider prediction of peak wavelength and peak intensity.

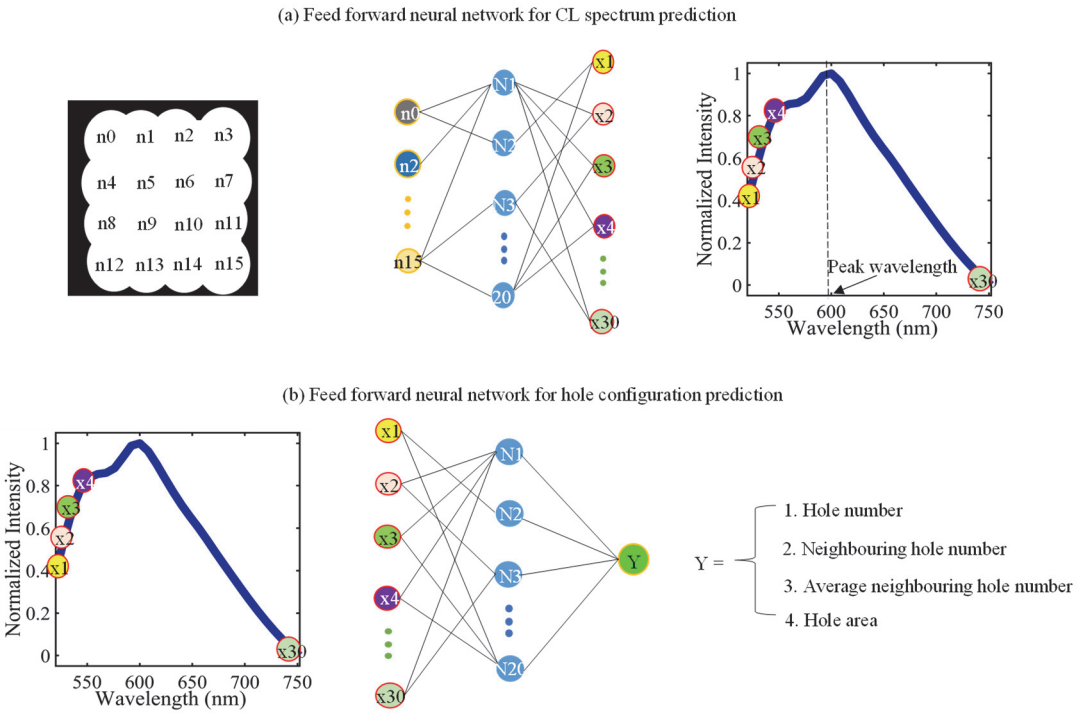

Figure 5. 3. Neural network for CL spectrum and air hole number predictions. (a) The configuration information was represented by a one-dimensional vector as the input of the 20 layers feed forward neural network, there are 30 output neurons form the spectrum. (b) The spectrum information was represented by a one-dimensional vector as the input of the 20 layers feed forward neural network, there are 1 output neuron represents the hole number or neighbouring hole number or average neighboring hole number or hole area of configuration.

5.4 AI-retrieval of emission spectrum from geometry: computational demonstration

In this section, I demonstrate the retrieval of emission spectral characteristics from plasmonic aperture configurations. In particular, I consider two cases including the wavelength position of the emission peak and the full emission spectrum. The input to the network comprises information about the configuration of plasmonic apertures. The network is trained on a large set of over 2,000 spectra together with the corresponding configurations, which are separated to a training set (80%), a validation set (10%) and a test set (10%).

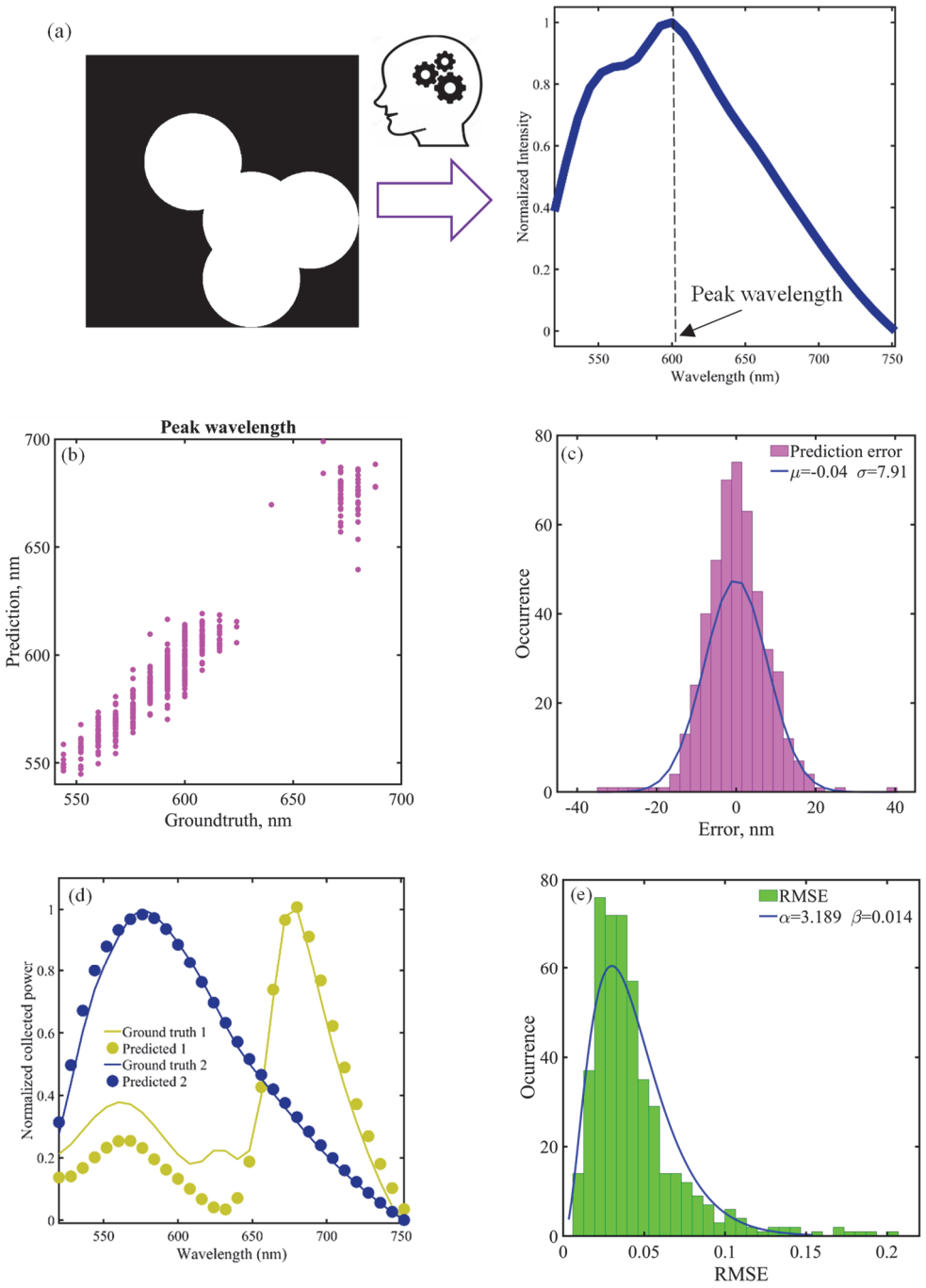

Figure 5. 4. AI predicts peak wavelength of CL spectrum and AI predicts CL spectrum from plasmonic configurations with numerical dataset. (a) An example to illustrate the schematic of predicting peak wavelength of CL spectra and predicting CL spectra from configuration. (b) Ground truth VS prediction in the test process of peak wavelength prediction task. (c) The histogram of prediction error of peak wavelength prediction task. The histogram is fitted by a Gaussian distribution, where μ is the mean and σ is the standard deviation (in nm). (d) Two examples of predicting CL spectrum after artificial neural network trained. Lines are ground truths and dots are predictions. (e) The RMSE histogram of prediction vs ground truth after network has been trained, where $\alpha\beta$ (0.045) is the mean and $\alpha\beta^2$ (0.0006) is the standard deviation.

The trained neural network can predict peak wavelength with high accuracy as shown in Fig. 5.4 (b)). The accuracy here is quantified through the error in the peak wavelength estimation. The distribution of error of all the predictions in the test process is shown in Fig. 5.4 (c), where we see an average error of about 0.04 nm and a spread of ~8 nm. Subsequently, the network is

requested to retrieve the full emission spectrum (as shown in Fig. 5.4 (d)). Here, the root mean square error (RMSE) of each emission spectrum retrieval was used to describe the performance of the trained network. The distribution of RMSE of all the predictions in the test process is shown in Fig. 5.4 (e). Here, the peak of the error distribution is at 0.014 which demonstrates the trained network has a very high accuracy to predict the CL spectrum.

5.5 AI-retrieval of geometry from emission spectrum: computational demonstration

Deep learning helps to push the limits of optical information storage [182]. The subwavelength plamsonic apertures we employ here also are kinds of information carrier. The configuration information including hole number, neighbouring hole number, 16 bit digital information from 0000000000000000 to 1111111111111111, etc. In this section, I numerically demonstrate the prediction of configuration information from CL spectrum (see Fig. 5.5 (a)). The numerical dataset is the same in the task of predicting CL spectrum from plasmonic configurations.

Firstly, I consider the retrieval of key parameters of the plasmonic aperture configuration: total number of holes, total number of nearest-neighbouring holes and average number of neighbours per hole. Whereas the first provides a measure of the gold covered area, the second and third quantify the distribution of holes in the configuration. Figure 5.5(b) shows the ground truth VS prediction for the total hole number prediction task and Fig. 5.5(c) shows the corresponding prediction error distribution. I can observe an average error is 0.13 and the standard deviation is 0.93 which is smaller than a single hole number, which means there is high accuracy of prediction. I define the total number of neighbouring holes of a configuration as the number of all nearest neighbours for each hole summed over all holes in the configuration. For example, there are 2 neighbouring holes in the configuration shown in Fig. 5.5(a). This number represents the hole density which is an important characteristic of the configuration. Figure 5.5(d) shows the ground truth VS prediction for the neighbouring hole number prediction task and Fig. 5.5(e) shows the prediction error distribution in which the average error is 0.16 and the standard deviation is 3.92. Similarly, the average number for neighbours per hole can be employed as a metric of the hole density. Figure 5.6 shows the prediction performance for these two prediction tasks, the average error is 0.02 and the standard deviations is 0.47.

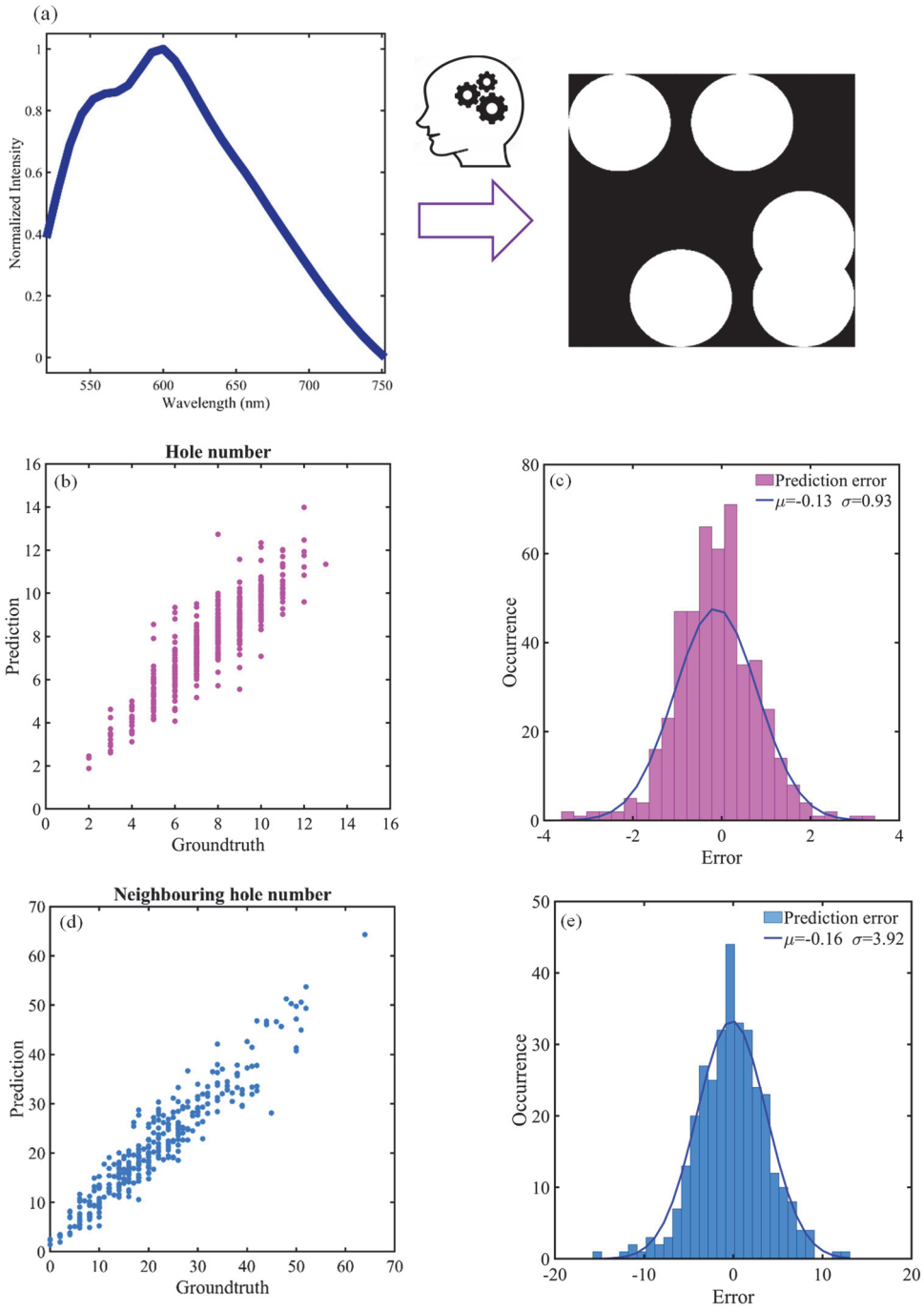

Figure 5. 5. AI predicts plasmonic configurations from CL spectrum with numerical dataset. (a) An example to illustrates the schematic of predicting configuration from a CL spectra. (b) and (d) Prediction VS ground truth of hole number and neighbouring hole number prediction task in the test process. (c) and (e) The histograms of prediction errors of hole number and neighbouring hole number prediction task. The histograms are fitted by Gaussian distributions, where μ is the mean and σ is the standard deviation.

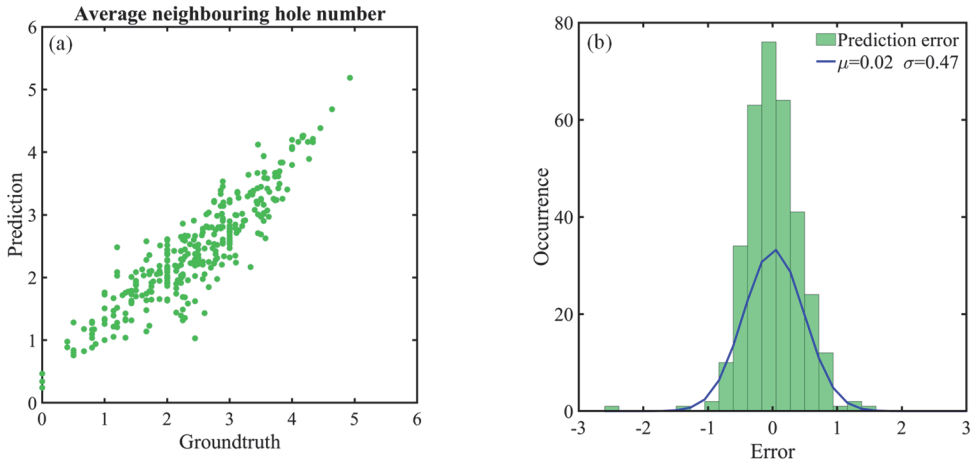

Figure 5. 6. AI predicts plasmonic configurations from CL spectrum with numerical dataset. (a) Prediction VS ground truth of average neighbouring hole number prediction task in the test process. (b) The histograms of prediction errors of average neighbouring hole number prediction task. The histograms are fitted by Gaussian distributions, where μ is the mean and σ is the standard deviation (in nm^2 in (d)).

5.6 AI-retrieval of geometry from emission spectrm: preliminary experiments

To demonstrate experimentally the concepts introduced in this chapter, I consider a large number of plasmonic aperture configurations fabricated by creating holes on a glass substrate by focused ion beam milling (sample fabricated by my supervisor Dr Jun Yu Ou) and collecting the corresponding emission spectra by cathodoluminescence. There are some differences between designed and fabricated samples as shown in Fig. 5.7(a). The holes are connected to each other even according the design they should be separated by 1 or more sites. The differences come from the finite size of the ion beam. In the CL measurement, the electron beam energy is 30kV with probe beam current ~ 1nA. To minimize positioning errors the electron beam is defocused so that it covers the full configuration. Fig. 5.7(a) shows characteristic examples of measured CL spectra, which have been normalized to the peak intensities. Importantly, my measurements indicate that different configurations lead to dramatically different spectra despite the departure of the fabricated structures from their respective designs. The CL spectra are also smoothed before fed in the input of the neural network as shown in Fig. 5.7(c). The dataset included 450 different plasmonic aperture configurations with their spectra. 80% was used for training, while the remining was used for training. Further details on fabrication and measurement are detailed in Chapter 2.

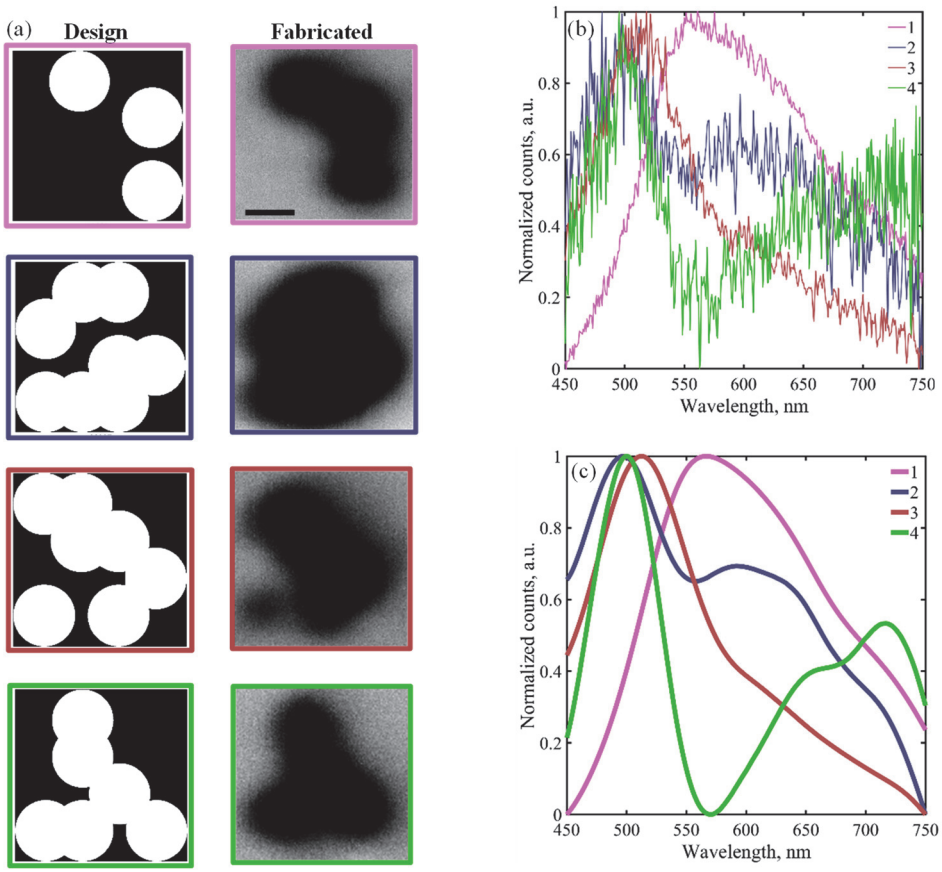

Figure 5. 7. Experimentally CL spectrum of plasmonic configurations. (a) Four different plasmonic configurations and corresponding samples, the scale bar is 50 nm. (b) Measured CL spectrum in (a), line color corresponding to the configurations in (a) with the same outline color. (c) The smoothed spectrum of (b).

Information about the geometry of the configuration of plasmonic apertures is obtained similarly to the numerical case, with similar network settings. Neural network retrieved results for total hole numbers, neighbouring hole numbers and average neighbouring hole numbers are presented in Figs 5. 8 and 5.9. The network retrieved values follow the ground truth in general, although the errors are substantially larger from the numerical case. In particular, the average error is 1.09 and standard deviation is 2.22 for the total hole number prediction task. Similarly, the average error is 4.93 and standard deviation is 11.82 for the neighbouring hole number prediction task. The network predictions are somewhat improved for the case of average neighbouring hole numbers, where the average error is close to zero (0.09) while the spread remains smaller than 1 (0.85).

There are several factors contributing to the low prediction accuracies of neural network trained with the experimental dataset:

1. Fabrication imperfections: The fabricated samples deviate strongly from the target designs with substantial hole overlap. This significantly affects the network ability to distinguish different configurations. difference makes the hole between two holes is not necessary any more, which means the same CL spectrum can corresponding to more than two different configurations.

2. Beam positioning errors. Owing to the finite spatial resolution of the SEM, the beam

may deviate from the center of the measured configuration. Such errors have been mitigated to some extent by defocusing the electron beam to a size comparable to that of the full configuration. However, the electron density distribution is not homogeneous across the electron beam, which means that positioning errors may persist. I have quantified such errors by looking at the reproducibility of the results upon successive repositioning of the electron beam. The results are shown in Fig. 5.10 indicating that repositioning errors do not qualitatively affect the shape of the spectrum. Although such effects appear small, their influence in the network training remains to be explored.

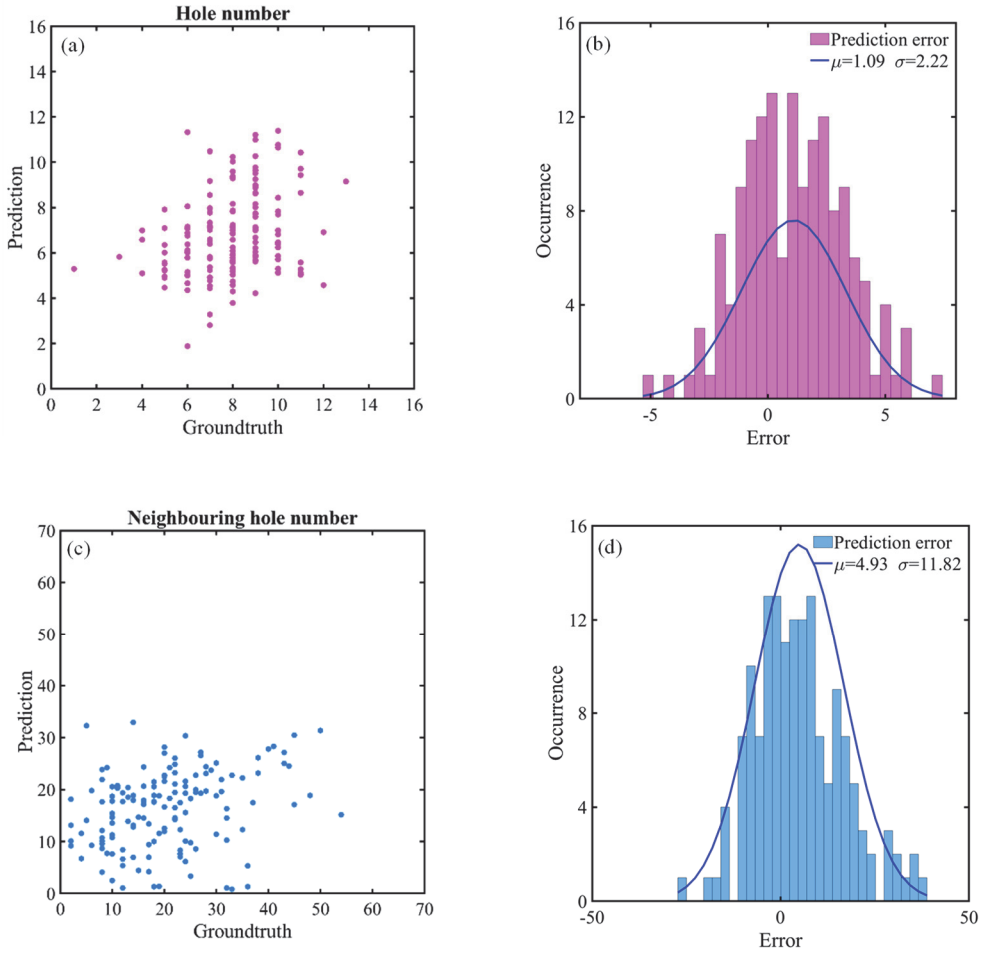

Figure 5. 8. AI predicts plasmonic configurations from CL spectrum with experimental dataset. (a) and (c) Prediction VS ground truth of hole number and neighbouring hole number prediction task in the test process. (b) and (d) The histograms of prediction errors of hole number and neighbouring hole number prediction task. The histograms are fitted by Gaussian distributions, where μ is the mean and σ is the standard deviation.

3. Dataset size. The experimental dataset is substantially smaller than the one used in the numerical simulations by over a factor of 5. Even more so, experimental errors and fabrication imperfections typically result in requirements for larger datasets.

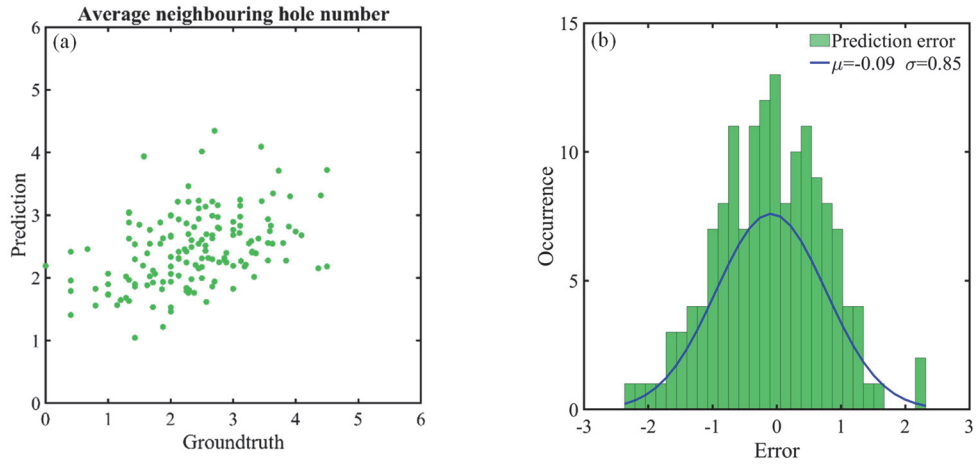

Figure 5. 9. AI predicts plasmonic configurations from CL spectrum with experimental dataset. (a) Prediction VS ground truth of average neighbouring hole number prediction task in the test process. (b) The histograms of prediction errors of average neighbouring hole number prediction task. The histograms are fitted by Gaussian distributions, where μ is the mean and σ is the standard deviation.

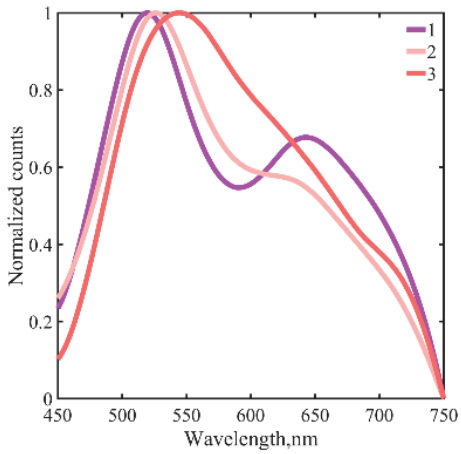

Figure 5. 10. Three times measurement of CL spectrum taken on the same configuration.

5.7 Summary

This chapter explores the possibilities provided by artificial intelligence in the analysis of emission spectra from nanoscale emitters. In particular, I demonstrate that in the case of small ensembles of plasmonic apertures, neural networks can retrieve information regarding the geometrical arrangement of such ensembles from the far-field emitted spectra. My simulations indicate that characteristics, such as number of apertures and measures of aperture density (e.g. number of nearest-neighbours), can be accurately predicted by feed forward neural networks with small errors of a few %. The inverse situation can also be addressed by a similar approach, where full emission spectra can be obtained by feeding information about the plasmonic aperture configuration into a neural network with high accuracy. I have also tested this concept experimentally, where I show that similarly to the numerical case neural networks can predict geometrical characteristics of the configuration. However, in this case the error is a factor x2-x3 larger. This is attributed to a combination of smaller experimental dataset size, fabrication imperfections and experimental errors, in particular with respect to beam positioning.

The operation principle of the suggested approach is based on the excitation of plasmonic modes in the apertures. Here such modes mediate the interaction between the different areas within a single

configuration, which is imprinted in the far-field emission spectrum. I corroborate this by performing calculations of emission spectra from dielectric apertures arranged in similarly-sized configurations, where the absence of plasmonic interactions leads a much weaker dependence of emission spectra on the fine geometrical details of the configuration.

The results presented in this chapter are expected to be of great interest in both analysis of cathodoluminescence spectra from nanostructured materials as well as in practical applications. In the former case, there are exciting opportunities in pushing the size of the target object to even smaller dimensions, beyond the SEM resolution limits, while still retaining the ability to identify the object based on its emission spectrum. In the case of applications, one can envisage tagging schemes based on nanoscale barcodes, where instead of imaging scattering patterns intensity, recording emission at a few different frequencies is sufficient for identification.

Chapter 6

Conclusions

6.1 Summary

My research work focused on the effects of the dielectric properties of the ambient environment on the emission dynamics and scattering properties of quantum emitters and resonators, respectively. The quantum emitter of choice here is the NV center in diamond, which is commercially available and well studied with potential for applications in quantum technologies, sensing and so on. Emission properties were studied with time-resolved cathodoluminescence (TR-CL) with temporal resolution of a few ns.

I have experimentally demonstrated decay rate enhancement of NV^0 centers in nanodiamond (ND) clusters by introducing a dielectric thin film between the emitter and the supporting substrate (Si). My results indicate that this is sufficient to tune radiative decay rate within ~90% as a result of interactions between the emitter and the resonant modes of the thin film. My measurements indicate the absence of correlations between the NV lifetimes and the geometrical characteristics of the ND clusters, thus the observed decay rate enhancement cannot be attributed to such factors. This analysis provides insights into the mechanism of decay rate enhancement of NV emission from NDs deposited on thin films and puts forward simple means of controlling the corresponding emission statistics.

I have demonstrated the engineering the collapse of lifetime distribution of NV centres in nanodiamond by chalcogenide films. Here, the increased nonradiative decay rate dominates over the radiative decay rate leading to this dramatic change in lifetime statistics. Numerical modelling results have shown that the observed changes in the lifetime statistics are underpinned by two mechanisms. One of the mechanisms is dissipation in lossy chalcogenide films, which enhances non-radiative decay to the extent that it completely dominates radiative decay for NDs embedded in the films. While such a mechanism naturally reduces the brightness of a single NV centre, in practice the intensity of fluorescence can be maintained at a sufficient level in NDs containing many centres. The other mechanism corresponds to an interplay between scattering and absorption of emitted photons. Also, I have analyzed the spectral characteristics of NV centres in chalcogenide materials in detail and found that the phonon sideband (PSB) centre frequency distribution exhibits a red shift and its spread becomes narrower when NDs embedded in SbTe film while PSB linewidth distribution remains almost the same. Unlike PSB, zero phonon line (ZPL) is less affected by the surrounding environmental conditions, such as external strain, temperature. Moreover, the spectral characteristics of NV centres in NDs embedded in SbTe film are independent of the dielectric properties of SbTe film.

The possibilities provided by artificial intelligence in the analysis of emission spectra from nanoscale emitters have been explored. Neural networks can retrieve information regarding the geometrical arrangement of small ensembles of plasmonic apertures from the far-field emitted spectra. The simulations indicate that the ensembles' characteristics, such as number of apertures and measures of aperture density (e.g. number of nearest-neighbours), can be accurately predicted by feed forward neural networks with small errors of a few %. The inverse situation can also be addressed by a similar approach. This concept has also been tested experimentally, but the error is a factor x2-x3 larger, which is attributed to a combination of smaller experimental dataset size, fabrication imperfections and experimental errors, in particular with respect to beam positioning.

6.2 Outlook

In addition to the time-resolved CL measurement on NV centres in NDs reported in this thesis, angle-resolved and Hanbury Brown-Twiss (HBT) CL have been shown to reveal the spatial and quantum properties of the emission from NV centres. Investigating the statistics of the emission pattern in different NDs can may be able to provide information about the number and orientation of the NV centres. The NDs studied here have multiple NV centres, which exhibit (anti)bunching properties in HBT-CL measurement. A single NV centre in ND shows antibunching indicating that it is a single photon source. Studying single NV centres in ND is an important next step of this work.

The large number of NV centres (~1000) in a single ND may be employed a platform for artificial intelligence, whereby individual NV centers act similarly to neurons a neuronal network (or the brain). NV centers interact strongly with one another representing neuronal connections (synapses). A key ingredient of such a scheme is nonlinearity, which can be introduced here by noting that the ND emission saturates at high currents. On the other hand, dynamics are provided by the NV centres decay time (at the nanosecond scale). Thus NV centers in diamond may be used for the realization of a a time delay single node photonic reservoir computer.

Appendix A

Publications

Journal Publications

1. H. Li, J. Y. Ou, V. A. Fedotov, and N. Papasimakis, Decay rate enhancement of diamond NV-centers on diamond thin films. Opt. Express, (2021) doi: 110.1364/OE.425706.
2. H. Li, J. Y. Ou, B. Gholipour, J. K. So, D. Piccinotti, V. A. Fedotov, and N. Papasimakis, Engineering the Collapse of Lifetime Distribution of Nitrogen-Vacancy Centers in Nanodiamonds. Applied Physics Letters, 118 (2021) 261103.
3. H. Li, J. Y. Ou, V. A. Fedotov, and N. Papasimakis, Coupled resonators in media with near-zero refractive index. (To be submitted)
4. H. Li, J. Y. Ou, V. A. Fedotov, and N. Papasimakis, Nano-objects identification by AI with their emission spectrum. (In preparation)
5. H. Li, J. Y. Ou, V. A. Fedotov, and N. Papasimakis, Research progress of NV centres in nanodiamond for nanophotonics. (In preparation)

Conference Contributions

Presenting author underlined

1. (Oral) H. Li, J. Y. Ou, V. A. Fedotov, N. Papasimakis and N. I. Zheludev, Emission of Diamond NV Centers in Dielectric, Semiconducting and Plasmonic Environments, CLEO 2020 Virtual Conference, 11-15 May 2020
2. (Oral) H. Li, J. Y. Ou, N. Papasimakis, V. A. Fedotov and N. I. Zheludev, Decay rate statistics of NV centres in diamond on plasmonic and dielectric substrates, Electron Beam Spectroscopy for Nanophotonics 2019 (EBSN 2019), Paris, France, 16-19 Sept 2019
3. (Oral) H. Li, J. Y. Ou, N. Papasimakis, V. A. Fedotov and N. I. Zheludev, Lifetime distributions of NV centres in diamond on plasmonic and dielectric substrates, Nanophotonics and Micro/Nano Optics International Conference (NANOP 2019), Munich, Germany, 4 - 6 Sept 2019
4. H. Li, J. K. So, B. Gholipour, D. Piccinotti, N. Papasimakis, V. F. Fedotov, W. Gao, B. Hayden, and N. I. Zheludev, Quantum emitters in epsilon-near-zero and negative epsilon environments, Nanometa 2019, Seefeld, Austria, 3 - 6 Jan 2019

Appendix B

Coupled resonators in media with near-zero refractive index

B.1 Introduction

Materials with near-zero electromagnetic parameters, such as media with near-zero permittivity (ENZ) and media with simultaneously near-zero permittivity and permeability (EMNZ), provide new opportunities to tailor the interaction of wave and matter [184-186]. For example, it has been suggested that ENZ modes interacting with dipole resonators may enable control of the spectral properties of semiconductor nanolayers [187], nonlinearity coupled to and comes from ENZ materials [188, 189], quantum emitters in open ENZ cavities are predicted to allow switching between radiating and non-radiating modes [190], while EMNZ waveguide super coupling can be employed to control dipole-dipole interactions between emitters [191]. It has also been demonstrated that plasmonic antennas on ENZ substrates exhibit resonance pinning and suppressed near-field interactions [191, 192].

Here I study numerically coupling phenomena in plasmonic and dielectric resonator dimers embedded in near-zero refractive index (NZRI) media. In contrast to dielectric hosts with n>>0 where placing resonators close to one another leads to mode splitting, I show that both the resonance frequency and linewidth, as well as resonant mode are largely independent of the separation distance of the dimer constituents even for distances as small as λ/200. At the same time, in the case of plasmonic dimers, I have demonstrated that absorption increases substantially by decreasing the dimer separation distance. My results indicate that closely packed resonators embedded in NZRI hosts could be employed for the construction of strongly absorbing layers without the typically observed mode splitting and spectral reshaping.

B.2 Methods

In my study, I consider plasmonic (Au) and dielectric (Si) resonator dimers embedded in NZRI media. The resonators target the visible (Au) and mid-IR (Si) parts of the spectrum with corresponding radii of 25 nm and 1.8 μm. The permittivity of gold is defined by ref. [193], while silicon is considered to be dispersion-less with n=3.48 [194].The NZRI host is defined by $\varepsilon_{NZRI} = \mu_{NZRI} = 0.01 + 0.01 * i$, and thus are impedance matched to free-space. The NZRI host is a slab which extends infinitely in the yz plane and has a thickness of 1.2 μm . For simplicity, I consider infinitely long cylindrical resonators (see Fig. B.1) and solve the 2D scattering problem by a commercial finite element solver (COMSOL 5.3a). The resonators are illuminated by a plane wave and quantify the strength of the resonant excitation either through absorption

(plasmonic) or electric field intensity (dielectric).

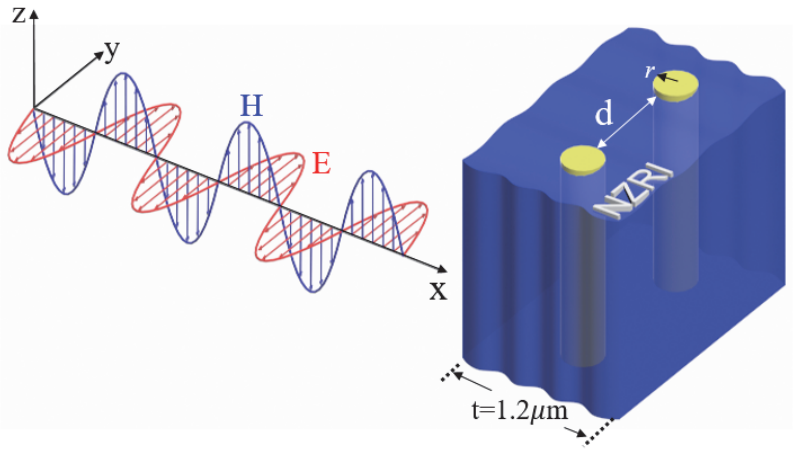

Figure. B. 1. Schematic of an infinitely long cylindrical resonator in the media with NZRI and illuminated by a plane wave polarized along the y-axis.

B.3 Plasmonic dimers in near-zero refractive index media

Figure B.2 shows the spectra of an infinitely long cylindrical resonator in the air (n=1) and in the NZRI medium. The resonant wavelength of gold nano rod in the free space is at 437.5 nm while it blue shifts to 412 nm when it is in the NZRI (see Fig. B.2(a-b)), which is due to the wavelength in the NZRI media becomes longer ($\lambda_{NZRI} = \frac{\lambda}{n_{NZRI}}$). The resonance condition here is similar to the quasistatic plasmonic nanoparticle resonance [195] and corresponds to the wavelength where the real apart permittivity of the Au is zero. In addition, absorption becomes lower together with the Full width of half maximum (FWHM) reduced about a half, this is because the electric field localized less inside the gold nano rod (see field maps in the inset of Fi. B.2(a-b)). Electric field maps indicate that both in the case of air and NZRI, the excited mode is of electric dipole character (see field maps in the inset of Fi. B.2(a-b)).

Resonator dimers are known to exhibit substantially different behavior compared to that of single isolated resonators [195]. Here, I consider a cylindrical resonator dimer where both resonators are placed on the same plane transverse to the propagation direction (along x) and are separated by distance d (edge-to-edge). In the case of dimer embedded in the air reducing the separation distance leads to broadening of the absorption peak and eventually splitting of the resonance due to the appearance of gap plasmon mode (see Fig. B.2(a) & Fig. B.2(e-g)). On the other at longer distances the interaction between the two resonators is minimal and the dimer constituents behave similarly to a single resonator. Conversely, for dimers embedded in NZRI media varying the separation distance does not affect the resonance line shape, neither in terms of resonance position or linewidth (see Fig. B.2(b) & Fig. B.2(e-g)). However, in contrast to dimers in air, decreasing the separation distance leads to a substantial increase in absorption by ~50%. This corresponds to essentially an increase in oscillation amplitude in the plasmonic rod and stands in sharp contrast to the usually observed mode splitting and quenching-like behavior

for closely spaced metallic resonators.

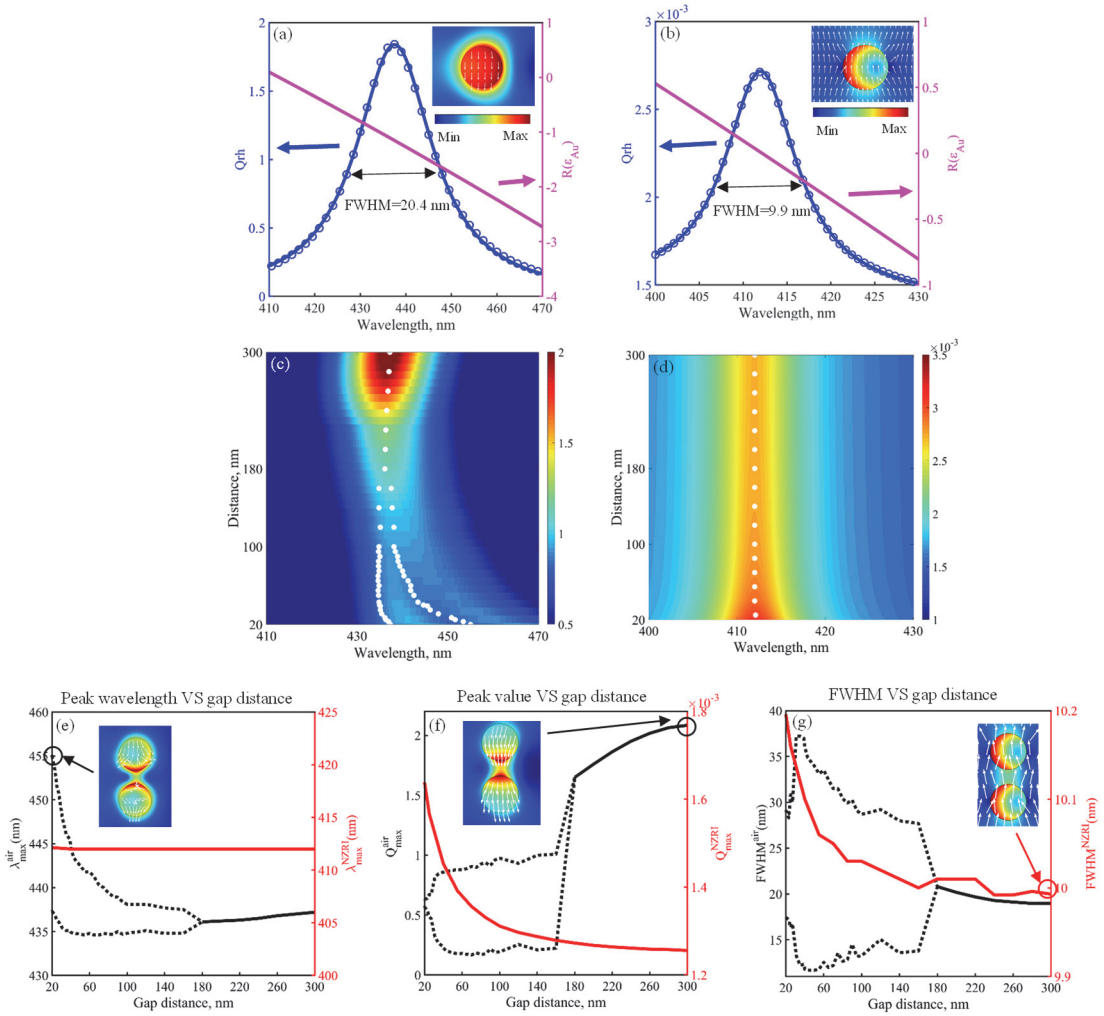

Figure. B. 2. The resonant behaviors of gold nano rods in the free space and NZRI. (a-b) Simulated normalized heat resist spectrum (blue curve), Lorentzian fitting (blue circle), the real part permittivity of gold (purple), the FWHM are 20.4 nm and 9.9 nm respectively. Inset: the electric field map and polarization vector of gold nano rod in free space and displacement map and polarization vector of gold nano rod in NZRI at the resonant wavelengths 437.5 nm and 412 nm respectively. The gold nano rod dimers in the free space and NZRI (c-d). (c) Normalized heat resist map versus gap distance (20 nm~300 nm) and wavelength when gold nano rod dimer in the free space, and (d) the normalized heat resist map with gap distance in the range of 20~100nm. The white dot is the fitting results. The resonant behaviors of gold nano rods dimers in the free space and NZRI versus gap distance (e-g). (e) Resonant peak wavelengths. (f) Peak value. (g) Full width of half-maximum. Insets are the field map and displacement map at the corresponding wavelength and gap distance as the arrow indicated.

To further inverstigate how the Au rod resonance behavior influenced by the surrounding Au rods, I inverstigated how the average absorption in the Au rods depends on the Au rod densities. Here, I define a constant NZRI area with size of 1606 nm × 1606 nm and there are random number and random positions of 50 nm Au rods distributed in this area, so the maximum

number of Au rods in this area is 16 with gap distance 2 nm. These Au rods embedded in NZRI media varying the density of Au rods does not affect the resonance position while they are randomly distributed when Au rods are in the free space, which demonstrates the Au rods resonace behavior does not depends on the surrounding Au rods at all. This is because of the wavelength in the NZRI media is infinitely which prohibit the Au rods coupling as the field maps in Fig. 3 (c-d) shows.

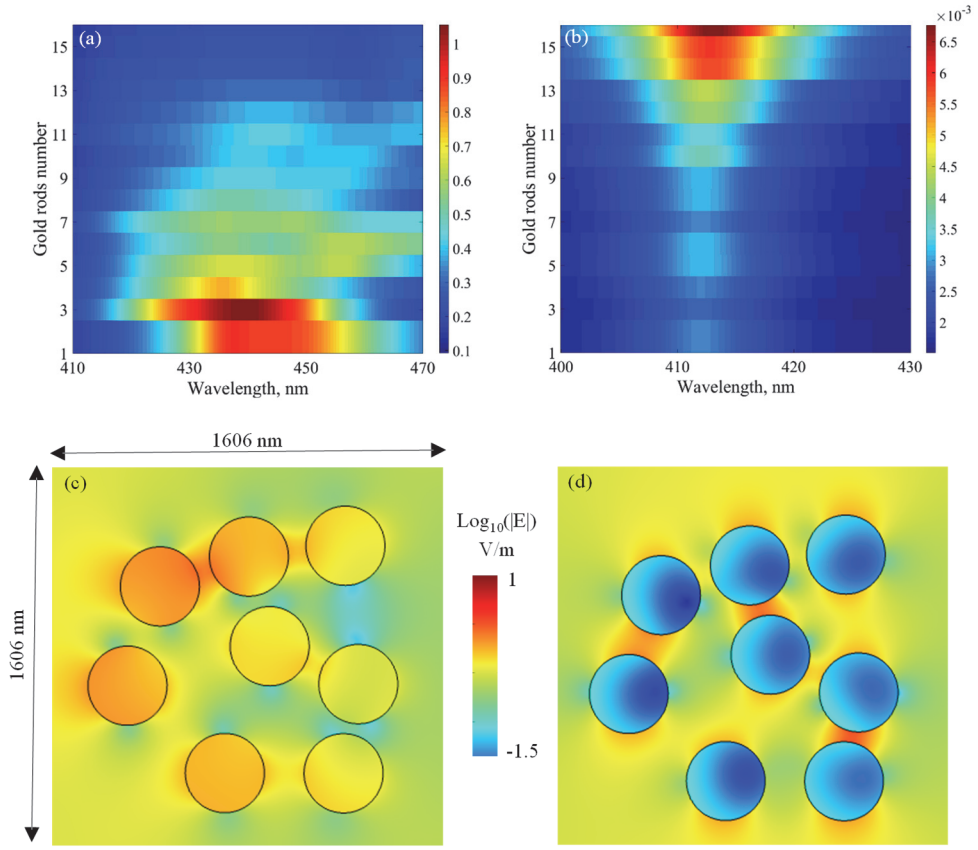

Figure. B. 3. Normalized heat resist maps versus gold rod numbers (1~16 rods in area with size 1606 nm ×1606 nm) and wavelength when gold nano rods in the free space (a), and NZRI (b). Electric field maps of randomly distributed 9 Au nano rods in areas with sizes 1606 nm ×1606 nm in air (c) and NZRI (d), respectively.

B.4 Dielectric dimers in near-zero refractive index media

In the meantime, I also study the coupling behavior of the silicon rods (with a radius of 1.8 μm) dimer in the NZRI, the gap distances d between the two rods vary from 2 μm to 8 μm, and I analyze only one silicon rod to reflect the properties of the whole dimer system. In contrast to the plasmonic case, there is no mode splitting when the silicon rods dimers either in the free space or in the NZRI within this gap distance range as shown in Fig. B.4 (a-b). The couplings of gold and silicon dimer in NZRI are both suppressed, which can be seen from the PW of the dimer system are always around the same wavelengths with the single rod resonance Fig. 8 a. However, due to the resonant schematics are different in gold and silicon rod, the electric magnetic fields on resonance are localized on the surface of the gold rod while they compressed

within the silicon rod, the PW in the gold dimer system is the blue shift and the red shift in the silicon dimer system with the gap distances increase when the dimer in the free space. Moreover, the PV and FWHM of the silicon rods dimers in the NRZI have the same monotonicity as it is in the free space as shown in fig B.4 (a-b), which is also different with gold nanorod dimers.

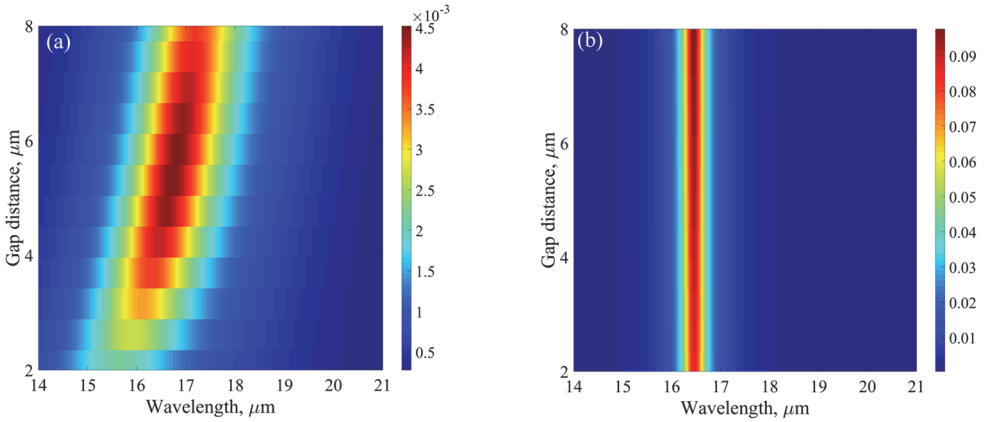

Figure. B. 4. The silicon rods dimers in the free space and NZRI. (a), (b) Normalized electric fields maps versus gap distance and wavelength.

B.5 Discussion

Naturally, there is no material with NZRI in the full spectrum but there are NZRI wavelengths in the dispersion media. Investigating the coupling behavior of the dimer system in the natural materials with the NZRI wavelengths would be more practically. Like the permittivity is described by the following Lorentzian model $\varepsilon = \varepsilon_\infty + \frac{\omega_p^2}{\omega_0^2 - \omega^2 - i\gamma\omega}$, where $\varepsilon_\infty = 0.5$, $\gamma = 8.72 \times 10^{10}\ rad/s$, ω_0=1.125$\times 10^{14}\ rad/s$, the permittivity described by this Lorentzian model with these parameters are shown in Fig. B.4 a, b, when $\omega = 1.147 \times 10^{14}\ rad/s$ that at the wavelength of 16.44 μm the $\varepsilon \approx 0.01{+}0.01i$. I simulated the silicon rods dimer with a radius of 1.8 μm in this dispersion NZRI and made it $\varepsilon = \mu$ and the gap distance varies from 50 nm to 8 μm. As I expected the normalized electric field density spectrum 'pinning' at the wavelength of 16.44 μm, and the peak value of electric field density increase when the gap distance becomes larger, which agrees well with the results in section B.4.

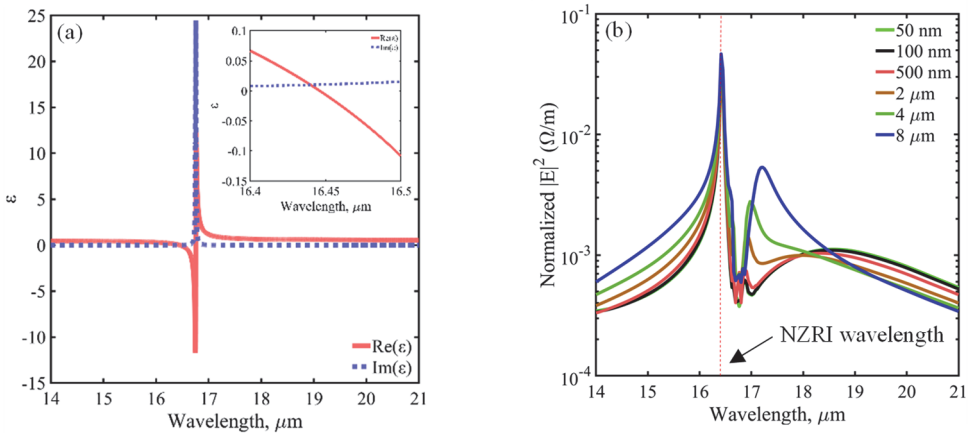

Figure. B. 5. (a) The permittivity of dispersion NZRI. Inset: the permittivity of dispersion NZRI with wavelengths range 16.4 μm to 16.5 μm. (b) The normalized square electric field densities spectrum of silicon rods dimer in the NZRI when gap distance varies from 50 nm to 8 μm.

B.6 Summary

In summary, I have numerically investigated the resonant properties of the single gold and silicon rod in the media with NZRI, and the coupling effects of the gold and silicon rod dimers in the NZRI with gap distances between the rods change. The resonant wavelength of both plasmonic and dielectric rods are ‘pining’ when there are in the NZRI , which are due to the wavelength in the NZRI media becomes longer. In addition, the resonant wavelength of the plasmonic rod in the NZRI is the same as the wavelength that the real permittivity of the plasmonic material is zero. My simulation results show that the coupling strengths are always the same no matter what the gap distances are and now matter how density of the Au rods are in the NZRI. Finally, I analyzed the case of the dielectric dimer system in the NZRI with dispersion, which makes my analysis can also be applied to natural materials with NZRI wavelengths.

Appendix C

Controlling nitrogen vacancy centre lifetime with metasurface

C.1 Introduction

A metamaterial as a wave-propagating medium is designed to exhibit extraordinary properties due to its functional microstructure, with a spatial periodicity whose periodic length is much less than the wavelength of the propagating waves. The properties predicted or verified so far include states of negative permittivity [196], negative permeability [197] and negative refractive index [198]. These properties have been used in applications such as perfect lenses [199] and cloaking [200]. Metasurfaces are the two-dimensional metamaterials, they are typically metallic thin films that are structured on the sub-wavelength scale and that are thin in comparison to the operational wavelength of the metamaterial. Metasurfaces of a different nature can be created by using optically thin films made of lossy materials (that is, imaginary part of the complex refractive index comparable to the real part) [201]. The phase changes on reflection or transmission of light at the boundary between lossy media can be substantially different from 0 or π [202, 203]. These nontrivial interfacial phase changes enable nanometre-thin films to substantially modify the light spectrum. Hyperbolic metamaterial was employed to enhance the decay rate from single NV center in NDs with a broadband enhancement [45]. However, NV centres emission enhanced by structured metamaterials still have not been reported yet. One challenge is how to design fabrication-friendly metasurface with resonance at NV centre ZPL.

Here, I have employed the metasurface with trap mode to modulate the emission properties of NV centres in NDs, the results show the NDs are weakly couplled to the electric fields in the metasurface which results in there is only small change of NDs lifetime and brightness distributions.

C.2 Metasurface deign

The metasurface consists of the structured Ag thin film and the glass substrate. I designed the resonance wavelength of metasurface to the ZPL of NV^0 centres which is 575nm. The thickness of the Ag film is 50 nm, there are two asymmetric air slits in one unit cell with period of 200 nm, the widths of two air slits are the same (50 nm) but they have different lengths (one is 95 nm, the other is 60 nm), as shown in fig C.1 (a). In the simulation, a linear polarized plane wave used as the excitation source (the polarization is shown as fig. C.1(a)). The material parameters of Ag taken from ref. [204]. In my desin, there is an trap mode in the metasurface, as Fig C.1 (c) shows there is a resonance at wavelength of 575 nm.

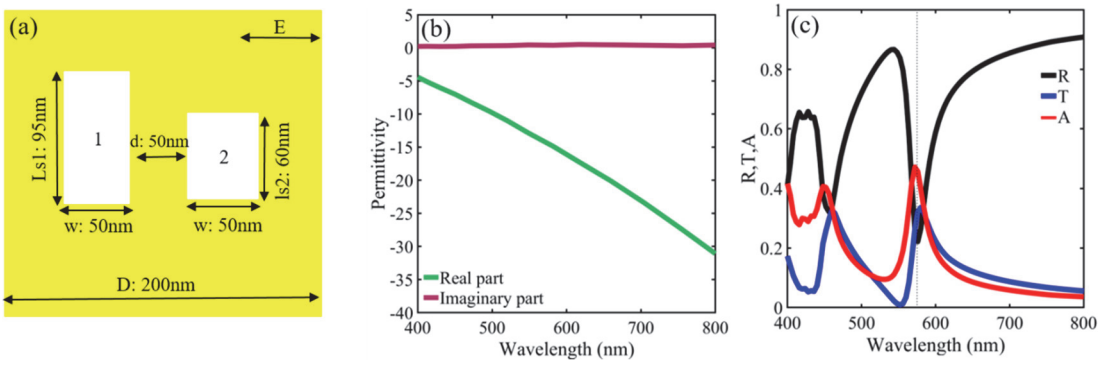

Figure C. 1. Metasurface design. (a) The geometry parameters of metasurface and polarization of the incident light. (b) The permittivity of Ag [204]. (c) Reflectance (R), transmission (T) and absorption (A) of the designed metasurface.

C.3 Fabricated metasurface

The fabrication of metasurface was performed by Focused-ion beam (FIB) milling by my colleague Dr. Oleksandr Buchnev. The fabricated metasurface was shown in fig. C.2(a). The resonance at wavelength of 575nm was also observed in the measured reflectance, transmission spectrum (measured by CRAIC) and absorption of the metasurface (see fig. C.2.(b)). The resonant wavelength in the fabricated sample has a shif due to the air hole size slightly different with the design in the simulation. In addition, the full width of half maximum becomes broader due to the optical loss of the material introduced during Focused-ion beam fabrication. However, the absorption peak of the trap mode is around ZPL of the NV^0 centre.

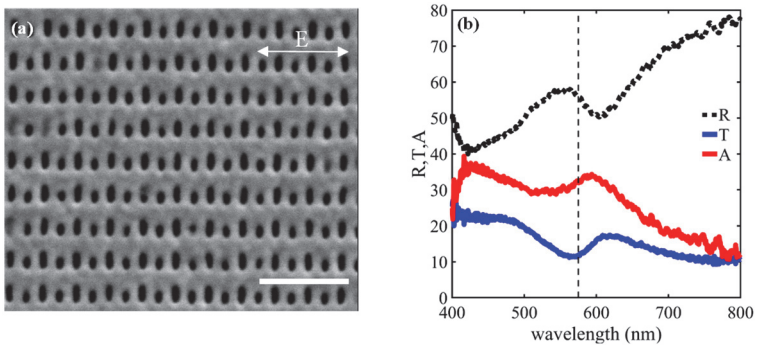

Figure C. 2. (a) SEM image of the metasurface sample. Scale bar is 500 nm. (b) Measured reflectance (R), transmission (T) and absorption (A) of the fabricated metasurface with the polarization as shown in (a).

C.4 Lifetime and brightness of nitrogen vacancy centres in nanoddiamond s in metasurface

The obtained metasurface sample was then coated via drop casting with a dispersion of NDs, which was prepared by diluting NDs in methanol and mixing the solution for 10 min in an ultrasonic bath. Figure C.3(a) shows a fragment of the sample featuring ND clusters on the metasurface. The lifetime of NV centres in NDs on metasurface was characterized by TR-CL, as a reference, NDs on the area without structuring was also measured. For both cases, I selected

a total of 60 ND clusters. The results of my measurements are summarized in Fig. C.3(b-c) in the form of boxplots. Compared with the reference, NDs on structured area displays a slightly shorter average lifetime nearing 14 ns while the lifetime of NV^0 centres is around 16.5 ns. The small change also can be observed in the spread of lifetime distribution. In addition, the brightness of NV centres slight reduced (~1 kcp/s)as well compared with the reference, which indicates a slightly nonradiated decay rate enhancement contributes to the lifetime decrease due to there is a weak absorption peak at NV centre ZPL. The experimental results demonstrated here are similarly with the NDs embedded in SbTe film which has been reported in Chapter 4. The low Q-factor of the metasurface results in the weak coupling between NV centres in NDs and metasurface. The local density of optical density state (LDOS) in the structurd metasurface is not homogeneously ditributed, this some how contributed to the spread of lifetime and brightnes do not have significantly reduced.

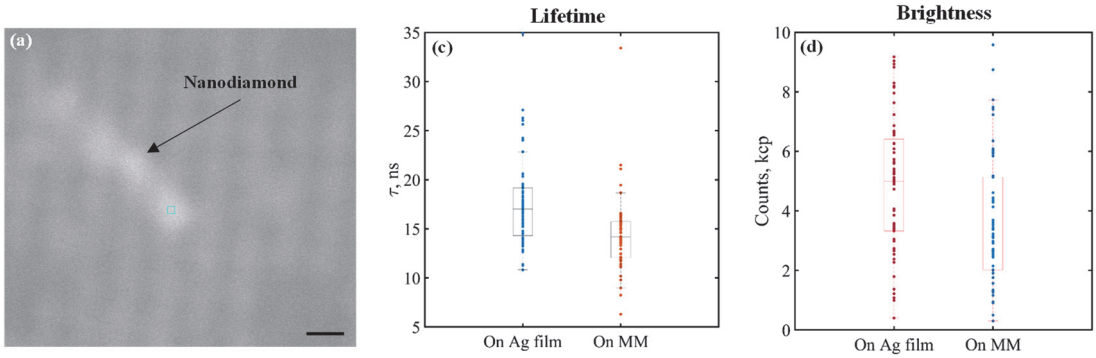

Figure C. 3. Experimental results. (a) SEM image of the a NDs cluster in the metasurace. Scale bar is 200 nm. (b) Boxplot of the distribution of lifetimes extracted from time-correlated histograms of NDs on Ag film and metasurface， respectively. (c) Brightness of emission from NDs corresponding to lifetime data in (b), kcp is kilo count per second. On each box, the central mark indicates the median, and the bottom and top edges of the box indicate the 25th and 75th percentiles, respectively. The whiskers extend to the most extreme data points not considered outliers. The points represent the experimental data.

C.5 Summary

In summary, I have employed the metasurface with trap mode to modulate the emission properties of NV centres in NDs, the results show the NDs are weakly couplled to the electric fields in the metasurface which results in there is only small change of NDs lifetime and brightness distributions compared with NDs on the un-structured areas. In contrast to dielectric and plasmonic resonators which can highly enhcance the decay rate of NV centres, the sturctured metasurface is hardly to make this achievement due to its low Q-factor. Looking forward to the said, the LDOS in the metasurface is not homogeneously distributed, which makes it is important to study how the decay rates of NV centre in NDs changed with the positions in the metasurface.

Appendix D

Angle-resolved CL, Hanbury Brown-Twiss (HBT)-CL for nitrogen vacancy centres in nanodiamond

D.1 Angle-resolved CL, HBT-CL system based on SEM

In addition the time-resolved CL measurement reported in the main text of this thesis, I also have performed a comprehensive studied on a single ND with angle-resloved and HBT-CL simultaneously. The SEM system based cathodoluminescence system also equippd with large array liquid nitrogen cooled CCD and time-correlated single photon counters, which enables the angle-resolved and Hanbury Brown-Twiss (HBT) CL measurements, respectively. (see Fig. D.1).

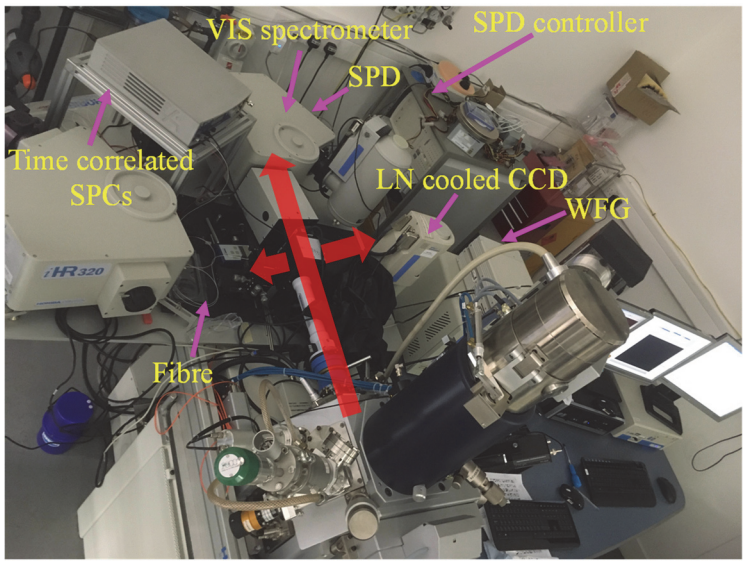

Figure D. 1 SEM based cathodoluminescence system equipped with liquid nitrogen cooled CCD and time-correlated single photon counters, which enables the angle-reoslved and Hanbury Brown-Twiss cathodoluminescence measurements, respectively.

D.2 Angle-resolved CL, HBT-CL for nitrogen vacancy centres in nanodiamond

CL mapping for a single ND contains multiple NV centres can some tells the information about how the NV cenres distributed in the NDs. Here, I have performed CL mapping for a single ND as shown in Fig. D. 2(a), the CL mapps for this ND shows the NV centres are homogeously

distributed in ND. Moreover,the emission pattern of NV centres in NDs determined by the orientations of the NV centres. I have performed the angle-resolved CL for the same ND, the result is shown in Fig D.2(c), from which I observe the electric field is randomly distributed in the space, which indicates the orientaions of the NV centre are randomnly distributed. Furthermore, I have performed the HBT-CL measurement for the same ND, the unti-bunching is clear observed in Fig. D.2(d), which has been observed in ref. [106].

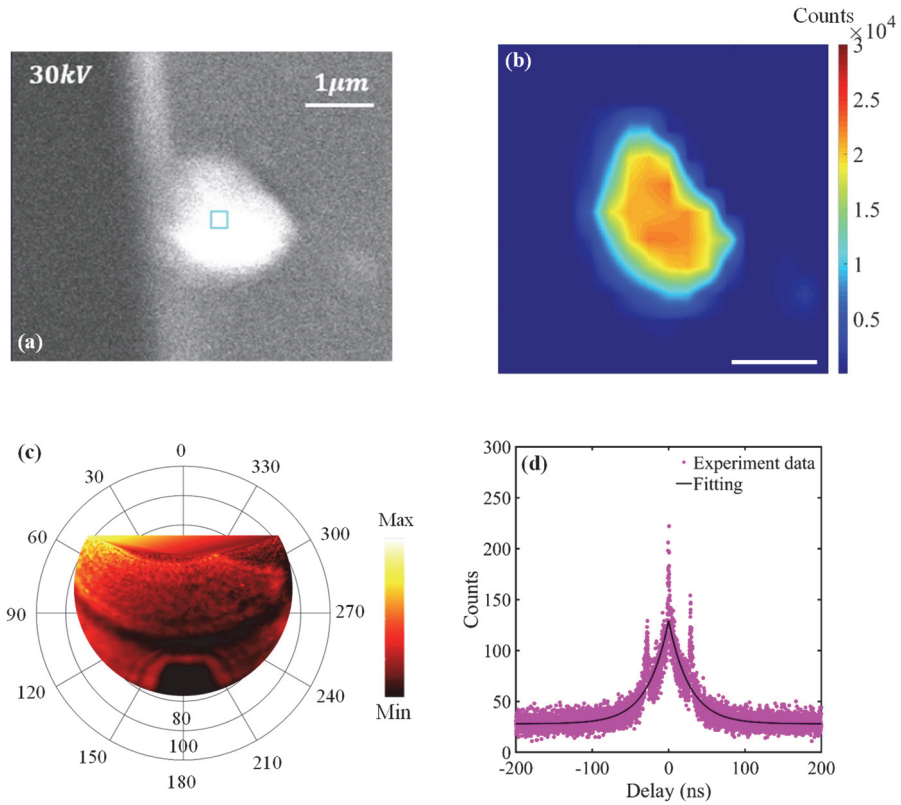

Figure D. 2 CL mapping, angle-resolved CL and HBT-CL for a same ND cluster contains NV centresd. (a) SEM image of a single ND cluster. (b) CL mapping for ND cluster corresponding with (a) at NV^0 centre ZPL, the beam current is 1.9 nA. (c) Angle-resolved CL of ND cluster corresponding with (a) at centre wavelength at NV^0 centre ZPL with bandwidth ~ 100 nm. (d) $g^{(2)}(\tau)$-CL ND cluster corresponding with (a) at centre wavelength at NV^0 centre ZPL with bandwidth ~ 100 nm. These two peaks around delay time of 50 ns is due to the reflections from the fibre connnectors which connect to the entrance of two time-correlated single photon detectors.

Appendix E

A shcematic of nitrogen vacancy centres in nanodiamond based reservoir computer

E.1 Schematic

The large amout NV centres (~1000) in a single ND can be assumed as the prenty of artificial neurons in the brain. The properties of NV centres in ND are affected with each other, which can be assumed the neurons connections. Moreover, the ND emission would be saturated in the large amout electrons' excitation, and the NV centres decay time is at the nanosecond scale, they both provide the nonlinearity and dynamic which are necessary to realze a time delay single node photonic reservoir computer. The schematic of NV centres in ND based reservoir computer proposed by me is shonw in Fig. E.1.

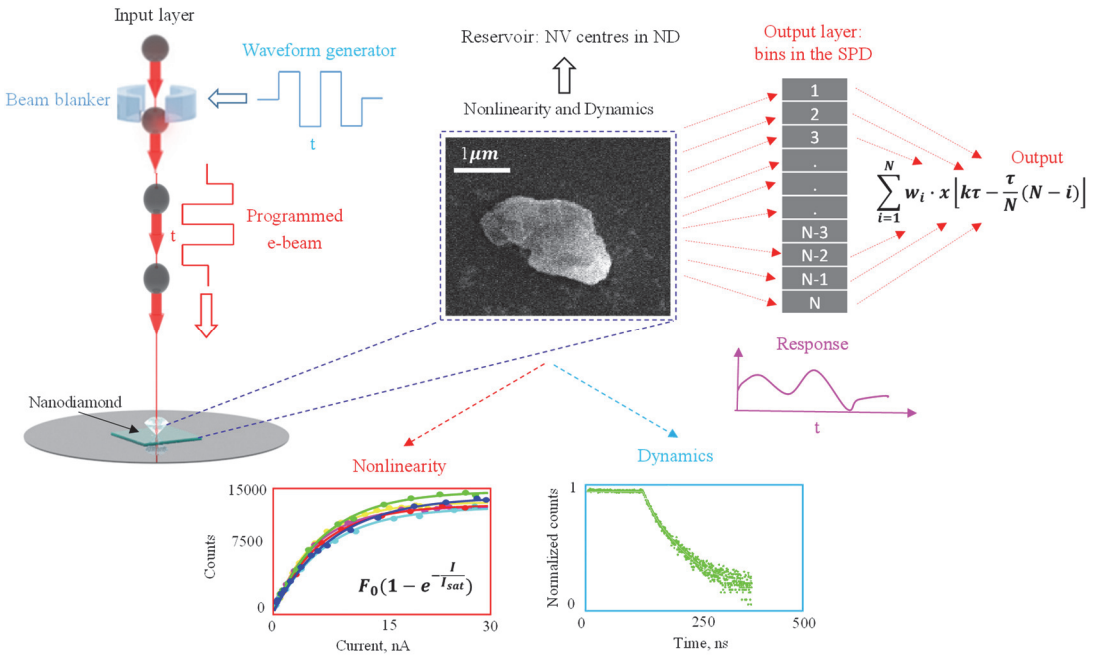

Figure E. 1 A schematic of NV centres in nanodiamond based reservoir computer.

Bibliography

[1] L. N. a. B. Hecht, "Quantum emitters," *Principles of nano-optics,* pp. 304–334.

[2] M. W. M. Doherty, Neil B. Delaney, Paul Jelezko, Fedor Wrachtrup, Jörg Hollenberg, Lloyd C. L., "The nitrogen-vacancy colour centre in diamond," *Physics Reports,* vol. 528, no. 1, pp. 1-45, 2013, doi: 10.1016/j.physrep.2013.02.001.

[3] A. B. R. Brouri, J.-. Poizat, and P. Grangier, "Photon antibunching in the fluorescence of individual color centers in diamond," *Optics Letters,* vol. 25, no. 17, 2000.

[4] S. M. C. Kurtsiefer, P. Zarda, and H. Weinfurter, "Stable Solid-State Source of Single Photons," *Phys Rev Lett,* vol. 85, no. 2, 2000.

[5] G. Alagappan, L. A. Krivitsky, and C. E. Png, "Purcell enhancement of light emission in nanodiamond using a trenched nanobeam cavity," *Journal of Optics,* vol. 22, no. 2, 2020, doi: 10.1088/2040-8986/ab66cd.

[6] J. R. Rabeau, S. T. Huntington, A. D. Greentree, and S. Prawer, "Diamond chemical-vapor deposition on optical fibers for fluorescence waveguiding," *Applied Physics Letters,* vol. 86, no. 13, 2005, doi: 10.1063/1.1890484.

[7] Q. Zhang, H. Yu, M. Barbiero, B. Wang, and M. Gu, "Artificial neural networks enabled by nanophotonics," *Light: Science & Applications,* vol. 8, no. 1, 2019, doi: 10.1038/s41377-019-0151-0.

[8] J.-Y. O. Tanchao Pu, Vassili Savinov, Guanghui Yuan, Nikitas Papasimakis, Nikolay I. Zheludev, "Unlabeled far-field Deeply Subwavelength Topological Microscopy (DSTM)," 2020.

[9] D. Piccinotti, K. F. MacDonald, S. Gregory, I. Youngs, and N. I. Zheludev, "Artificial Intelligence for Photonics and Photonic Materials," *Reports on Progress in Physics,* 2020, doi: 10.1088/1361-6633/abb4c7.

[10] T. Pu, J. Y. Ou, N. Papasimakis, and N. I. Zheludev, "Label-free deeply subwavelength optical microscopy," *Applied Physics Letters,* vol. 116, no. 13, 2020, doi: 10.1063/5.0003330.

[11] Z. A. Kudyshev, S. I. Bogdanov, T. Isacsson, A. V. Kildishev, A. Boltasseva, and V. M. Shalaev, "Rapid Classification of Quantum Sources Enabled by Machine Learning," *Advanced Quantum Technologies,* vol. 3, no. 10, 2020, doi: 10.1002/qute.202000067.

[12] L. H. Robins, L. P. Cook, E. N. Farabaugh, and A. Feldman, "Cathodoluminescence of defects in diamond films and particles grown by hot-filament chemical-vapor deposition," *Phys Rev B Condens Matter,* vol. 39, no. 18, pp. 13367-13377, Jun 15 1989, doi: 10.1103/physrevb.39.13367.

[13] H. Watanabe, T. Kitamura, S. Nakashima, and S. Shikata, "Cathodoluminescence characterization of a nitrogen-doped homoepitaxial diamond thin film," *Journal of Applied Physics,* vol. 105, no. 9, 2009, doi: 10.1063/1.3117214.

[14] F. J. García de Abajo, "Optical excitations in electron microscopy," *Reviews of Modern Physics,* vol. 82, no. 1, pp. 209-275, 2010, doi: 10.1103/RevModPhys.82.209.

[15] F. J. M. V. Bashevoy, K. F. MacDonald, Y. Chen, and N. I. Zheludev, "Hyperspectral imaging of plasmonic nanostructures with nanoscale resolution," 2007.

[16] R. d. W. Ernst Jan R. Vesseur, Martin Kuttge, and Albert Polman, "Direct Observation of Plasmonic Modes in Au Nanowires Using High-Resolution Cathodoluminescence Spectroscopy," 2007.

[17] E. S. Barnard, T. Coenen, E. J. Vesseur, A. Polman, and M. L. Brongersma, "Imaging the hidden modes of ultrathin plasmonic strip antennas by cathodoluminescence," *Nano Lett,* vol. 11, no. 10, pp. 4265-9, Oct 12 2011, doi: 10.1021/nl202256k.

[18] B. G. Andrea Lovera, Peter Nordlander, and Olivier J.F. Martin, "Mechanisms of Fano resonances in coupled plasmonic systems," 2013.

[19] J. B. Lassiter, H. Sobhani, M. W. Knight, W. S. Mielczarek, P. Nordlander, and N. J. Halas, "Designing and deconstructing the Fano lineshape in plasmonic nanoclusters," *Nano Lett,* vol. 12, no. 2, pp. 1058-62, Feb 8 2012, doi: 10.1021/nl204303d.

[20] A. Maity, A. Maiti, P. Das, D. Senapati, and T. Kumar Chini, "Effect of Intertip Coupling on the Plasmonic Behavior of Individual Multitipped Gold Nanoflower," *ACS Photonics,* vol. 1, no. 12, pp. 1290-1297, 2014, doi: 10.1021/ph500309j.

[21] I. Aharonovich and E. Neu, "Diamond Nanophotonics," *Advanced Optical Materials,* vol. 2, no. 10, pp. 911-928, 2014, doi: 10.1002/adom.201400189.

[22] G. Balasubramanian *et al.*, "Ultralong spin coherence time in isotopically engineered

diamond," *Nature materials,* vol. 8, no. 5, pp. 383-387, 2009.
[23] J. Taylor *et al.*, "High-sensitivity diamond magnetometer with nanoscale resolution," *Nature Physics,* vol. 4, no. 10, pp. 810-816, 2008.
[24] K. Beha, A. Batalov, N. B. Manson, R. Bratschitsch, and A. Leitenstorfer, "Optimum photoluminescence excitation and recharging cycle of single nitrogen-vacancy centers in ultrapure diamond," *Phys Rev Lett,* vol. 109, no. 9, p. 097404, Aug 31 2012, doi: 10.1103/PhysRevLett.109.097404.
[25] K. M. C. Fu, C. Santori, P. E. Barclay, and R. G. Beausoleil, "Conversion of neutral nitrogen-vacancy centers to negatively charged nitrogen-vacancy centers through selective oxidation," *Applied Physics Letters,* vol. 96, no. 12, 2010, doi: 10.1063/1.3364135.
[26] A. Bhaumik, R. Sachan, and J. Narayan, "Tunable charge states of nitrogen-vacancy centers in diamond for ultrafast quantum devices," *Carbon,* vol. 142, pp. 662-672, 2019, doi: 10.1016/j.carbon.2018.10.084.
[27] C. Schreyvogel, M. Wolfer, H. Kato, M. Schreck, and C. E. Nebel, "Tuned NV emission by in-plane Al-Schottky junctions on hydrogen terminated diamond," *Sci Rep,* vol. 4, p. 3634, Jan 10 2014, doi: 10.1038/srep03634.
[28] S. Sharma and R. V. Nair, "Charge-state conversion in nitrogen-vacancy centers mediated by an engineered photonic environment," *Physical Review A,* vol. 101, no. 4, 2020, doi: 10.1103/PhysRevA.101.043420.
[29] X.-D. Chen, C.-L. Zou, F.-W. Sun, and G.-C. Guo, "Optical manipulation of the charge state of nitrogen-vacancy center in diamond," *Applied Physics Letters,* vol. 103, no. 1, 2013, doi: 10.1063/1.4813120.
[30] P. Siyushev, H. Pinto, M. Voros, A. Gali, F. Jelezko, and J. Wrachtrup, "Optically controlled switching of the charge state of a single nitrogen-vacancy center in diamond at cryogenic temperatures," *Phys Rev Lett,* vol. 110, no. 16, p. 167402, Apr 19 2013, doi: 10.1103/PhysRevLett.110.167402.
[31] M. Sola-Garcia, S. Meuret, T. Coenen, and A. Polman, "Electron-Induced State Conversion in Diamond NV Centers Measured with Pump-Probe Cathodoluminescence Spectroscopy," *ACS Photonics,* vol. 7, no. 1, pp. 232-240, Jan 15 2020, doi: 10.1021/acsphotonics.9b01463.
[32] A. Gruber, A. Dräbenstedt, C. Tietz, L. Fleury, J. Wrachtrup, and C. Von Borczyskowski, "Scanning confocal optical microscopy and magnetic resonance on single defect centers," *Science,* vol. 276, no. 5321, pp. 2012-2014, 1997.
[33] A. Beveratos, R. Brouri, T. Gacoin, J.-P. Poizat, and P. Grangier, "Nonclassical radiation from diamond nanocrystals," *Physical Review A,* vol. 64, no. 6, 2001, doi: 10.1103/PhysRevA.64.061802.
[34] A. Collins, M. Thomaz, and M. I. B. Jorge, "Luminescence decay time of the 1.945 eV centre in type Ib diamond," *Journal of Physics C: Solid State Physics,* vol. 16, no. 11, p. 2177, 1983.
[35] G. Liaugaudas, G. Davies, K. Suhling, R. U. A. Khan, and D. J. F. Evans, "Luminescence lifetimes of neutral nitrogen-vacancy centres in synthetic diamond containing nitrogen," *Journal of Physics: Condensed Matter,* vol. 24, no. 43, 2012, doi: 10.1088/0953-8984/24/43/435503.
[36] J. Storteboom, P. Dolan, S. Castelletto, X. Li, and M. Gu, "Lifetime investigation of single nitrogen vacancy centres in nanodiamonds," *Opt Express,* vol. 23, no. 9, pp. 11327-33, May 4 2015, doi: 10.1364/OE.23.011327.
[37] F. A. Inam, A. M. Edmonds, M. J. Steel, and S. Castelletto, "Tracking emission rate dynamics of nitrogen vacancy centers in nanodiamonds," *Applied Physics Letters,* vol. 102, no. 25, 2013, doi: 10.1063/1.4812711.
[38] M. Y. Shalaginov *et al.*, "Characterization of nanodiamonds for metamaterial applications," *Applied Physics B,* vol. 105, no. 2, pp. 191-195, 2011, doi: 10.1007/s00340-011-4718-6.
[39] P. Reineck *et al.*, "Not All Fluorescent Nanodiamonds Are Created Equal: A Comparative Study," *Particle & Particle Systems Characterization,* vol. 36, no. 3, 2019, doi: 10.1002/ppsc.201900009.
[40] D. A. Shilkin *et al.*, "Optical Magnetism and Fundamental Modes of Nanodiamonds," *ACS Photonics,* vol. 4, no. 5, pp. 1153-1158, 2017, doi: 10.1021/acsphotonics.7b00007.
[41] A. S. Zalogina *et al.*, "Purcell effect in active diamond nanoantennas," *Nanoscale,* vol. 10, no. 18, pp. 8721-8727, May 10 2018, doi: 10.1039/c7nr07953b.
[42] S. V. Bolshedvorskii *et al.*, "Single bright NV centers in aggregates of detonation nanodiamonds," *Optical Materials Express,* vol. 7, no. 11, 2017, doi: 10.1364/ome.7.004038.
[43] C. Bradac *et al.*, "Observation and control of blinking nitrogen-vacancy centres in discrete

nanodiamonds," *Nat Nanotechnol,* vol. 5, no. 5, pp. 345-9, May 2010, doi: 10.1038/nnano.2010.56.
[44] Y. Chi, G. Chen, F. Jelezko, E. Wu, and H. Zeng, "Enhanced Photoluminescence of Single-Photon Emitters in Nanodiamonds on a Gold Film," *IEEE Photonics Technology Letters,* vol. 23, no. 6, pp. 374-376, 2011, doi: 10.1109/lpt.2011.2106488.
[45] M. Y. Shalaginov *et al.*, "Enhancement of single-photon emission from nitrogen-vacancy centers with TiN/(Al,Sc)N hyperbolic metamaterial," *Laser & Photonics Reviews,* vol. 9, no. 1, pp. 120-127, 2015, doi: 10.1002/lpor.201400185.
[46] M. Y. Shalaginov *et al.*, "Broadband enhancement of spontaneous emission from nitrogen-vacancy centers in nanodiamonds by hyperbolic metamaterials," *Applied Physics Letters,* vol. 102, no. 17, 2013, doi: 10.1063/1.4804262.
[47] K. M. C. Fu *et al.*, "Coupling of nitrogen-vacancy centers in diamond to a GaP waveguide," *Applied Physics Letters,* vol. 93, no. 23, 2008, doi: 10.1063/1.3045950.
[48] N. Yamamoto, J. C. H. Spence, and D. Fathy, "Cathodoluminescence and polarization studies from individual dislocations in diamond," *Philosophical Magazine B,* vol. 49, no. 6, pp. 609-629, 2006, doi: 10.1080/13642818408227648.
[49] M. L. Brongersma and V. M. Shalaev, "The case for plasmonics," *science,* vol. 328, no. 5977, pp. 440-441, 2010.
[50] W. L. Barnes, A. Dereux, and T. W. Ebbesen, "Surface plasmon subwavelength optics," *nature,* vol. 424, no. 6950, pp. 824-830, 2003.
[51] R. Kolesov *et al.*, "Wave–particle duality of single surface plasmon polaritons," *Nature Physics,* vol. 5, no. 7, pp. 470-474, 2009, doi: 10.1038/nphys1278.
[52] A. Huck, S. Kumar, A. Shakoor, and U. L. Andersen, "Controlled coupling of a single nitrogen-vacancy center to a silver nanowire," *Phys Rev Lett,* vol. 106, no. 9, p. 096801, Mar 4 2011, doi: 10.1103/PhysRevLett.106.096801.
[53] S. Kumar, A. Huck, Y. Chen, and U. L. Andersen, "Coupling of a single quantum emitter to end-to-end aligned silver nanowires," *Applied Physics Letters,* vol. 102, no. 10, 2013, doi: 10.1063/1.4795015.
[54] S. Kumar, A. Huck, and U. L. Andersen, "Efficient coupling of a single diamond color center to propagating plasmonic gap modes," *Nano Lett,* vol. 13, no. 3, pp. 1221-5, Mar 13 2013, doi: 10.1021/nl304682r.
[55] S. Kumar, N. I. Kristiansen, A. Huck, and U. L. Andersen, "Generation and controlled routing of single plasmons on a chip," *Nano Lett,* vol. 14, no. 2, pp. 663-9, Feb 12 2014, doi: 10.1021/nl403907w.
[56] H. Siampour, S. Kumar, and S. I. Bozhevolnyi, "Nanofabrication of Plasmonic Circuits Containing Single Photon Sources," *ACS Photonics,* vol. 4, no. 8, pp. 1879-1884, 2017, doi: 10.1021/acsphotonics.7b00374.
[57] E. Ampem-Lassen *et al.*, "Nano-manipulation of diamond-based single photon sources," *Optics express,* vol. 17, no. 14, pp. 11287-11293, 2009.
[58] M. Gregor, R. Henze, T. Schröder, and O. Benson, "On-demand positioning of a preselected quantum emitter on a fiber-coupled toroidal microresonator," *Applied Physics Letters,* vol. 95, no. 15, p. 153110, 2009.
[59] T. Schroder, A. W. Schell, G. Kewes, T. Aichele, and O. Benson, "Fiber-integrated diamond-based single photon source," *Nano Lett,* vol. 11, no. 1, pp. 198-202, Jan 12 2011, doi: 10.1021/nl103434r.
[60] L. Liebermeister *et al.*, "Tapered fiber coupling of single photons emitted by a deterministically positioned single nitrogen vacancy center," *Applied Physics Letters,* vol. 104, no. 3, 2014, doi: 10.1063/1.4862207.
[61] T. Schröder, M. Fujiwara, T. Noda, H.-Q. Zhao, O. Benson, and S. Takeuchi, "A nanodiamond-tapered fiber system with high single-mode coupling efficiency," *Optics express,* vol. 20, no. 10, pp. 10490-10497, 2012.
[62] M. Almokhtar, M. Fujiwara, H. Takashima, and S. Takeuchi, "Numerical simulations of nanodiamond nitrogen-vacancy centers coupled with tapered optical fibers as hybrid quantum nanophotonic devices," *Opt Express,* vol. 22, no. 17, pp. 20045-59, Aug 25 2014, doi: 10.1364/OE.22.020045.
[63] R. Albrecht, A. Bommer, C. Deutsch, J. Reichel, and C. Becher, "Coupling of a single nitrogen-vacancy center in diamond to a fiber-based microcavity," *Phys Rev Lett,* vol. 110, no. 24, p. 243602, Jun 14 2013, doi: 10.1103/PhysRevLett.110.243602.
[64] K. M. C. Fu, P. E. Barclay, C. Santori, A. Faraon, and R. G. Beausoleil, "Low-temperature

tapered-fiber probing of diamond nitrogen-vacancy ensembles coupled to GaP microcavities," *New Journal of Physics,* vol. 13, no. 5, 2011, doi: 10.1088/1367-2630/13/5/055023.

[65] R. N. Patel *et al.*, "Efficient photon coupling from a diamond nitrogen vacancy center by integration with silica fiber," *Light Sci Appl,* vol. 5, no. 2, p. e16032, Feb 2016, doi: 10.1038/lsa.2016.32.

[66] M. R. Henderson *et al.*, "Diamond in tellurite glass: a new medium for quantum information," *Adv Mater,* vol. 23, no. 25, pp. 2806-10, Jul 5 2011, doi: 10.1002/adma.201100151.

[67] A. Faraon, P. E. Barclay, C. Santori, K.-M. C. Fu, and R. G. Beausoleil, "Resonant enhancement of the zero-phonon emission from a colour centre in a diamond cavity," *Nature Photonics,* vol. 5, no. 5, pp. 301-305, 2011, doi: 10.1038/nphoton.2011.52.

[68] B. J. Hausmann *et al.*, "Integrated diamond networks for quantum nanophotonics," *Nano Lett,* vol. 12, no. 3, pp. 1578-82, Mar 14 2012, doi: 10.1021/nl204449n.

[69] A. Faraon, C. Santori, Z. Huang, V. M. Acosta, and R. G. Beausoleil, "Coupling of nitrogen-vacancy centers to photonic crystal cavities in monocrystalline diamond," *Phys Rev Lett,* vol. 109, no. 3, p. 033604, Jul 20 2012, doi: 10.1103/PhysRevLett.109.033604.

[70] N. H. Wan, S. Mouradian, and D. Englund, "Two-dimensional photonic crystal slab nanocavities on bulk single-crystal diamond," *Applied Physics Letters,* vol. 112, no. 14, 2018, doi: 10.1063/1.5021349.

[71] B. J. Hausmann *et al.*, "Coupling of NV centers to photonic crystal nanobeams in diamond," *Nano Lett,* vol. 13, no. 12, pp. 5791-6, 2013, doi: 10.1021/nl402174g.

[72] O. Benson, "Assembly of hybrid photonic architectures from nanophotonic constituents," *Nature,* vol. 480, no. 7376, pp. 193-9, Dec 8 2011, doi: 10.1038/nature10610.

[73] "One-by-One Coupling of Single Defect Centers in Nanodiamonds to High-Q Modes of an Optical Microresonator," *NANO LETTERS,* 2008.

[74] S. Schietinger and O. Benson, "Coupling single NV-centres to high-Qwhispering gallery modes of a preselected frequency-matched microresonator," *Journal of Physics B: Atomic, Molecular and Optical Physics,* vol. 42, no. 11, 2009, doi: 10.1088/0953-4075/42/11/114001.

[75] C. Bradac, T. Gaebel, N. Naidoo, J. R. Rabeau, and A. S. Barnard, "Single Photon Emission from Diamond nanocrystals in an Opal Photonic Crystal," *Nano Lett,* vol. 9, no. 10, pp. 3555-64, Oct 2009, doi: 10.1021/nl9017379.

[76] F. A. Inam *et al.*, "Modification of spontaneous emission from nanodiamond colour centres on a structured surface," *New Journal of Physics,* vol. 13, no. 7, 2011, doi: 10.1088/1367-2630/13/7/073012.

[77] "Purcell Factor Enhancement by Dielectric Nanoantennas for Nanodiamonds with NV-centers," 2017.

[78] P. E. Barclay, K.-M. C. Fu, C. Santori, and R. G. Beausoleil, "Chip-based microcavities coupled to nitrogen-vacancy centers in single crystal diamond," *Applied Physics Letters,* vol. 95, no. 19, 2009, doi: 10.1063/1.3262948.

[79] T. van der Sar *et al.*, "Deterministic nanoassembly of a coupled quantum emitter–photonic crystal cavity system," *Applied Physics Letters,* vol. 98, no. 19, 2011, doi: 10.1063/1.3571437.

[80] A. W. Schell *et al.*, "Three-dimensional quantum photonic elements based on single nitrogen vacancy-centres in laser-written microstructures," *Sci Rep,* vol. 3, p. 1577, 2013, doi: 10.1038/srep01577.

[81] D. Englund *et al.*, "Deterministic coupling of a single nitrogen vacancy center to a photonic crystal cavity," *Nano Lett,* vol. 10, no. 10, pp. 3922-6, Oct 13 2010, doi: 10.1021/nl101662v.

[82] M. D. Eisaman, J. Fan, A. Migdall, and S. V. Polyakov, "Enhancement of the zero phonon line emission from a single nitrogen vacancy center in a nanodiamond via coupling to a photonic crystal cavity " *Rev Sci Instrum,* vol. 82, no. 7, p. 071101, Jul 2011, doi: 10.1063/1.3610677.

[83] K. G. Fehler, A. P. Ovvyan, N. Gruhler, W. H. P. Pernice, and A. Kubanek, "Efficient Coupling of an Ensemble of Nitrogen Vacancy Center to the Mode of a High-Q, Si3N4 Photonic Crystal Cavity," *ACS Nano,* vol. 13, no. 6, pp. 6891-6898, 2019, doi: 10.1021/acsnano.9b01668.

[84] J. E. Froch *et al.*, "Photonic Nanobeam Cavities with Nanopockets for Efficient Integration of Fluorescent Nanoparticles," *Nano Lett,* vol. 20, no. 4, pp. 2784-2790, Apr 8 2020, doi: 10.1021/acs.nanolett.0c00466.

[85] J. Gong, N. Steinsultz, and M. Ouyang, "Nanodiamond-based nanostructures for coupling nitrogen-vacancy centres to metal nanoparticles and semiconductor quantum dots," *Nat Commun,* vol. 7, p. 11820, Jun 8 2016, doi: 10.1038/ncomms11820.

[86] J. Zhao *et al.*, "Light Emission from Plasmonic Nanostructures Enhanced with Fluorescent Nanodiamonds," *Sci Rep,* vol. 8, no. 1, p. 3605, Feb 26 2018, doi: 10.1038/s41598-018-22019-z.
[87] J. T. Choy *et al.*, "Enhanced single-photon emission from a diamond–silver aperture," *Nature Photonics,* vol. 5, no. 12, pp. 738-743, 2011, doi: 10.1038/nphoton.2011.249.
[88] J. T. Choy, I. Bulu, B. J. M. Hausmann, E. Janitz, I. C. Huang, and M. Lončar, "Spontaneous emission and collection efficiency enhancement of single emitters in diamond via plasmonic cavities and gratings," *Applied Physics Letters,* vol. 103, no. 16, 2013, doi: 10.1063/1.4817397.
[89] S. K. H. Andersen, S. Kumar, and S. I. Bozhevolnyi, "Ultrabright Linearly Polarized Photon Generation from a Nitrogen Vacancy Center in a Nanocube Dimer Antenna," *Nano Lett,* vol. 17, no. 6, pp. 3889-3895, Jun 14 2017, doi: 10.1021/acs.nanolett.7b01436.
[90] H. Siampour, S. Kumar, and S. I. Bozhevolnyi, "Chip-integrated plasmonic cavity-enhanced single nitrogen-vacancy center emission," *Nanoscale,* vol. 9, no. 45, pp. 17902-17908, Nov 23 2017, doi: 10.1039/c7nr05675c.
[91] S. I. Bogdanov *et al.*, "Ultrabright Room-Temperature Sub-Nanosecond Emission from Single Nitrogen-Vacancy Centers Coupled to Nanopatch Antennas," *Nano Lett,* vol. 18, no. 8, pp. 4837-4844, Aug 8 2018, doi: 10.1021/acs.nanolett.8b01415.
[92] A. W. Schell, P. Engel, J. F. Werra, C. Wolff, K. Busch, and O. Benson, "Scanning single quantum emitter fluorescence lifetime imaging: quantitative analysis of the local density of photonic states," *Nano Lett,* vol. 14, no. 5, pp. 2623-7, May 14 2014, doi: 10.1021/nl500460c.
[93] Y. Kan, F. Ding, C. Zhao, and S. I. Bozhevolnyi, "Directional off-Normal Photon Streaming from Hybrid Plasmon-Emitter Coupled Metasurfaces," *ACS Photonics,* vol. 7, no. 5, pp. 1111-1116, 2020, doi: 10.1021/acsphotonics.0c00196.
[94] Y. Kan, S. K. H. Andersen, F. Ding, S. Kumar, C. Zhao, and S. I. Bozhevolnyi, "Metasurface-Enabled Generation of Circularly Polarized Single Photons," *Adv Mater,* vol. 32, no. 16, p. e1907832, Apr 2020, doi: 10.1002/adma.201907832.
[95] P. B. R. R. Nair, A. N. Grigorenko, K. S. Novoselov, T. J. Booth, T. Stauber, N. M. R. Peres, and A. K. Geim, "Fine Structure Constant Defines Visual Transparency of Graphene," *Science,* 2008, doi: 10.1126/science.1156965originally.
[96] X. Liu *et al.*, "Energy transfer from a single nitrogen-vacancy center in nanodiamond to a graphene monolayer," *Applied Physics Letters,* vol. 101, no. 23, 2012, doi: 10.1063/1.4769367.
[97] J. Tisler *et al.*, "Single defect center scanning near-field optical microscopy on graphene," *Nano Lett,* vol. 13, no. 7, pp. 3152-6, Jul 10 2013, doi: 10.1021/nl401129m.
[98] A. Brenneis *et al.*, "Ultrafast electronic readout of diamond nitrogen-vacancy centres coupled to graphene," *Nat Nanotechnol,* vol. 10, no. 2, pp. 135-9, Feb 2015, doi: 10.1038/nnano.2014.276.
[99] C. Zachreson, A. A. Martin, I. Aharonovich, and M. Toth, "Electron beam controlled restructuring of luminescence centers in polycrystalline diamond," *ACS Appl Mater Interfaces,* vol. 6, no. 13, pp. 10367-72, Jul 9 2014, doi: 10.1021/am501865t.
[100] H. Zhang, D. R. Glenn, R. Schalek, J. W. Lichtman, and R. L. Walsworth, "Efficiency of Cathodoluminescence Emission by Nitrogen-Vacancy Color Centers in Nanodiamonds," *Small,* vol. 13, no. 22, Jun 2017, doi: 10.1002/smll.201700543.
[101] D. R. Glenn *et al.*, "Correlative light and electron microscopy using cathodoluminescence from nanoparticles with distinguishable colours," *Sci Rep,* vol. 2, p. 865, 2012, doi: 10.1038/srep00865.
[102] L. H. Tizei and M. Kociak, "Spectrally and spatially resolved cathodoluminescence of nanodiamonds: local variations of the NV(0) emission properties," *Nanotechnology,* vol. 23, no. 17, p. 175702, May 4 2012, doi: 10.1088/0957-4484/23/17/175702.
[103] L. H. G. Tizei *et al.*, "Spatially and spectrally resolved cathodoluminescence with fast electrons: A tool for background subtraction in luminescence intensity second-order correlation measurements applied to subwavelength inhomogeneous diamond nanocrystals," *physica status solidi (a),* vol. 210, no. 10, pp. 2060-2065, 2013, doi: 10.1002/pssa.201300044.
[104] T. van der Sar *et al.*, "Nanopositioning of a diamond nanocrystal containing a single nitrogen-vacancy defect center," *Applied Physics Letters,* vol. 94, no. 17, 2009, doi: 10.1063/1.3120558.
[105] N. Mizuochi *et al.*, "Electrically driven single-photon source at room temperature in diamond," *Nature Photonics,* vol. 6, no. 5, pp. 299-303, 2012, doi: 10.1038/nphoton.2012.75.

[106] L. H. Tizei and M. Kociak, "Spatially resolved quantum nano-optics of single photons using an electron microscope," *Phys Rev Lett,* vol. 110, no. 15, p. 153604, Apr 12 2013, doi: 10.1103/PhysRevLett.110.153604.
[107] S. Meuret *et al.*, "Photon bunching in cathodoluminescence," *Phys Rev Lett,* vol. 114, no. 19, p. 197401, May 15 2015, doi: 10.1103/PhysRevLett.114.197401.
[108] H. Lourenço-Martins *et al.*, "Probing Plasmon-NV0 Coupling at the Nanometer Scale with Photons and Fast Electrons," *ACS Photonics,* vol. 5, no. 2, pp. 324-328, 2017, doi: 10.1021/acsphotonics.7b01093.
[109] M. A. Feldman *et al.*, "Colossal photon bunching in quasiparticle-mediated nanodiamond cathodoluminescence," *Physical Review B,* vol. 97, no. 8, 2018, doi: 10.1103/PhysRevB.97.081404.
[110] F. N. Gur *et al.*, "DNA-Assembled Plasmonic Waveguides for Nanoscale Light Propagation to a Fluorescent Nanodiamond," *Nano Lett,* vol. 18, no. 11, pp. 7323-7329, Nov 14 2018, doi: 10.1021/acs.nanolett.8b03524.
[111] M. B. Prigozhin *et al.*, "Bright sub-20-nm cathodoluminescent nanoprobes for electron microscopy," *Nat Nanotechnol,* vol. 14, no. 5, pp. 420-425, May 2019, doi: 10.1038/s41565-019-0395-0.
[112] R. Santagati *et al.*, "Magnetic-Field Learning Using a Single Electronic Spin in Diamond with One-Photon Readout at Room Temperature," *Physical Review X,* vol. 9, no. 2, 2019, doi: 10.1103/PhysRevX.9.021019.
[113] J. Wang *et al.*, "Experimental quantum Hamiltonian learning," *Nature Physics,* vol. 13, no. 6, pp. 551-555, 2017, doi: 10.1038/nphys4074.
[114] J. F. Barry *et al.*, "Optical magnetic detection of single-neuron action potentials using quantum defects in diamond," *Proc Natl Acad Sci U S A,* vol. 114, no. 32, p. E6730, Aug 8 2017, doi: 10.1073/pnas.1712523114.
[115] Y. S. John Peurifoy, Li Jing, Yi Yang, Fidel Cano-Renteria, Brendan G. DeLacy, John D. Joannopoulos, Max Tegmark, Marin Soljačić, "Nanophotonic particle simulation and inverse design using artificial neural networks," 2018.
[116] A. A. PETER R. WIECHA, CHRISTIAN GIRARD, AND OTTO L. MUSKENS, "Deep learning in nano-photonics- inverse design and beyond," 2020.
[117] D. Piccinotti, B. Gholipour, J. Yao, K. F. MacDonald, B. E. Hayden, and N. I. Zheludev, "Stoichiometric engineering of chalcogenide semiconductor alloys for nanophotonic applications," *Advanced Materials,* vol. 31, no. 14, 2019.
[118] S. G. a. B. E. Hayden, "Physical Vapor Deposition Method for the High-Throughput Synthesis of Solid-State Material Libraries," *J. Comb. Chem,* vol. 8, no. 66, 2006.
[119] S. Guerin, B. Hayden, D. W. Hewak, and C. Vian, "Synthesis and Screening of Phase Change Chalcogenide Thin Film Materials for Data Storage," *ACS Comb Sci,* vol. 19, no. 7, pp. 478-491, Jul 10 2017, doi: 10.1021/acscombsci.7b00047.
[120] S. Spencer, G. Andrews, and C. Deacon, "Contact angle of ethanol–water solutions on crystalline and mesoporous silicon," *Semiconductor science and technology,* vol. 28, no. 5, p. 055011, 2013.
[121] H. G. Tompkins and J. N. Hilfiker, *Spectroscopic Ellipsometry: Practical Application to Thin Film Characterization*. Momentum Press, 2015.
[122] D. Piccinotti, B. Gholipour, J. Yao, K. F. Macdonald, B. E. Hayden, and N. I. Zheludev, "Compositionally controlled plasmonics in amorphous semiconductor metasurfaces," *Optics express,* vol. 26, no. 16, pp. 20861-20867, 2018.
[123] F. Wooten, "Optical Properties of Solids," in *Optical Properties of Solids*. New York and London: Academic Press, 1972, ch. 3, pp. 42 - 52.
[124] D. P. Millar, "Time-resolved fluorescence spectroscopy," *Current opinion in structural biology,* vol. 6, no. 5, pp. 637-642, 1996.
[125] F. Wang, G. Dukovic, L. E. Brus, and T. F. Heinz, "Time-resolved fluorescence of carbon nanotubes and its implication for radiative lifetimes," *Physical review letters,* vol. 92, no. 17, p. 177401, 2004.
[126] L. B. McGown and F. V. Bright, "Phase-resolved fluorescence spectroscopy," *Analytical Chemistry,* vol. 56, no. 13, pp. 1400A-1417A, 1984.
[127] D. O'Connor, *Time-correlated single photon counting*. Academic Press, 2012.
[128] *FluoroHub Single photon counting controller user guide*. Horiba Jonbin Yvon.
[129] C. M. H. a. B. K. Selinger, "Single-Photon Decay Spectroscopy. II. The Pile-up Problem," *Aust. J. Chem,* 1979.

[130] H. Fujioka and K. Ura, "Electron beam blanking systems," *Scanning,* vol. 5, no. 1, pp. 3-13, 1983.
[131] R. J. Moerland, I. G. Weppelman, M. W. Garming, P. Kruit, and J. P. Hoogenboom, "Time-resolved cathodoluminescence microscopy with sub-nanosecond beam blanking for direct evaluation of the local density of states," *Opt Express,* vol. 24, no. 21, pp. 24760-24772, Oct 17 2016, doi: 10.1364/OE.24.024760.
[132] M. Hastenrath, L. Balk, K. Löhnert, and E. Kubalek, "Time resolved cathodoluminescence in the scanning electron microscope by use of the streak technique," *Journal of Microscopy,* vol. 118, no. 3, pp. 303-308, 1980.
[133] B. J. M. Brenny, A. Polman, and F. J. García de Abajo, "Femtosecond plasmon and photon wave packets excited by a high-energy electron on a metal or dielectric surface," *Physical Review B,* vol. 94, no. 15, 2016, doi: 10.1103/PhysRevB.94.155412.
[134] S. Meuret *et al.*, "Photon bunching reveals single-electron cathodoluminescence excitation efficiency in InGaN quantum wells," *Physical Review B,* vol. 96, no. 3, p. 035308, 2017.
[135] E. H. Hellen and D. Axelrod, "Fluorescence emission at dielectric and metal-film interfaces," *JOSA B,* vol. 4, no. 3, pp. 337-350, 1987.
[136] W. Lukosz and R. Kunz, "Light emission by magnetic and electric dipoles close to a plane interface. I. Total radiated power," *JOSA,* vol. 67, no. 12, pp. 1607-1615, 1977.
[137] N. Danz, R. Waldhäusl, A. Bräuer, and R. Kowarschik, "Dipole lifetime in stratified media," *JOSA B,* vol. 19, no. 3, pp. 412-419, 2002.
[138] J.-M. Jin, *The finite element method in electromagnetics*. John Wiley & Sons, 2015.
[139] R. Courant, "Variational methods for the solution of problems of equilibrium and vibrations," *Lecture notes in pure and applied mathematics,* pp. 1-1, 1994.
[140] D. B. Davidson, *Computational electromagnetics for RF and microwave engineering*. Cambridge University Press, 2010.
[141] J.-M. Jin and D. J. Riley, *Finite element analysis of antennas and arrays*. Wiley Online Library, 2009.
[142] H. Phillip and E. Taft, "Kramers-Kronig analysis of reflectance data for diamond," *Physical Review,* vol. 136, no. 5A, p. A1445, 1964.
[143] D. E. Aspnes and A. Studna, "Dielectric functions and optical parameters of si, ge, gap, gaas, gasb, inp, inas, and insb from 1.5 to 6.0 ev," *Physical review B,* vol. 27, no. 2, p. 985, 1983.
[144] G. Li, B. P. Clarke, J. K. So, K. F. MacDonald, and N. I. Zheludev, "Holographic free-electron light source," *Nat Commun,* vol. 7, p. 13705, Dec 2 2016, doi: 10.1038/ncomms13705.
[145] A. Zell, *Simulation neuronaler netze* (no. 5.3). Addison-Wesley Bonn, 1994.
[146] B. Zhou and F. Auzel, "MODE SELECTION OF A FABRY-PEROT INGAASP LASER AT 1.5 MU-M BY THE ER3+ I-4 (15/2)-] I-4 (13/2) TRANSITION," in *ANNALES DES TELECOMMUNICATIONS-ANNALS OF TELECOMMUNICATIONS*, 1993, vol. 48, no. 11-12: PRESSES POLYTECHNIQUES ET UNIVERSITAIRES ROMANDES EPFL-ECUBLENS, CENTRE MIDI …, pp. 546-556.
[147] P. Atherton, N. K. Reay, J. Ring, and T. Hicks, "Tunable fabry-perot filters," *Optical Engineering,* vol. 20, no. 6, p. 206806, 1981.
[148] M. A. Schmidt, D. Y. Lei, L. Wondraczek, V. Nazabal, and S. A. Maier, "Hybrid nanoparticle-microcavity-based plasmonic nanosensors with improved detection resolution and extended remote-sensing ability," *Nat Commun,* vol. 3, p. 1108, 2012, doi: 10.1038/ncomms2109.
[149] G. Björk, S. Machida, Y. Yamamoto, and K. Igeta, "Modification of spontaneous emission rate in planar dielectric microcavity structures," *Physical Review A,* vol. 44, no. 1, p. 669, 1991.
[150] H. Yokoyama, K. Nishi, T. Anan, H. Yamada, S. Brorson, and E. Ippen, "Enhanced spontaneous emission from GaAs quantum wells in monolithic microcavities," *Applied physics letters,* vol. 57, no. 26, pp. 2814-2816, 1990.
[151] I. Aharonovich, A. D. Greentree, and S. Prawer, "Diamond photonics," *Nature Photonics,* vol. 5, no. 7, pp. 397-405, 2011, doi: 10.1038/nphoton.2011.54.
[152] C. Dang *et al.*, "Achieving large uniform tensile elasticity in microfabricated diamond," *Science,* vol. 371, no. 6524, pp. 76-78, 2021.
[153] S. Noda, M. Fujita, and T. Asano, "Spontaneous-emission control by photonic crystals and nanocavities," *Nature photonics,* vol. 1, no. 8, pp. 449-458, 2007.
[154] N. El-Hinnawy *et al.*, "Low-loss latching microwave switch using thermally pulsed non-volatile chalcogenide phase change materials," *Applied Physics Letters,* vol. 105, no. 1, p. 013501, 2014.

[155] Q. Wang *et al.*, "Optically reconfigurable metasurfaces and photonic devices based on phase change materials," *Nature Photonics,* vol. 10, no. 1, pp. 60-65, 2016.
[156] F. Ding, Y. Yang, and S. I. Bozhevolnyi, "Dynamic metasurfaces using phase-change chalcogenides," *Advanced Optical Materials,* vol. 7, no. 14, p. 1801709, 2019.
[157] Y. Qu, Q. Li, K. Du, L. Cai, J. Lu, and M. Qiu, "Dynamic Thermal Emission Control Based on Ultrathin Plasmonic Metamaterials Including Phase-Changing Material GST," *Laser & Photonics Reviews,* vol. 11, no. 5, p. 1700091, 2017.
[158] T. Cao *et al.*, "Tuneable thermal emission using chalcogenide metasurface," *Advanced Optical Materials,* vol. 6, no. 16, p. 1800169, 2018.
[159] M. Takahashi, N. Syafawati Humam, N. Tsumori, T. Saiki, P. Regreny, and M. Gendry, "Local control of emission energy of semiconductor quantum dots using volume expansion of a phase-change material," *Applied Physics Letters,* vol. 102, no. 9, p. 093120, 2013.
[160] N. S. B. Humam *et al.*, "Redshifted and blueshifted photoluminescence emission of InAs/InP quantum dots upon amorphization of phase change material," *Optics express,* vol. 22, no. 12, pp. 14830-14839, 2014.
[161] Y. Sato *et al.*, "Tuning of emission energy of single quantum dots using phase-change mask for resonant control of their interactions," *Applied Physics A,* vol. 121, no. 4, pp. 1329-1333, 2015.
[162] A. Mohtashami and A. Femius Koenderink, "Suitability of nanodiamond nitrogen–vacancy centers for spontaneous emission control experiments," *New Journal of Physics,* vol. 15, no. 4, 2013, doi: 10.1088/1367-2630/15/4/043017.
[163] W. Lukosz and R. Kunz, "Fluorescence lifetime of magnetic and electric dipoles near a dielectric interface," *Optics Communications,* vol. 20, no. 2, pp. 195-199, 1977.
[164] H. Schniepp and V. Sandoghdar, "Spontaneous emission of europium ions embedded in dielectric nanospheres," *Physical review letters,* vol. 89, no. 25, p. 257403, 2002.
[165] B. J. Eggleton, B. Luther-Davies, and K. Richardson, "Chalcogenide photonics," *Nature photonics,* vol. 5, no. 3, p. 141, 2011.
[166] T. Martins *et al.*, "Fiber-integrated phase-change reconfigurable optical attenuator," *Apl Photonics,* vol. 4, no. 11, p. 111301, 2019.
[167] J. Zhang, Y. Zhang, Q. Hong, W. Xu, Z. Zhu, and X. Yuan, "Near-Infrared Rewritable, Non-Volatile Subwavelength Absorber Based on Chalcogenide Phase Change Materials," *Nanomaterials,* vol. 10, no. 6, p. 1222, 2020.
[168] B. Gholipour, J. Zhang, K. F. MacDonald, D. W. Hewak, and N. I. Zheludev, "An all-optical, non-volatile, bidirectional, phase-change meta-switch," *Advanced materials,* vol. 25, no. 22, pp. 3050-3054, 2013.
[169] S. Zastrow *et al.*, "Thermoelectric transport and Hall measurements of low defect Sb2Te3thin films grown by atomic layer deposition," *Semicond. Sci. Technol.,* vol. 28, no. 3, p. 035010, 2013, doi: 10.1088/0268-1242/28/3/035010.
[170] H. Zou, D. M. Rowe, and G. Min, "Preparation and characterization of p-type Sb_2Te_3 and n-type Bi_2Te_3 thin films grown by coevaporation," *J. Vac. Sci. Technol. A,* vol. 19, pp. 899-903, 2001, doi: 10.1116/1.1354600.
[171] Y. Kim, A. DiVenere, G. K. L. Wong, J. B. Ketterson, S. Cho, and J. R. Meyer, "Structural and thermoelectric transport properties of Sb2Te3 thin films grown by molecular beam epitaxy," (in English), *Journal of Applied Physics,* Article vol. 91, no. 2, pp. 715-718, Jan 2002, doi: 10.1063/1.1424056.
[172] D. Hsieh *et al.*, "Observation of time-reversal-protected single-dirac-cone topological-insulator states in Bi2Te3 and Sb2Te3," *Phys. Rev. Lett.,* vol. 103, no. 14, p. 146401, 2009, Art no. 146401, doi: 10.1103/PhysRevLett.103.146401.
[173] H. Zhang, C.-X. Liu, X.-L. Qi, X. Dai, Z. Fang, and S.-C. Zhang, "Topological insulators in Bi2Se3, Bi2Te3 and Sb2Te3 with a single Dirac cone on the surface," *Nat. Phys.,* vol. 5, no. 6, pp. 438-442, 2009, doi: 10.1038/nphys1270.
[174] D. Dobrakowski *et al.*, "Antiresonant fibers with single-and double-ring capillaries for optofluidic applications," *Optics Express,* vol. 28, no. 22, pp. 32483-32498, 2020.
[175] D. Piccinotti, B. Gholipour, J. Yao, K. F. MacDonald, B. E. Hayden, and N. I. Zheludev, "Optical Response of Nanohole Arrays Filled with Chalcogenide Low-Epsilon Media," *Advanced Optical Materials,* vol. 6, no. 22, 2018.
[176] D. Piccinotti, B. Gholipour, J. Yao, K. F. MacDonald, B. E. Hayden, and N. I. Zheludev, "Stoichiometric Engineering of Chalcogenide Semiconductor Alloys for Nanophotonic Applications," *Adv Mater,* vol. 31, no. 14, p. e1807083, Apr 2019, doi:

10.1002/adma.201807083.
[177] A. Karvounis, B. Gholipour, K. F. MacDonald, and N. I. Zheludev, "All-dielectric phase-change reconfigurable metasurface," *Applied Physics Letters,* vol. 109, no. 5, p. 051103, 2016.
[178] B. Gholipour, A. Karvounis, J. Yin, C. Soci, K. F. MacDonald, and N. I. Zheludev, "Phase-change-driven dielectric-plasmonic transitions in chalcogenide metasurfaces," *NPG Asia Materials,* vol. 10, no. 6, pp. 533-539, 2018.
[179] B. Gholipour, D. Piccinotti, A. Karvounis, K. F. MacDonald, and N. I. Zheludev, "Reconfigurable ultraviolet and high-energy visible dielectric metamaterials," *Nano letters,* vol. 19, no. 3, pp. 1643-1648, 2019.
[180] Y. Li *et al.*, "Self-Learning Perfect Optical Chirality via a Deep Neural Network," *Phys Rev Lett,* vol. 123, no. 21, p. 213902, Nov 22 2019, doi: 10.1103/PhysRevLett.123.213902.
[181] T. Pu, J. Y. Ou, V. Savinov, G. Yuan, N. Papasimakis, and N. I. Zheludev, "1-Unlabeled Far-Field Deeply Subwavelength Topological Microscopy (DSTM)," *Advanced Science,* p. 2002886, 2020.
[182] P. R. Wiecha, A. Lecestre, N. Mallet, and G. Larrieu, "Pushing the limits of optical information storage using deep learning," *Nat Nanotechnol,* vol. 14, no. 3, pp. 237-244, Mar 2019, doi: 10.1038/s41565-018-0346-1.
[183] M. J. Rust, M. Bates, and X. Zhuang, "Sub-diffraction-limit imaging by stochastic optical reconstruction microscopy (STORM)," *Nature methods,* vol. 3, no. 10, pp. 793-796, 2006.
[184] A. M. Mahmoud and N. Engheta, "Wave-matter interactions in epsilon-and-mu-near-zero structures," *Nat Commun,* vol. 5, p. 5638, Dec 5 2014, doi: 10.1038/ncomms6638.
[185] I. Liberal and N. Engheta, "Near-zero refractive index photonics," *Nature Photonics,* vol. 11, no. 3, pp. 149-158, 2017, doi: 10.1038/nphoton.2017.13.
[186] X. Niu, X. Hu, S. Chu, and Q. Gong, "Epsilon-Near-Zero Photonics: A New Platform for Integrated Devices," *Advanced Optical Materials,* vol. 6, no. 10, 2018, doi: 10.1002/adom.201701292.
[187] S. Campione, S. Liu, A. Benz, J. F. Klem, M. B. Sinclair, and I. Brener, "Epsilon-Near-Zero Modes for Tailored Light-Matter Interaction," *Physical Review Applied,* vol. 4, no. 4, 2015, doi: 10.1103/PhysRevApplied.4.044011.
[188] M. Z. Alam, S. A. Schulz, J. Upham, I. De Leon, and R. W. Boyd, "Large optical nonlinearity of nanoantennas coupled to an epsilon-near-zero material," *Nature Photonics,* vol. 12, no. 2, pp. 79-83, 2018, doi: 10.1038/s41566-017-0089-9.
[189] Y. Yang *et al.*, "High-harmonic generation from an epsilon-near-zero material," *Nature Physics,* 2019, doi: 10.1038/s41567-019-0584-7.
[190] A. M. Mahmoud, I. Liberal, and N. Engheta, "Dipole-dipole interactions mediated by epsilon-and-mu-near-zero waveguide supercoupling [Invited]," *Optical Materials Express,* vol. 7, no. 2, 2017, doi: 10.1364/ome.7.000415.
[191] I. Liberal and N. Engheta, "Nonradiating and radiating modes excited by quantum emitters in open epsilon-near-zero cavities," *Science advances,* vol. 2, no. 10, p. e1600987, 2016.
[192] J. Kim *et al.*, "Role of epsilon-near-zero substrates in the optical response of plasmonic antennas," *Optica,* vol. 3, no. 3, pp. 339-346, 2016.
[193] e. E. D. Palik, " Handbook of Optical Constants of Solids," *Academic Press, Orlando,* 1984.
[194] D. Chandler-Horowitz and P. M. Amirtharaj, "High-accuracy, midinfrared (450cm−1⩽ω⩽4000cm−1) refractive index values of silicon," *Journal of Applied Physics,* vol. 97, no. 12, 2005, doi: 10.1063/1.1923612.
[195] J. Cao, T. Sun, and K. T. Grattan, "Gold nanorod-based localized surface plasmon resonance biosensors: A review," *Sensors and actuators B: Chemical,* vol. 195, pp. 332-351, 2014.
[196] R. M. Walser, A. P. Valanju, and P. M. Valanju, "Comment on “extremely low frequency plasmons in metallic mesostructures”," *Physical review letters,* vol. 87, no. 11, p. 119701, 2001.
[197] J. B. Pendry, A. J. Holden, D. J. Robbins, and W. Stewart, "Magnetism from conductors and enhanced nonlinear phenomena," *IEEE transactions on microwave theory and techniques,* vol. 47, no. 11, pp. 2075-2084, 1999.
[198] J. B. Pendry, "Negative refraction makes a perfect lens," *Physical review letters,* vol. 85, no. 18, p. 3966, 2000.
[199] R. A. Shelby, D. R. Smith, and S. Schultz, "Experimental verification of a negative index of refraction," *science,* vol. 292, no. 5514, pp. 77-79, 2001.
[200] J. B. Pendry, D. Schurig, and D. R. Smith, "Controlling electromagnetic fields," *science,* vol. 312, no. 5781, pp. 1780-1782, 2006.

[201] N. Yu and F. Capasso, "Flat optics with designer metasurfaces," *Nature materials,* vol. 13, no. 2, pp. 139-150, 2014.
[202] M. A. Kats, R. Blanchard, P. Genevet, and F. Capasso, "Nanometre optical coatings based on strong interference effects in highly absorbing media," *Nature materials,* vol. 12, no. 1, pp. 20-24, 2013.
[203] M. A. Kats *et al.*, "Ultra-thin perfect absorber employing a tunable phase change material," *Applied Physics Letters,* vol. 101, no. 22, p. 221101, 2012.
[204] P. B. Johnson and R. W. Christy, "Optical Constants of the Noble Metals," *Physical Review B,* vol. 6, no. 12, pp. 4370-4379, 1972, doi: 10.1103/PhysRevB.6.4370.